Modeling and analysis of interactions between free surface flows and floating structures

Fabien Wahl

Sorbonne Université

École doctorale de sciences mathématiques de Paris centre

THÈSE DE DOCTORAT

en mathématiques appliquées

présentée et soutenue publiquement le 11 décembre 2018 par

FABIEN WAHL

Modélisation et analyse des interactions entre écoulements à surface libre et objets flottants

après avis des rapporteurs

M. Jean-Marc Hérard	EDF R&D
M. Tomás Morales de Luna	Universidad de Córdoba

devant le jury composé de

M. Jean-Marc Hérard	Directeur de recherche	rapporteur
Mme Muriel Boulakia	Maître de conférences	examinatrice
Mme Magali Ribot	Professeur	examinatrice
Mme Cindy Guichard	Maître de conférences	co-encadrante
M. Martin Parisot	Chargé de recherche	co-encadrant
Mme Edwige Godlewski	Professeur	directrice
M. Jacques Sainte-Marie	Directeur de recherche	directeur

Fabien Wahl
Sorbonne Université, université Paris-Diderot SPC, Cerema, CNRS, Inria, laboratoire Jacques-Louis Lions, LJLL, équipe ANGE, F-75005 Paris, France
fabien.wahl@inria.fr

Résumé

Cette thèse traite de la modélisation et de la résolution numérique d'écoulements en présence d'une structure à la surface. On considère la problématique d'un objet flottant sur un grand domaine. Les écoulements sous la banquise ou dans les conduites, les icebergs flottants et la production d'énergie renouvelable grâce à des bouées sont des applications potentielles de ce travail.

Nous dérivons un modèle de type Saint-Venant avec une contrainte de congestion supplémentaire depuis les équations de Navier-Stokes. La contrainte de congestion est un défi pour la résolution numérique d'équations hyperboliques. Nous proposons alors un modèle unifié basé sur une relaxation pseudo-compressible pour la résolution. Cette approche ne nécessite pas de décrire la dynamique de l'interface entre la partie en charge et la partie à surface libre de l'écoulement. Nous identifions les propriétés nécessaires à la résolution numérique (schéma bas-Froude, préservation des équilibres) et décrivons l'adaptation d'un schéma volumes finis. Les forces potentielles sont importantes devant les termes d'advection dans les parties congestionnées, néanmoins la préservation de l'état d'équilibre du lac au repos ainsi qu'une loi de dissipation pour l'énergie mécanique sont démontrées sous une condition non-restrictive sur le pas de temps.

Pour prendre en compte un objet flottant librement, nous introduisons un couplage entre le modèle de Saint-Venant congestionné et les équations du mouvement données par le principe fondamental de la dynamique en nous concentrant sur l'énergie du système couplé. Cet aspect est en effet d'un intérêt majeur dans la production d'énergie. Un schéma de Newmark est utilisé pour le solide et couplé à la résolution numérique pour le fluide. Nous proposons une correction entropique basée sur un choix de discrétisation particulier des termes de couplage pour assurer une loi de dissipation au niveau discret.

La méthode est validée en dimension un sur des solutions analytiques stationnaires et non-stationnaires. En particulier nous montrons des simulations de solutions stationnaires transcritiques ainsi que de cas plus concrets pouvant modéliser de façon simplifiée des récupérateurs d'énergie.

Mots-clés

équations de Saint-Venant, modèle hyperbolique congestionné, contrainte unilatérale, schéma well-balanced, schéma satisfaisant l'entropie, couplage, schéma bas-Froude

Abstract

This thesis is about the modeling and the numerical approximation of flows in the presence of a structure at the surface. We consider the floating body problem on a large space scale. It is motivated by applications for geophysical phenomena such as flows under the ice floe or in sewers, floating icebergs and renewable energy production using wave energy converters.

We derive a shallow water model with a supplementary congestion constraint from the Navier-Stokes equations. The congestion constraint is a challenging problem for the numerical approximation of hyperbolic equations. Thus we propose a unified model based on a pseudo-compressible relaxation for the resolution. This approach does not need to describe the dynamics of the interface between the free surface and the congested domain. We identify the mandatory properties for the numerical scheme (low-Froude stability, well-balanced character) and describe the adaptation of a numerical scheme based on a finite volume method. In the congested areas the potential forces are large in front of the advection terms, however the well-balanced property and the dissipation of mechanical energy are ensured under a non-restrictive condition on the time step.

To take into account freely floating objects, we introduce a coupling between the congested shallow water model and the equations given by Newton's second law of motion and focus on the energy of the coupled system. Indeed, the latter is of major interest for energy production. A Newmark scheme is used to solve the solid dynamics and coupled to the fluid scheme. We propose an entropy correction based on an adapted choice of discretization for the coupling terms in order to ensure a dissipation law at the discrete level.

A validation is established in the one dimensional case using stationary and non-stationary analytical solutions. In particular, we carry out simulations of transcritical steady flow and show the feasibility of energy converter simulations.

Keywords

shallow water equations, congested hyperbolic model, unilateral constraint, well-balanced scheme, entropy-satisfying scheme, coupling, low-Froude stability

Remerciements

Je tiens à remercier tout d'abord ceux qui m'ont encadré ces dernières années. Merci à Jacques Sainte-Marie de m'avoir ouvert la porte du monde de la recherche, de m'avoir fait confiance et de m'avoir encouragé tout au long de ces dernières années. Merci à Edwige Godlewski pour sa disponibilité malgré son agenda chargé. Merci en particulier pour ses conseils réfléchis et ses nombreuses relectures minutieuses. Un grand merci revient à Martin Parisot pour sa disponibilité, son enthousiasme et ses nombreux conseils et idées. Merci pour tout ce que j'ai pu apprendre durant ces trois années. Merci aussi à Cindy Guichard pour son écoute et sa patience, en particulier pour le fameux point fixe. J'ai eu la chance d'avoir eu à mes côtés un quatuor composé de personnes complémentaires. Merci pour tous vos efforts et votre bienveillance.

Je souhaite également remercier Jean-Marc Hérard et Tomás Morales de Luna d'avoir accepté d'être rapporteurs. Merci d'avoir lu avec attention mon mémoire et d'y avoir apporté votre intérêt. Vos remarques et conseils ont apporté une valeur ajoutée à mon mémoire.

Mes remerciements vont ensuite à Muriel Boulakia et Magali Ribot d'avoir accepté de faire partie du jury de ma thèse.

J'ai effectué ma thèse au sein de l'équipe ANGE localisée au laboratoire Jacques-Lous Lions ainsi qu'à l'Inria Rocquencourt (puis Inria Paris). La liste des personnes rencontrées durant les trois dernières années serait bien trop longue à dresser, mais cela n'enlève rien aux belles rencontres que j'ai pu faire. En particulier, merci aux membres de l'équipe ANGE pour leur accueil et leur bonne ambiance. Je tiens ici également à remercier Maryse Desnous, Corentin Lacombe, le secrétariat du LJLL ainsi que les services de l'Inria pour leur aide concernant des problèmes souvent surcontraints.

Merci à ceux qui ont accepté de relire une partie de ce mémoire, qu'ils soient scientifiques ou pas, vos remarques et conseils m'ont encouragé et rassuré lors de la rédaction.

Je n'ai pas le droit d'oublier le B.a.-ba. Merci Frédéric d'avoir « accepté » d'en reprendre l'organisation. J'espère que l'on aura encore des occasions de nous revoir dans cette configuration. Votre bonne humeur a su faire oublier les moments de doute.

Sur le plan personnel, je voudrai dire merci à Hugo pour au final plein de choses, merci à Léa de m'avoir supporté aussi longtemps et merci au bureau du quatrième étage pour nos infatigables discussions.

Merci och mengen Elteren. Dir hutt iech ëmmer interesséiert gewisen an ni opgehale mech ze ënnerstëtzen. Merci Marc an Tom fir déi (ze rar) Treffe beim „Jippelchen". Merci Philippe fir deng Ënnerstëtzung op de leschte Meter. Merci Julie !

Il me semble impossible de rendre cette énumération exhaustive donc simplement merci à ceux qui ont croisé mon chemin ici à Paris.

Table des matières

Table des illustrations

Notations

α, β ..... Newmark parameter
γ ..... CPR-parameter
δ_G, δ_G^0 ..... distance of G to the equilibrium position
$\delta_t^n, \overline{\delta_t}$ ..... time step, mean time step
δ_x ..... uniform space step
ε ..... shallowness parameter
ε_t ..... tolerance
ε_{Newton} ..... fixed point error
ζ, ζ^n, ζ^0 ..... vertical degree of freedom
$\dot{\zeta}, \dot{\zeta}^n, \dot{\zeta}^0$ ..... vertical velocity
$\ddot{\zeta}, \ddot{\zeta}^n$ ..... vertical acceleration
ζ_{eq} ..... equilibrium position
$\overline{\zeta}$ ..... characteristic length of the spring
η, η^0 ..... fluid surface
$\theta, \theta^n, \theta^0$ ..... angle of rotation
$\dot{\theta}, \dot{\theta}^n, \dot{\theta}^0$ ..... angular velocity
$\ddot{\theta}, \ddot{\theta}^n$ ..... angular acceleration
$\kappa, \kappa_B, \kappa_R$ ..... friction coefficient
λ ..... relaxation parameter
$\mu, \overline{\mu}$ ..... viscosity coefficient
ν_f^k ..... normalized face size
σ ..... viscosity tensor
$\sigma_{xx}, \sigma_{xz}, \sigma_{zx}, \sigma_{zz}$ ..... viscosity tensor component
$\phi, \phi_\lambda, \phi_k^n$ ..... potential of conservative forces
χ, χ^n, χ^0 ..... horizontal degree of freedom
$\dot{\chi}, \dot{\chi}^n, \dot{\chi}^0$ ..... horizontal velocity
$\ddot{\chi}, \ddot{\chi}^n$ ..... horizontal acceleration
ψ ..... color function
ω ..... time step reduction coefficient

Γ ..... bottom or roof
$\Lambda, \widetilde{\Lambda}$ ..... Newmark variable
Ω, Ω_x ..... space domain, horizontal space domain
Ω_f, Ω_f^0 ..... fluid domain

$\overline{\#_{resol}}$ ..... mean number of calls of the linear system resolution
$\#_{resol}$ ..... total number of calls of the linear system resolution
c ..... damping coefficient
d ..... space dimension

e_x, e_y, e_z ..... directional unit vector
f ..... face
g ..... gravity acceleration
$h, h_\lambda, h_k^n, h^0, h_\lambda^0$ ..... water height
h_{eq} ..... water height at equilibrium position
i_{max} ..... maximum acceptable number of iterations
k, k_f ..... cell, neighbor cell
l ..... length of the domain
l_k ..... space step
l_R ..... length of the roof
n ..... interior normal to the solid
n_η, n_B, n_R ..... outward normal
p ..... pressure
$p_\eta, p_\lambda, p_k^n, p_\lambda^0$ ..... surface pressure
t, t^n ..... time variable
u, u^0 ..... velocity component
$\overline{u}, \overline{u}_\lambda, \overline{u}_k^n, \overline{u}^0, \overline{u}_\lambda^0$ ..... vertical averaged velocity
w, w^0 ..... velocity component
x ..... space component
x_k ..... coordinate of the cell center
z ..... space component

B, B_k^n ..... bottom
$\mathcal{B}$ ..... solid body
$E, E^n, \widetilde{E}, \widetilde{E}^n$ ..... energy of the solid
E_c ..... recoverable energy in time
$\mathcal{E}, \mathcal{E}_\lambda, \mathcal{E}_k^n$ ..... energy of the fluid
F_χ, F_ζ ..... external forces
$\mathcal{F}_f^n, \mathcal{F}_{k\pm\frac{1}{2}}^n$ ..... numerical flux
$\mathbb{F}_k, \mathbb{F}_{\partial\mathbb{T}}$ ..... set of faces of k, set of boundary faces
G ..... center of mass
H ..... characteristic vertical space dimension
$\overline{H}, \overline{H}_k^n$ ..... opening
$\mathcal{J}_G$ ..... moment of inertia
K ..... stiffness coefficient
L ..... characteristic horizontal space dimension
$\mathcal{L}, \widetilde{\mathcal{L}}$ ..... regularization operator
M ..... mass
N_f^k ..... unit normal to f outward to k
P, P_η, P_k^n ..... atmospheric pressure

P_c^n ..... recoverable energy
$R, R_k^n, R_0, \mathcal{R}$ ..... roof
T ..... characteristic time of observation
$\mathcal{T}$ ..... final time
T_θ, T_θ^n ..... torque of external forces
$\mathbb{T}$ ..... mesh
U ..... efficient forcing velocity
U_B, U_R ..... bottom/roof velocity component
W^n ..... fixed point variable
W_B, W_R ..... bottom/roof velocity component
X ..... point of the solid different from G

Chapitre 1

Introduction générale

La compréhension des écoulements géophysiques et plus précisément des écoulements à surface libre tels que les rivières ou les océans est essentielle à la prédiction et la prévention de catastrophes naturelles comme les inondations ou les tsunamis. S'il est impossible d'empêcher ces phénomènes, il s'agit en revanche de protéger au mieux les populations et de limiter les dégâts sur les infrastructures. Par ailleurs, la recherche de concepts innovants pour la production d'énergie par les courants ou les vagues, qui est une alternative décarbonée et durable aux énergies fossiles traditionnelles, est très active. L'estimation des ressources en énergie ainsi que l'optimisation des procédés de récupération nécessitent pourtant une bonne maîtrise de la simulation de la source ainsi que du récupérateur.

L'utilisation de modèles mathématiques permet de mieux comprendre les phénomènes observés et de faire des prévisions. Il faut proposer des modèles représentant au mieux la physique et pouvant être résolus par une méthode numérique fiable. La simulation numérique permet aussi de valider un concept de récupérateur d'énergie sans le mettre à l'eau, ni même le construire. L'analyse mathématique est nécessaire pour s'assurer de la robustesse de la méthode afin de tester des situations critiques (débit extrême, sécheresse, orage, vague scélérate, ...).

Cette thèse traitera en particulier d'écoulements à surface libre et de leur interaction avec des structures flottantes. L'objectif est de modéliser la dynamique d'un objet flottant et de proposer un outil mathématique capable de simuler un objet porté par l'eau.

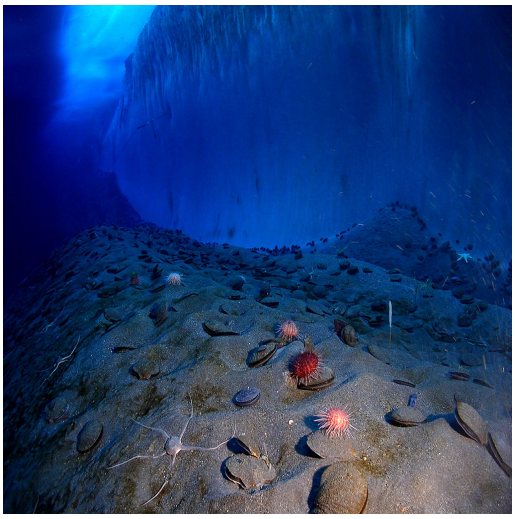

Écoulement sous la banquise

Pipe-line

Égout

Iceberg

FIGURE 1.1 – Exemples d'écoulements partiellement en charge

1.1 Motivations

De nombreux écoulements géophysiques sont à surface libre, comme les rivières ou la mer.

Il existe néanmoins des cas où l'écoulement est partiellement voire totalement en charge, c'est-à-dire sans surface libre, voir Figure 1.1. On peut penser aux décharges dans un tuyau, les égouts ou les écoulements sous la banquise. Dans tous ces cas, le fluide est contraint de passer sous une structure. Cette

contrainte peut être fixe en temps (et même en espace dans le cas d'un tuyau régulier par exemple) ou alors bouger sous la force du fluide. Les icebergs qui flottent dans la mer ou des débris qui se déplacent lors d'inondations en sont des exemples. Plus récemment, des structures flottantes servant à récupérer l'énergie marine ont été développées, voir Figure 1.2.

Dans la suite, nous allons décrire deux applications en particulier, à savoir les écoulements dans les conduites et les énergies marines.

Conduites Les conduites ou circuits hydrauliques constituent un écoulement présentant des parties en charge et des parties à surface libre [Bourdarias et al., 2012 ; Demay, 2017].

Le régime à surface libre est caractérisé par des ondes gravitaires lentes. Dans ce cas, on peut négliger la pression à la surface pour une première approximation. En revanche, un écoulement en charge est caractérisé par des ondes de pression et par conséquent on ne peut pas négliger la pression.

Des circuits de refroidissement dans une centrale électrique, des conduites forcées pour amener l'eau du barrage vers la turbine ou encore les eaux usées dans les égouts sont des cas d'applications importants. En pratique, les coups de bélier suite à une ouverture de vanne dans un circuit peuvent causer des dégâts importants sur le réseau hydraulique. En effet, une telle ouverture de vanne peut créer un débit important et engendrer un écoulement en charge capable d'endommager le circuit.

Il est difficile mathématiquement de traiter la transition entre une partie à surface libre et une partie en charge ainsi que le déplacement d'une partie en charge dans une conduite. Vue la taille des circuits, le calcul CFD, surtout s'il est très précis, devient très coûteux pour ce genre d'application, d'où la nécessité de modèles réduits mais suffisamment précis pour capturer les phénomènes d'intérêt.

Énergies marines renouvelables Historiquement, le premier récupérateur d'énergie marine remonte à 1799. À cette date, les frères Girard [Girard, 1799] ont déposé un premier brevet. Même si la machine n'a jamais vu le jour, le domaine passionnait les inventeurs ainsi que les scientifiques [Masuda, 1986]. Moins populaires pendant une période, un nouveau élan a été donné aux énergies marines après la crise du pétrole de 1973. Aujourd'hui les énergies marines sont toujours considérées comme potentiellement intéressantes et se rapprochent d'une commercialisation massive [Clément et al., 2002].

Dans la suite nous allons énumérer trois types d'EMR (Énergies Marines Renouvelables) en rapport avec cette thèse, voir Figure 1.2.

— *Houlomoteur.* C'est l'énergie de la houle des vagues qui est récupérée.

Pelamis

Éolienne *offshore* flottante

Hydrolienne en dehors de l'eau

Hydrolienne flottante

FIGURE 1.2 – Exemples de dispositifs servant à récupérer l'énergie marine

Aussi appelée « énergie des vagues », elle désigne la production d'électricité à partir de la déformation successive de la surface libre née de l'effet du vent. Un célèbre exemple est le pelamis [He et al., 2013]. Le pelamis est constitué de plusieurs cylindres rattachés par des articulations. Le mouvement des vagues agit sur un verrin hydraulique dans chaque articulation pour produire de l'électricité.

— *Éolien offshore flottant.* Contrairement aux éoliennes fixées au sol, le

caractère flottant permet d'implanter des éoliennes dans des eaux plus profondes loin des côtes. L'énergie est produite par les vents marins.

— *Hydrolienne.* Dans ce cas, l'énergie est produite par les courants (marées, rivière,...). La turbine de l'hydrolienne transforme l'énergie cinétique de l'eau en énergie mécanique et on récupère finalement l'électricité à travers un alternateur.

Actuellement, le défi consiste à rendre cette énergie compétitive en termes de coûts de production à travers l'optimisation des dispositifs de récupération et la compréhension de la source. La simulation numérique est un outil complémentaire à l'étude expérimentale pour, entre autres, améliorer la stabilité des flotteurs, tester de nouveaux concepts de récupérateurs d'énergie, comprendre les effets de sillage ou encore étudier l'interaction de la bathymétrie avec une structure.

1.2 Mise en équation

Les équations de Navier-Stokes pour un fluide incompressible [Navier, 1827 ; Stokes, 1845] décrivent le mouvement d'un fluide newtonien et sont utilisées dans la modélisation des écoulements à surface libre. L'analyse théorique de ces équations reste à ce jour un sujet de recherche ouvert et la résolution numérique est complexe à cause de la condition d'incompressibilité et aussi à cause de la non-linéarité [Prosperetti, 2002]. L'utilisation des équations de Navier-Stokes pour des applications réelles demande en outre des ressources informatiques importantes. Pour réduire cette complexité, on peut dériver des modèles réduits et des méthodes numériques robustes, précises et stables sous certaines hypothèses. La résolution numérique de ces modèles devient beaucoup moins coûteuse que les approches se basant sur les équations de Navier-Stokes, ce qui les rend intéressants pour l'optimisation.

En 1871 le physicien Barré de Saint-Venant [de Saint-Venant, 1871] a introduit les *shallow water equations* aussi appelées équations de Saint-Venant. Ces équations sont basées sur l'hypothèse que l'écoulement est peu profond. Ainsi on les utilise en pratique pour décrire des écoulements dans les rivières, les lacs ou proche de la côte. Notons g l'accélération gravitationnelle, z la composante verticale, B la bathymétrie, $\overline{u}$ la vitesse moyenne selon la verticale et h la hauteur d'eau, voir Figure 1.3. Dans [Gerbeau and Perthame, 2001], les auteurs font une dérivation asymptotique des équations de Saint-Venant depuis les équations de Navier-Stokes. Se basant sur une moyennisation verticale, la

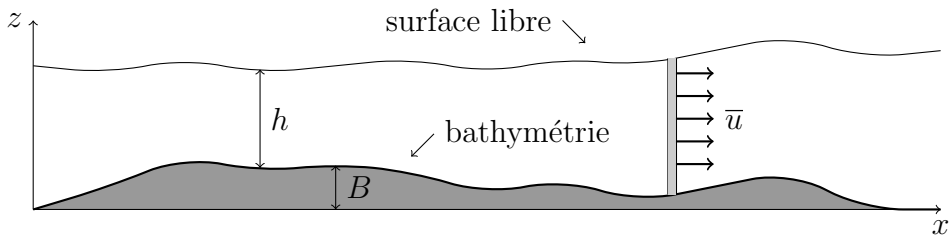

FIGURE 1.3 – Notations pour le système de Saint-Venant dans le cas unidimensionnel

vitesse est constante selon la verticale et la dimension est ainsi réduite. De plus, la pression p étant supposée hydrostatique, c'est-à-dire $p(z) = g(h + B - z)$, on évite la difficulté venant de la condition d'incompressibilité. En effet, la pression ne joue plus le rôle de multiplicateur de Lagrange associé à la condition d'incompressibilité, mais elle est fonction des autres variables. Le système de Saint-Venant s'écrit finalement

$$\begin{cases} \partial_t h + \nabla_x \cdot (h\overline{u}) &= 0 \\ \partial_t (h\overline{u}) + \nabla_x \cdot \left(h\overline{u} \otimes \overline{u} + \dfrac{g}{2} h^2 I_d \right) &= -gh\nabla_x B. \end{cases}$$

La première équation représente la conservation de la masse et la deuxième correspond à la conservation de la quantité de mouvement. Il s'agit d'un système hyperbolique dont la célérité des ondes gravitaires est donnée par $\sqrt{gh}$. Des termes sources prenant en compte par exemple la friction ou la viscosité peuvent être rajoutés [Gerbeau and Perthame, 2001 ; Marche, 2007]. Bien que l'hypothèse de faible profondeur soit valable dans beaucoup d'applications géophysiques comme par exemple les courants marins, les modèles moyennés selon la verticale ne peuvent pourtant pas modéliser le déferlement des vagues. En effet, la surface du fluide est paramétrisée par une fonction monovaluée en la variable d'espace, ce qui rend la description d'une vague déferlante impossible. Par contre les équations de Saint-Venant prennent en compte les non-linéarités ce que ne font pas certains modèles réduits, par exemple la méthode de potentiel de vitesse [Matt et al., 2012].

1.2.1 Écoulements partiellement en charge

La première investigation d'écoulements partiellement en charge remonte à 1932 [Meyer-Peter and Favre, 1932]. Aujourd'hui dans la littérature, on trouve principalement trois approches de modélisation [Bousso et al., 2013].

On utilise majoritairement l'approche *shock capturing* avancée en 1964 [Cunge and Wegner, 1964] qui introduit un seul modèle sur tout le domaine. Ce modèle détecte les transitions entre les parties à surface libre et les parties en charge. Une « fente de Preissmann » est introduite dans les parties en charge et la taille de cette fente est déterminée de manière à retrouver des ondes avec une vitesse appropriée dans ces parties. La contrainte d'incompressibilité est ainsi contournée. Des validations expérimentales ont été faites utilisant la fente de Preissmann [Aureli et al., 2015 ; Capart et al., 1997]. Notamment des codes industriels sont basés sur le *shock capturing*, par exemple CANOE® ou MOUSE®.

En 1972, Wiggert introduit la méthode dite par *interface tracking* [Wiggert, 1972]. Le domaine est séparé en une partie à surface libre et une partie en charge. On considère un système d'équations dans chaque domaine et on calcule la position de l'interface. La dynamique de cette interface devient compliquée surtout si beaucoup de points de transition apparaissent. Différents auteurs ont mené des travaux pour mieux décrire l'interface [Fuamba, 2002 ; Song et al., 1983]. De plus, le couplage de deux modèles n'est pas forcément facile à réaliser. On considère souvent le modèle d'Allievi [Wylie et al., 1993] pour modéliser la partie en charge, mais un couplage avec un modèle de type Saint-Venant ne semble pas trivial.

En 1982, Hamam et Mc Corquodale introduisent la méthode des *rigid water columns* [Hamam and McCorquodale, 1982]. Il s'agit de décomposer l'écoulement initial en colonnes d'eau rigides qui ont une vitesse uniforme et de supposer des poches d'air stationnaires entre les colonnes en charge. La dynamique de ces colonnes est régie par une EDO. Une extension a été proposée [Li and McCorquodale, 1999] pour prendre en compte la dynamique de ces poches d'air. Bien qu'elle soit facile à coder, cette méthode devient compliquée pour des géométries plus complexes.

Dans [Bourdarias et al., 2012 ; Bourdarias and Gerbi, 2007] un seul système d'équations conservatives modélisant des écoulements présentant des parties à surface libre ainsi que des parties en charge est écrit. Ce modèle regroupe les équations de Saint-Venant et les équations d'Euler compressible sous une même formulation. Les auteurs y adaptent une méthode numérique utilisant des volumes finis pour sa résolution. Ils arrivent ainsi à traiter numériquement des écoulements avec plusieurs points de transition entre une partie à surface libre et une partie en charge.

1.2.2 Interaction d'une structure avec un fluide pour les EMR

Pour modéliser l'interaction d'une structure avec un fluide, on peut distinguer deux méthodes utilisées majoritairement en pratique, à savoir la théorie des écoulements à potentiel de vitesse et les approches se basant sur la résolution des équations de Navier-Stokes. Pour des modèles intégrés de type Saint-Venant, l'interaction avec un objet flottant a été moins traitée à ce jour.

En 1949, Fritz John [John, 1949] introduit la méthode de potentiel de vitesse qui est encore aujourd'hui utilisée majoritairement dans les codes industriels (par exemple dans le code NEMOH [Babarit and Delhommeau, 2015]) grâce à son temps de calcul raisonnable lié au fait qu'elle est linéaire. Cette méthode fait l'hypothèse que les vagues sont de faible amplitude et que le mouvement induit du solide est faible. On suppose aussi le fluide incompressible, irrotationnel et sans viscosité. Plus précisément, cette théorie suppose que la vitesse u du fluide dérive d'un potentiel ψ, c'est-à-dire $u = \nabla\psi$ et la pression à la surface p est obtenue grâce à l'équation de Bernoulli, c'est-à-dire $p = -\left(\partial_t\psi + \frac{1}{2}\nabla\psi \cdot \nabla\psi + gz\right)$. Une conséquence de cette hypothèse est que la seule inconnue du problème est le potentiel. De plus, lors de la résolution, on introduit une formulation sous forme intégrale sur le bord du domaine [Brebbia et al., 1984], ce qui diminue la dimension du problème et réduit le temps de calcul [Matt et al., 2012]. La non-linéarité est pourtant nécessaire pour mieux prendre en compte les interactions avec la topographie, celles entre la vague et la structure ou encore celles entre vagues. Pour simuler par exemple des fermes de convertisseurs d'énergies proches de la côte, la non-linéarité ne semble pas négligeable. Des améliorations ad-hoc pour prendre en compte des non-linéarités ont été proposées [Harris et al., 2017 ; Kashiwagi, 2000]. Dans ces travaux, les auteurs utilisent un formalisme Eulérien pour obtenir la vitesse du fluide et un formalisme Lagrangien pour suivre l'évolution de la surface libre.

Les approches se basant sur les équations de Navier-Stokes sont très coûteuses en temps de calcul, surtout si on désire être précis. Elles permettent par contre de prendre en compte des déferlements de vagues ou encore des structures immergées. Ces techniques sont notamment utilisées dans l'interaction fluide-structure pour les écoulements sanguins [Aletti et al., 2016 ; Chabannes, 2013 ; Landajuela et al., 2017 ; Quarteroni et al., 2000]. Des travaux se basant sur cette théorie existent également dans le domaine des énergies marines [Agamloh et al., 2008 ; Palm et al., 2013 ; Yu and Li, 2013]. Pour suivre l'interface entre le solide et le fluide, on utilise les méthodes dites ALE (Arbitraire Lagrangienne Eulérienne) [Donea et al., 1982]. Complexes à

implémenter, elles sont également coûteuses car le maillage est déformé en fonction du mouvement de l'interface. Pour éviter de gérer la déformation du maillage, des méthodes à maillage fixe existent comme celle des domaines fictifs [Glowinski et al., 1994]. Moins coûteuses en temps de calcul, elles sont néanmoins moins précises pour décrire la position l'interface car cette dernière ne correspond pas forcément aux noeuds du maillage.

Naturellement, des travaux sur le couplage des deux méthodes, pour ne garder que les avantages de chaque méthode, sont apparus [Wu and Taylor, 2003]. Plus précisément, il s'agit d'utiliser une approche de potentiel de vitesse loin de l'objet et de résoudre les équations de Navier-Stokes proche de la structure seulement. Dans ces cas, la viscosité ne semble pas facile à introduire car elle n'est pas prise en compte dans les méthodes de potentiel.

La modélisation de l'interaction entre un écoulement à surface libre et un objet flottant utilisant des modèles intégrés selon la verticale est moins développée dans la littérature. Dans [Lannes, 2017], David Lannes a récemment reformulé le problème des objets flottants. Il y écrit un modèle de type Saint-Venant sous la forme

$$\left\{ \begin{array}{rcl} \partial_t h + \nabla_x \cdot (h\overline{u}) & = & 0 \\ \partial_t (h\overline{u}) + \nabla_x \cdot (h\overline{u} \otimes \overline{u}) + gh\nabla_x h & = & -h\nabla_x p \end{array} \right. \tag{1.2.1}$$

où la pression à la surface p est égale à la pression atmosphérique, c'est-à-dire $p = P$ dans la partie à surface libre et la pression dans la partie en charge n'est à priori pas connue. Dans la partie en charge, la hauteur d'eau n'est plus une inconnue et la pression à la surface peut être évaluée par l'équation elliptique

$$-\nabla_x \cdot (h\nabla_x p) = -\partial_t^2 h + \nabla_x \cdot [\nabla_x \cdot (h\overline{u} \otimes \overline{u}) + gh\nabla_x h]\,. \tag{1.2.2}$$

À l'interface entre la partie en charge et la partie à surface libre, il est alors nécessaire d'imposer des conditions de couplage. Plus précisément, l'auteur impose la continuité de la hauteur d'eau, du débit et de la pression à l'interface. Comme les modèles hyperboliques peuvent présenter des discontinuités, ces conditions peuvent être compliquées à gérer. Dans ce premier travail, l'auteur étudie des interfaces ne dépendant pas du temps. Cette hypothèse revient à considérer des objets avec des murs verticaux et un mouvement uniquement vertical.
L'analyse du modèle (1.2.1)-(1.2.2) en dimension deux et dans le cas axi-symétrique est effectuée dans [Bocchi, 2018]. Dans un article récent, Iguchi et Lannes relaxent l'hypothèse des murs verticaux et font l'analyse en dimension un d'espace [Iguchi and Lannes, 2018]. De plus, le mouvement horizontal ainsi que la rotation de l'objet sont alors traités. La difficulté vient du fait qu'il

faut étudier la dynamique de l'interface entre le domaine congestionné et le domaine libre et imposer des conditions de couplage à l'interface.
Une méthode de résolution numérique dans le cas unidimensionnel du modèle (1.2.1)-(1.2.2) basée sur des éléments finis est proposée dans [Bosi et al., 2018]. Les auteurs gardent le formalisme de [Lannes, 2017], ce qui les force à considérer des objets avec des murs verticaux et seulement un mouvement vertical.

1.2.3 Autres modèles congestionnés

Le modèle de Saint-Venant est hyperbolique [Bouchut, 2004] et la contrainte imposée sur la hauteur d'eau ressemble à d'autres effets de congestion intervenant dans certains modèles hyperboliques. Nous allons donner des exemples dans la modélisation des mouvements de foule, le trafic routier, les milieux poreux, les écoulements granulaires ou encore en biologie sans néanmoins analyser les similitudes entre l'approche suivie dans les références citées et la nôtre.

Dans la modélisation macroscopique des mouvements de foule, des modèles congestionnés sont utilisés [Roudneff, 2011]. On représente la foule par une densité de personnes ρ qui vérifie

$$\begin{cases} \partial_t \rho + \nabla \cdot (\rho u) &= 0 \\ u + \nabla p &= U \\ \rho \leq 1,\ (1-\rho)\, p = 0,\ p \geq 0 \end{cases}$$

avec U la vitesse désirée qui est celle qu'adopterait une personne en l'absence de contraintes, u la vitesse réelle adoptée en prenant en compte les contraintes et p la pression. Une personne se déplace avec sa vitesse désirée (donnée) tant qu'il n'y a pas d'obstacle ($\rho < 1$). Une fois que $\rho = 1$, sa vitesse est réduite. La deuxième équation peut être vue comme la projection de la vitesse désirée sur l'espace des vitesses admissibles.
Les auteurs proposent une résolution numérique en deux étapes. La densité ρ est d'abord advectée par la vitesse désirée U puis une projection sur l'ensemble des vitesses admissibles, c'est-à-dire prenant en compte les contraintes, est effectuée.

Dans le trafic routier, on observe des zones libres (trafic fluide) et des zones congestionnées (embouteillages). Dès que deux bouchons deviennent collants, ils n'en forment plus qu'un [Delle Monache, 2014]. Plus généralement, cette dynamique a d'abord été prise en compte dans le cadre de la dynamique de bulles d'air dans des conduites [Bouchut et al., 2000]. Les auteurs y dérivent un

modèle d'Euler sous contrainte à partir d'un système diphasique gaz/liquide. Ce modèle s'écrit

$$\begin{cases} \partial_t \alpha + \partial_x (\alpha u) &= 0 \\ \partial_t (\alpha u) + \partial_x \left(\alpha u^2 + \pi\right) &= 0 \\ 0 \leq \alpha \leq 1,\ (1-\alpha)\,\pi = 0,\ \pi \geq 0 \end{cases}$$

avec α la fraction volumique du liquide, u la vitesse et π la pression du mélange. Dans le cas $\alpha < 1$ (mélange gaz-liquide), la pression π s'annule et le modèle est le système des gaz sans pression [Bouchut, 1994]. Dans le cas $\alpha = 1$ (liquide), π représente le multiplicateur de Lagrange associé à la contrainte d'incompressibilité $\partial_x u = 0$. L'analyse dans le cas unidimensionnel est réalisée dans [Berthelin, 2002] et des approches numériques se basant sur un splitting sont proposées dans [Bouchut et al., 2000 ; Maury and Preux, 2015]. Dans [Degond et al., 2011], les auteurs proposent une autre approche numérique se basant sur des schémas développés pour un faible nombre de Mach.
Les résultats sur le système d'Euler sous contrainte ont été étendus dans [Berthelin et al., 2008a] pour la modélisation macroscopique du trafic. On obtient un système similaire comme limite du modèle Aw-Rascle [Aw and Rascle, 2000]. Il s'écrit

$$\begin{cases} \partial_t n + \partial_x (nu) &= 0 \\ \partial_t (n\,(u+p)) + \partial_x (n\,(u+p)\,u) &= 0 \\ 0 \leq n \leq N,\ (N-n)\,p = 0,\ p \geq 0 \end{cases}$$

où n représente la densité de véhicules, N une densité maximale, u la vitesse et p la compensation de vitesse. Dans ce cas le terme $u + p$ peut être vu comme une vitesse désirée. Dans les parties libres, on retrouve le modèle des gaz sans pression.
On peut aussi s'intéresser à des routes à plusieurs voies ou encore à des limitations de vitesse pour mieux appréhender les problèmes de circulation. Dans [Berthelin and Broizat, 2012 ; Berthelin et al., 2008b], ces effets ont été pris en compte en supposant que N dépend de l'espace ou de la vitesse. Citons également les travaux concernant des mélanges de différents types de véhicules [Gashaw et al., 2018].

Concernant l'analyse théorique, une première justification en dimension trois du système de Navier-Stokes sous contrainte remonte à [Lions and Masmoudi, 1999]. Il s'agit de généraliser le modèle d'Euler sous contrainte. Le système suivant est obtenu en supposant une loi de pression barotrope

$$\begin{cases} \partial_t \rho + \nabla \cdot (\rho u) &= 0 \\ \partial_t (\rho u) + \nabla \cdot (\rho u \otimes u) + \nabla \pi - \nabla (\mu \nabla \cdot u) - 2\nabla \cdot (\nu D(u)) &= 0 \\ 0 \leq \rho \leq 1,\ (1-\rho)\,\pi = 0,\ \pi \geq 0 \end{cases}$$

avec ρ la densité, u la vitesse, π la pression et (ν, μ) le couple des coefficients de viscosité de Lamé. Dans [Labbé and Maitre, 2013] les auteurs rajoutent des effets de capillarité et une viscosité dependant de la densité. Une extension considérant des fluides non barotropes et une borne sur la densité dépendant de l'espace est étudiée dans [Perrin and Zatorska, 2015].

On peut également interpréter la modélisation des milieux granulaires comme effet de congestion. Il s'agit de modéliser au niveau macroscopique des grains immergés dans un fluide. En faisant formellement tendre la viscosité vers 0 le modèle suivant est dérivé dans [Lefebvre-Lepot and Maury, 2011]

$$\begin{cases} \partial_t \rho + \partial_x (\rho u) &= 0 \\ \partial_t (\rho u) + \partial_x \left(\rho u^2\right) + \partial_x p &= f \\ \partial_t \gamma + \partial_x (\gamma u) = -p \\ \rho \leq 1,\ (1-\rho)\gamma = 0,\ \gamma \leq 0 \end{cases}$$

avec ρ la fraction volumique, u la vitesse, p la pression du fluide, $-\gamma$ la pression du solide et f un terme source. La troisième équation correspond à la fermeture du système qui lie la pression du solide et la pression du fluide. Remarquons que dans les zones libres, c'est-à-dire $\rho < 1$, le modèle considéré est le système des gaz sans pression donné précédemment.

En biologie, on utilise des modèles de type Hele-Shaw pour modéliser la croissance tumorale [Perthame et al., 2014]. Le modèle s'écrit

$$\begin{cases} \partial_t \rho &= \Delta \rho + \rho \phi (p) \\ 0 \leq \rho \leq 1,\ (1-\rho)\, p = 0,\ p \geq 0 \end{cases}$$

avec ρ la densité d'une population de cellules, p la pression et ϕ la source. Ce modèle s'inscrit plus généralement dans les équations des milieux poreux avec un terme source.

Finalement en chimiothérapie [Perthame, 2004], on peut considérer le modèle suivant

$$\begin{cases} \partial_t \eta + \nabla \cdot (\eta u) &= 0 \\ \partial_t (\eta u) + \nabla \cdot (\eta u \otimes u) + \nabla p (\eta) + \pi &= \eta \nabla c - \tau_1 \eta u \\ \partial_t c - \Delta c + \tau_2 c &= \eta \\ \eta \leq 1,\ (1-\eta)\, \pi = 0,\ \pi \geq 0 \end{cases}$$

qui couple la densité de cellules η avec la concentration du produit chimique c. La vitesse des cellules est notée u. Le système peut être vu comme un

système de la mécanique des fluides avec une loi de pression p et un terme de forçage ∇c, régi par la troisième équation.

Dans la majorité des cas, la contrainte sur la variable d'état ne dépend pas du temps ni de l'espace. Pour un objet flottant, cette hypothèse ne semble pourtant pas pertinente. Une interaction forte entre la dynamique de l'objet et la contrainte sur le fluide est nécessaire.

1.3 Synthèse des travaux

Cette thèse, financée par Sorbonne Université, a été effectuée au sein de l'équipe ANGE (Analyse Numérique, Géophysique, Environnement) - équipe commune entre Inria et le laboratoire Jacques-Louis Lions, avec la tutelle du Cerema - et elle a également bénéficié de l'encadrement de Martin Parisot et de Cindy Guichard.

L'objectif principal de ce travail est la modélisation et la résolution numérique de l'interaction d'un écoulement à surface libre avec un objet flottant utilisant un modèle de type Saint-Venant.

La suite du manuscrit est divisée en deux chapitres. Dans la première partie, nous considérons un système de type Saint-Venant avec une contrainte unilatérale afin de modéliser des écoulements partiellement en charge, c'est-à-dire des écoulements pour lesquels des parties du domaine ne sont pas à surface libre. Dans cette première partie, la dynamique de la contrainte est supposée donnée. La deuxième partie consiste à considérer un objet flottant librement. Dans ce cas, la dynamique de la contrainte est couplée au fluide.

— Le Chapitre 2 correspond à un article accepté pour publication dans la revue *ESAIM : Mathematical Modelling and Numerical Analysis*. La référence est

Godlewski, E., Parisot, M., Sainte-Marie, J., and Wahl, F. (2018b). Congested shallow water model: roof modelling in free surface flow. *ESAIM: Mathematical Modelling and Numerical Analysis*, 52(5):1679 – 1707

Ces travaux ont été présentés à la quatrième école *EGRIN* (Piriac-sur-Mer, France, 2016), au congrès *SMAI* (Ronce-les-Bains, France, 2017), à la conférence internationale *SIAM GS* (Erlangen, Allemagne, 2017) ainsi qu'au colloque *EDP-Normandie* (Caen, France, 2017).

— Le Chapitre 3 est un article en voie de soumission qui a été déposé sur

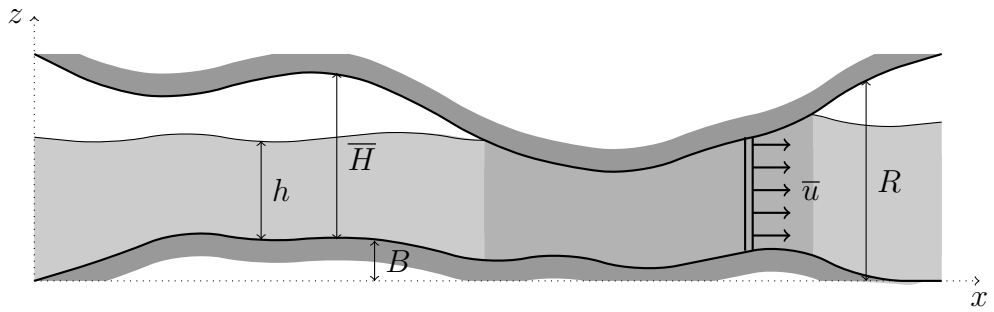

FIGURE 1.4 – Écoulement partiellement libre entre deux surfaces dans le cas unidimensionnel

HAL sous la référence

Godlewski, E., Parisot, M., Sainte-Marie, J., and Wahl, F. (2018a). Congested shallow water model: floating object. working paper or preprint <hal-01871708>

Ces travaux ont été présentés à la conférence *Simulation et Optimisation pour les Énergies Marines Renouvelables* (Paris, France, 2018) ainsi qu'à la sixième école *EGRIN* (Le Grand Lioran, France, 2018).

Nous allons dans la suite de ce chapitre présenter de façon succincte les modèles que nous avons considérés dans les deux chapitres suivants ainsi que la méthode numérique choisie pour les simuler.

1.3.1 Modélisation d'un toit dans les écoulements à surface libre

On considère un écoulement compris entre deux surfaces paramétrisées par les fonctions données B (pour la bathymétrie) et R (pour le toit) voir Figure 1.4. Nous supposons que $B(x,t) \leq R(x,t)$ et l'ouverture $\overline{H}$ entre le toit et le fond est définie par $\overline{H}(x,t) = R(x,t) - B(x,t)$. Le gradient symétrisé D_x est défini par $D_x = \frac{1}{2}\left(\nabla_x + (\nabla_x)^t\right)$.

En effectuant une approximation de faible profondeur [Gerbeau and Perthame, 2001], nous obtenons le modèle suivant à partir des équations de

Navier-Stokes

$$\begin{cases} \partial_t h + \nabla_x \cdot (h\overline{u}) = 0 \\ \partial_t (h\overline{u}) + \nabla_x \cdot \left(h\overline{u} \otimes \overline{u} + \dfrac{g}{2} h^2 I_d \right) = -h\nabla_x (gB + p_\eta) - \kappa (\overline{u} - U) \\ \qquad\qquad +2\overline{\mu} (\nabla_x \cdot (hD_x (\overline{u})) + \nabla_x (h\nabla_x \cdot \overline{u})) \end{cases} \tag{1.3.1}$$

complété par les contraintes

$$h \leq \overline{H}, \qquad \left(h - \overline{H}\right)(p_\eta - P_\eta) = 0 \qquad \text{et} \qquad p_\eta \geq P_\eta. \tag{1.3.2}$$

Les inconnues sont la hauteur d'eau h, la vitesse horizontale moyennée selon la verticale $\overline{u}$ et la pression à la surface p_η. L'accélération gravitationnelle est notée g. Les paramètres du présent modèle sont la viscosité $\overline{\mu}$, la friction κ, la vitesse de forçage U et la pression atmosphérique P_η. Les deux équations traduisent la conservation de la masse et de la quantité de mouvement. La première contrainte impose à la hauteur d'eau de rester confinée entre le toit et le fond. Dans une partie à surface libre, c'est-à-dire $h < \overline{H}$, la deuxième contrainte impose que la pression à la surface p_η est égale à la pression atmosphérique P_η et on retrouve alors le modèle de Saint-Venant classique. Dans une partie en charge, c'est-à-dire $h = \overline{H}$, la pression à la surface est inconnue. La pression joue le rôle de multiplicateur de Lagrange associé à la contrainte $h < \overline{H}$. En imposant la contrainte $p_\eta > P_\eta$, le modèle ne permet pas de modéliser des poches d'air confinées dans une conduite. En effet, ce choix ne permet pas de prendre en compte des sous-pressions, c'est-à-dire des situations où $p_\eta < P_\eta$. Lorsque la pression dans le fluide est égal à la pression atmosphérique, la pression du fluide peut ou bien devenir inférieure à cette dernière ou alors du vide est crée. Vu notre choix de modélisation, il y a création de vide, ce qui ne correspond pas à la physique.

Pour des solutions assez régulières, le modèle (1.3.1)-(1.3.2) admet une loi de dissipation sur l'énergie mécanique. Mathématiquement, cette loi permet de montrer l'existence de solutions en temps long. Pour une application aux récupérateurs d'énergie, il semble nécessaire de connaître l'énergie du fluide pour pouvoir estimer finalement l'énergie récupérable.

Dans ce travail, nous proposons une résolution unifiée du modèle (1.3.1)-(1.3.2), c'est-à-dire qu'on ne décompose pas le domaine en une partie à surface libre et une partie en charge. Cette approche a l'avantage qu'il n'est pas nécessaire de suivre explicitement la position de l'interface entre les deux parties. Cette dernière dépend fortement de la dynamique du fluide et n'est pas facile à décrire. De plus, on évite des conditions de couplage à l'interface. Cependant les contraintes (1.3.2) rendent la résolution du modèle compliquée. Nous avons donc choisi une méthode de relaxation.

Ainsi on réécrit la première contrainte de (1.3.2) sous forme d'une divergence et on relaxe cette dernière par la méthode dite pseudo-compressible [Chorin, 1968 ; Témam, 1969]. Un modèle relaxé est ainsi introduit (les termes de friction et de viscosité sont omis ici pour alléger l'écriture)

$$\begin{cases} \partial_t h_\lambda & + & \nabla_x \cdot (h_\lambda \overline{u}_\lambda) & = 0 \\ \partial_t (h_\lambda \overline{u}_\lambda) & + \nabla_x \cdot \left(h_\lambda \overline{u}_\lambda \otimes \overline{u}_\lambda + \dfrac{g}{2} h_\lambda^2 I_d \right) & = -h_\lambda \nabla_x (gB + p_\lambda) \\ p_\lambda & = & P_\eta + g \dfrac{\left(h_\lambda - \overline{H}\right)_+}{\lambda^2} \end{cases} \tag{1.3.3}$$

avec $\lambda > 0$ le paramètre de relaxation qui caractérise la « pénétration » du fluide dans le toit. Nous montrons que la réécriture et la relaxation de (1.3.2) conduisent à une expression explicite pour la pression p_λ en fonction de h_λ. La convergence du modèle relaxé (1.3.3) vers le modèle initial (1.3.1) n'est pas traitée ici, mais on peut penser utiliser les travaux [Rannacher, 1992] pour estimer l'erreur introduite par le modèle relaxé.

Pour des solutions assez régulières, le modèle (1.3.3) admet une loi de dissipation sur l'énergie mécanique et il est strictement hyperbolique avec des vitesses d'ondes $c = \sqrt{\left(1 + \frac{\mathbb{1}_{h_\lambda \geq \overline{H}}}{\lambda^2}\right) g h_\lambda}$. Dans les parties à surface libre, c'est-à-dire $h_\lambda < \overline{H}$, on retrouve les vitesses des ondes des équations de Saint-Venant classiques. Dans les parties en charge, en faisant tendre λ vers 0, la célérité des ondes devient grande, ce qui correspond à un régime dans lequel les forces potentielles sont importantes devant les termes d'advection.

Une condition nécessaire pour le schéma est la consistance avec le régime « incompressible », c'est-à-dire quand $\lambda \to 0$. On peut noter la similitude avec le régime bas-Mach dans le cas des équations d'Euler classiques [Guillard and Murrone, 2004]. L'approche numérique consiste à résoudre le système (1.3.3) en faisant tendre le paramètre de relaxation λ vers 0. Les schémas de Godunov classiques ne sont pas adaptés pour ce régime. Plus précisément, ils sont dissipatifs et présentent une condition CFL restrictive [Dellacherie, 2010].

Encore plus important que dans le cas des équations de Saint-Venant classiques, une deuxième condition nécessaire pour le schéma est de préserver l'état d'équilibre du lac au repos. Ce dernier est caractérisé par $g(h_\lambda + B) + p_\lambda$ constant et $\overline{u}_\lambda = 0$. Un schéma non *well-balanced* peut créer des petites oscillations de la taille du pas d'espace δ_x sur la hauteur d'eau qui peuvent s'accumuler et engendrer de fortes oscillations. Dans une partie congestionnée, des oscillations mêmes petites peuvent faire décrocher artificiellement le fluide du toit et engendrer de fortes variations sur la pression. En effet, dès que le fluide ne touche plus le toit, la pression à la surface p_λ est égale à la pression

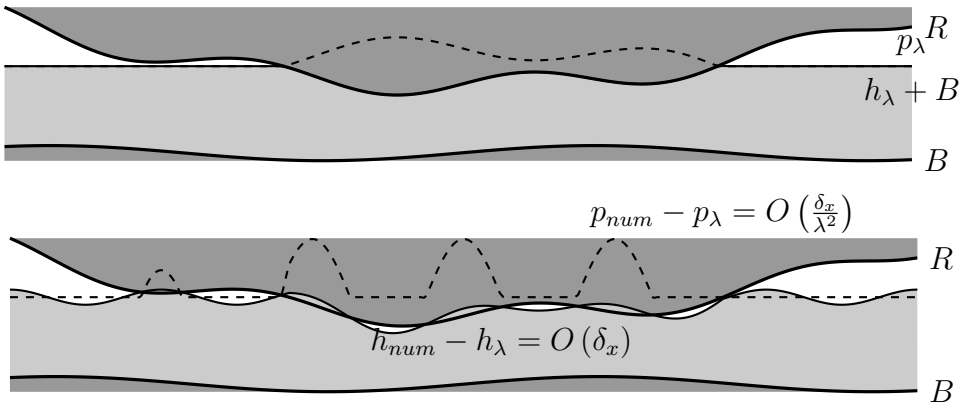

FIGURE 1.5 – Configuration du lac au repos et illustration de petites perturbations numériques. Les pointillés schématisent la pression s'exerçant à la surface ou sur le toit.

atmosphérique P_η. Lorsque le fluide se détache à certains endroits, cela peut ainsi faire apparaître des oscillations sur la pression, ce que nous avons essayé de représenter schématiquement sur la Figure 1.5 dans laquelle les pointillés, superposés à la configuration du fluide, schématisent la pression s'exerçant à la surface ou sur la toit et p_{num} (resp. h_{num}) la pression (resp. la hauteur d'eau) au niveau numérique.

Dans le présent travail, nous proposons une adaptation du schéma CPR (Centered-Potential Regularization) [Parisot and Vila, 2016] qui vérifie les deux conditions décrites ci-dessus. Le schéma CPR est une méthode volumes finis IMplicite-EXplicite. La première équation pour approcher la conservation de la masse est de type advection-diffusion, non-linéaire et implicite. L'équation sur la quantité de mouvement consiste en un schéma upwind explicite.

Vue la non-linéarité dans le schéma, il est nécessaire d'implémenter une méthode de point fixe. Cette dernière n'est pas robuste si on l'écrit en la variable h_λ. Plus précisément, le potentiel défini par $\phi_\lambda = g\,(h_\lambda + B) + p_\lambda$ et la pression p_λ deviennent grand quand λ tend vers 0, voir Figure 1.6. C'est la raison pour laquelle nous écrivons le point fixe en la variable ϕ_λ, voir Figure 1.7.

En utilisant une inégalité d'énergie, nous montrons que le schéma est stable sous une condition non restrictive sur le pas de temps. De même, on prouve la consistance avec le modèle relaxé (1.3.3), ainsi que la positivité de la hauteur d'eau, la conservation du volume d'eau et une borne supérieure sur la pression. Grâce à la borne sur la pression, on peut caractériser la pénétration.

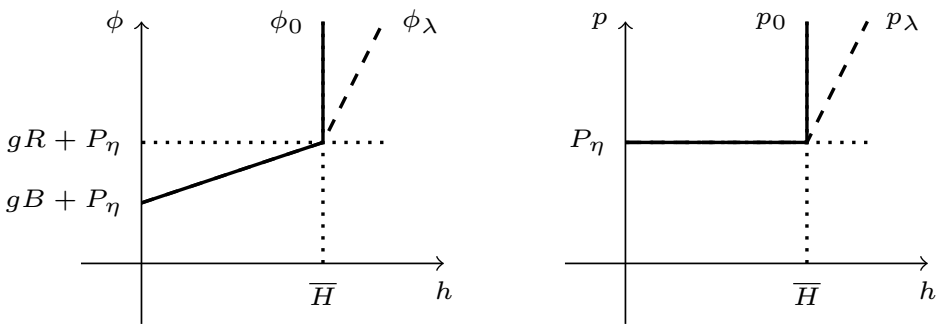

FIGURE 1.6 – Les variables ϕ_λ et p_λ en fonction de h

Plus précisément, nous obtenons au niveau discret que la pénétration est en $O(\lambda^2)$. La contrainte $h < \overline{H}$ est donc vérifiée quand λ tend vers 0.

Finalement, nous effectuons des cas test pour valider cette approche en dimension un d'espace. Les solutions transcritiques stationnaires sont étudiées et confrontées aux simulations, de même que des solutions non-stationnaires sont comparées aux résultats numériques.

L'algorithme de construction des solutions transcritiques dans le cas d'écoulements partiellement libres est donné dans l'annexe A.

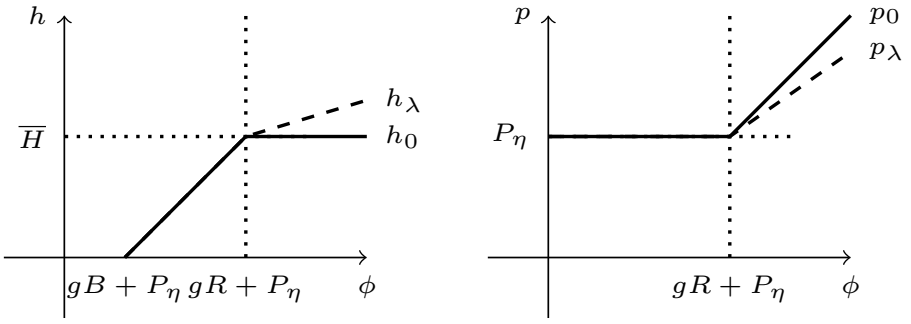

FIGURE 1.7 – Les variables h_λ et p_λ en fonction de ϕ

1.3.2 Flottaison

La deuxième partie des travaux de la thèse concerne la modélisation d'un objet flottant. Le toit n'est plus paramétrisé par une fonction R donnée et de ce fait les équations pour le fluide et la structure sont couplées.

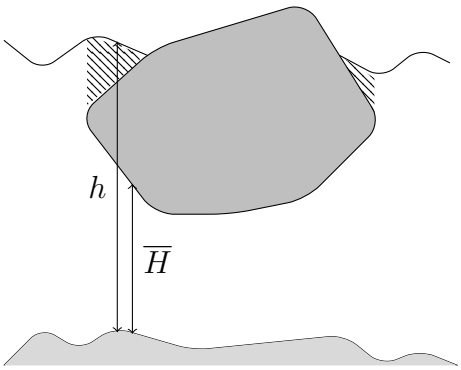

FIGURE 1.8 – Situation non autorisée

Nous considérons un objet dans le plan appelé « bouée », de masse M et de centre de gravité G, qui flotte à la surface de l'eau. Un mouvement libre en dimension deux d'espace suppose trois degrés de liberté. Le domaine horizontal est noté Ω_x.

On utilise le modèle de type Saint-Venant, c'est-à-dire moyenné sur la verticale, pour la modélisation du fluide. Ce choix ne permet pas de prendre en compte des objets immergés puisqu'une seule hauteur d'eau est considérée. Plus précisément le segment reliant un point de la surface du fluide à son projeté sur l'axe des abscisses ne doit pas intersecter l'objet en deux points distincts, voir Figure 1.8.

Pour simplifier, la pression atmosphérique P_η est prise égale à 0. Le mouvement libre de la bouée peut être décrit par le système

$$\begin{cases} M\ddot{\chi} = -\displaystyle\int_{\Omega_x} p_\eta \partial_x \mathcal{R} \mathrm{d}x \\ M\ddot{\zeta} = -Mg + \displaystyle\int_{\Omega_x} p_\eta \mathrm{d}x \\ \mathcal{J}_G \ddot{\theta} = \displaystyle\int_{\Omega_x} p_\eta \partial_\theta \mathcal{R} \mathrm{d}x \end{cases} \tag{1.3.4}$$

avec les trois degrés de liberté χ, ζ et θ représentant respectivement la translation horizontale, verticale et la rotation autour d'un axe perpendiculaire au plan et passant par G, voir Figure 1.9. Le moment d'inertie autour de G est noté $\mathcal{J}_G$. Les deux premières équations sont obtenues en appliquant la deuxième loi de Newton. La dernière équation est le théorème du moment cinétique. Le toit est alors sous la forme $R(x,t) = \mathcal{R}(x, \chi(t), \zeta(t), \theta(t))$ où $\mathcal{R}$ est lié à la géométrie de l'objet.

La connaissance de l'énergie du système eau-solide (1.3.1)-(1.3.2) et (1.3.4) est un point crucial pour le calcul de l'énergie récupérable d'un convertisseur

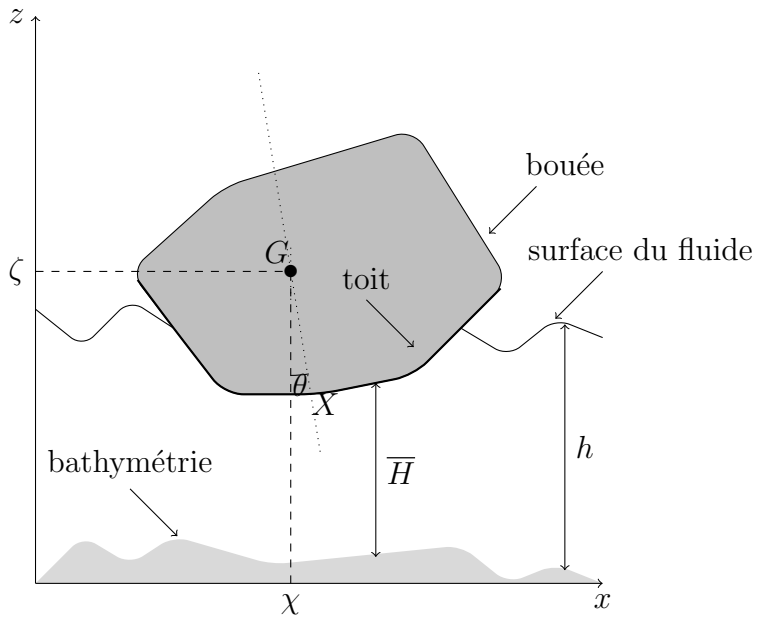

FIGURE 1.9 – Notations pour un objet flottant

d'énergie. Une attention particulière est donc portée au bilan d'énergie, aussi bien au niveau continu que discret.

On utilise un schéma de Newmark pour la résolution du système solide (1.3.4) étant donné son implémentation facile. Une discrétisation originale des dérivées de la géométrie de la bouée est proposée dans le but d'assurer une loi de dissipation d'énergie.

La principale réalisation de ce travail est le couplage entre le solide et le fluide au niveau discret. En vue de la simulation d'EMR, ce point semble indispensable.

1.4 Perspectives

Certains points de ce travail nécessitent d'être approfondis. Nous allons dans la suite décrire les principales perspectives de cette thèse.

— *Convergence* $\lambda \to 0$. Pour valider la pertinence du modèle relaxé (1.3.3), la convergence vers le modèle de Saint-Venant congestionné (1.3.1)-(1.3.2) quand λ tend vers 0 doit être prouvée. Cette limite est une question naturelle. Des travaux dans le contexte de fluides compressibles sont faits dans [Klainerman and Majda, 1981, 1982]. On peut également

penser utiliser les travaux dans le cadre des équations de Navier-Stokes [Rannacher, 1992] pour estimer l'erreur introduite par une approche pseudo-compressible. Néanmoins dans notre cas, le traitement de l'interface entre la partie en charge et la partie à surface libre reste complexe.

— *Produit non-conservatif.* Une deuxième difficulté au niveau de l'analyse est la définition du produit non-conservatif $h\nabla_x p_\eta$ dans le modèle de Saint-Venant congestionné (1.3.1)-(1.3.2). La hauteur d'eau h ainsi que la pression à la surface p_η peuvent être simultanément discontinues, voir Section 2.3.2.3. Cependant, il n'est pas immédiat d'appliquer les théories existantes dans ce domaine [Dal Maso et al., 1995].

— *Pression relative négative.* Dans le présent travail, on suppose que la pression relative est positive, c'est-à-dire $p_\eta - P_\eta \geq 0$. Cet aspect est plus globalement lié aux poches d'air piégées sous le toit. Dans [Bourdarias and Gerbi, 2007], les auteurs expliquent une stratégie numérique pour empêcher une formation de vide. Au niveau continu, ce point n'est pourtant pas clairement décrit. Dans un premier temps, on pourrait prendre en compte une loi de Laplace pour relier la pression et le volume du gaz. Ceci permettrait de modéliser des poches d'air. Une autre modélisation de poches d'air utilise un modèle diphasique. Cette approche est proposée dans [Demay, 2017].

— *Objects immergés.* Comme une seule hauteur d'eau est considérée dans notre modèle, on ne peut pas modéliser tous les objets partiellement immergés ni ceux totalement immergés [Ducassou et al., 2017 ; Guerber, 2011]. On peut penser utiliser des modèles par couches [Audusse et al., 2011] car au moins deux hauteurs d'eau doivent être prises en compte. L'analyse du passage d'un objet non-immergé à un objet totalement immergé est complexe, à la fois du point de vue analyse, que du point de vue numérique.

— *Autres modèles pour le fluide.* Dans les modèles de type Saint-Venant, on néglige l'accélération verticale. Les modèles dispersifs [Bristeau et al., 2015 ; Lannes and Bonneton, 2009] prennent en compte ces termes supplémentaires et représentent par conséquent mieux la houle. Une représentation précise des vagues est indispensable pour bien estimer l'énergie produite par les EMR.
Afin de mieux modéliser des effets de vents à la surface ou de forts effets de friction, on pourrait utiliser des modèles par couches [Audusse

et al., 2011]. La vitesse n'est plus constante selon la verticale et le profil vertical de la vitesse est pris en compte.

Un modèle par couches avec effets non-hydrostatiques a été proposé dans [Fernandez-Nieto et al., 2017].

Notre méthode pour prendre en compte des parties en charge semble bien pouvoir s'étendre aux résolutions numériques de ces modèles. Plus précisément, notre approche introduit une contrainte qui ne concerne que la hauteur d'eau et ne modifie pas l'équation sur la vitesse.

— *Interaction de plusieurs objets.* On peut également penser à la simulation de plusieurs objets pour le dimensionnement de fermes de récupérateurs d'énergie [Penalba et al., 2017]. Les modèles réduits sont intéressants pour des phénomènes à grande échelle vu leur temps de résolution raisonnable. Notre approche est directement adaptable pour prendre en compte plusieurs objets flottants. La dérive de débris lors d'inondations est une autre application de cette perspective où des interactions entre les différents objets devraient être rajoutées. Par ailleurs, certains récupérateurs d'énergie présentent une interaction avec le fond. Dans ce contexte, des modèles réduits sont étudiés dans [Benyo, 2017, 2018].

— *Confrontation avec des données réelles.* Appliquer notre méthode à un cas concret est indispensable. Nous avons montré une première étape vers la simulation de récupérateurs d'énergie marine utilisant un modèle simplifié unidimensionnel. Des solutions analytiques pour le système fluide-solide (1.3.1)-(1.3.2) et (1.3.4) sont difficiles à trouver et une confrontation à des données réelles constitue un moyen de validation nécessaire.

— *Calcul scientifique.* On a effectué des simulations en dimension un d'espace. Les temps de calcul de la présente méthode risquent néanmoins de devenir rapidement importants en dimension supérieure. Loin de l'objet flottant, on pourrait utiliser un schéma moins couteux traitant les surfaces libres et la méthode proposée dans ce travail serait uniquement utilisée proche de l'objet flottant.

Chapter 2

Congested shallow water model: roof modeling in free surface flow

This chapter has been done in collaboration with Edwige Godlewski, Martin Parisot and Jacques Sainte-Marie.

It has been published in ESAIM : Mathematical Modelling and Numerical Analysis [55].

2.1 Introduction

We deal with the derivation and the numerical resolution of a model describing shallow water flows in the presence of a roof. The roof denotes an impermeable surface above the flow which constrains the water surface in several parts of the domain. We do not assume that the roof is fixed, but the roof has a prescribed motion and the surface pressure is seen as an unilateral constraint. This assumption is not really essential to the analysis but greatly simplifies the reading. In particular the numerical procedure is not affected by the roof dynamics. The description of the fluid/structure interaction is studied in the literature for the Navier-Stokes equations [97]. However, for vertical-integrated models such as the shallow water model, the interaction with a roof has been considered only recently. The main applications of these models concern the prediction of urban flooding taking into account the flows in sewers or the hydraulic network in small hydroelectric power plants, [29; 49]. Moreover, the production of sustainable energy from wave power using floating buoys can also be realized considering a dynamical roof.

For the modeling of partially free surface flow, i.e. flow where some parts of the domain have a free surface and do not reach the roof and some other parts are in contact with the roof, two main approaches are proposed in the literature.

The first one can be classified as a coupling strategy between the free surface and the pressurized areas [66; 73]. The main advantage of this approach relies on the computation of the surface pressure induced by the roof using an elliptic equation obtained thanks to Bernoulli's equation. In addition, each sub-domain can be solved with the most appropriate numerical strategy. However, this strategy assumes a smooth enough flow in order to write transmission conditions at the coupling interface. This assumption is not always satisfied. In particular, it is well-known that hydraulic models can lead to discontinuous free surfaces which imply an advection of a discontinuous pressure. In addition, this strategy requires the description of the interface position which is a challenging issue since the interface is strongly linked to the flow dynamics.

The second strategy to model partially free surface flow is based on the design of a unified model in the whole domain. Our work is based on this idea. Previous works also deal with a unified model [22; 23; 49]. This strategy is advantageous because it does not require the description of the interface position and the transmission conditions at the interface. The partially free surface models proposed in the cited works can be described as shallow water models with an additional pressure given as an explicit function of the water depth. The additional pressure comes from the compressibility of the fluid in the pressurized areas and introduces the sound celerity in the water. The material velocity is very small in comparison to the sound celerity which leads to the particular low-Mach regime. However, in our approach, we do not consider the water as compressible. In Section 2.2.1, a shallow water model with a constraint, from now on called congestion constraint, modeling the roof is derived from the Navier-Stokes equations in a tank under the classical shallow water assumption [51].

A consequence of this approach is that the model we obtain is of hyperbolic type with a supplementary congestion constraint. This type of equations appears in many contexts. A congested hyperbolic model describing pressureless gas dynamics is proposed in [21]. The model is similar to a model of crowd motion [84]. In [16], the authors use a congested hyperbolic model to describe traffic jams. In [26], the authors use a degenerated parabolic model to describe porous media. For some particular parameters, the model can be written as a congested hyperbolic model. In [93], a congested hyperbolic model is presented as the singular limit of a barotropic model for granular

flow. One can also highlight the relevance of congestion constraints in models for chemotaxis in order to fix mathematical blow-up [94].

One of the first analysis of a congested problem is realized in [79]. In [13] a congested hyperbolic system where the constraint is verified by mass loss is analyzed. In a more general framework, congested linear hyperbolic conservation laws are analyzed in [43; 44]. Quasi-linear scalar conservation laws are studied in [77]. The congested pressureless model introduced in [21] is analyzed in [12]. Compared to the previous models, the model introduced in our work presents a bound of congestion depending on space and time.

The numerical resolution of the above cited models [22; 23; 49] is a challenging problem due to the congestion constraint. In particular in our context, where the upper bound of the water level, called the opening in the sequel, is a function depending on time and space. In Section 2.2.2, a strictly hyperbolic approximate model is proposed which is based on a pseudo-compressibility approximation. The approximate model is similar to the above cited models [22; 23; 49] with the difference that the relaxation parameter is not linked to any physical process. Nevertheless, we will require a similar asymptotic limit, namely the high potential force regime [58]. In addition, since the opening is a space (and time) function, a particular attention is given to the well-balanced property, i.e. the numerical preservation of the lake at rest. We emphasize that this property is also required in the congested area to get a relevant approximation of the surface pressure.

The main achievement is the description of a relaxation strategy, see Section 2.2.2, and the adaptation of a numerical scheme for the approximation of the congested shallow water model, see Section 2.3. Indeed, the numerical scheme for an advection model in high potential force regime [90] can be easily adapted to our (or other) congested hyperbolic models. The well-balanced property and the dissipation of the mechanical energy, acting as a mathematical entropy, are proven. Eventually, several numerical simulations in a one dimensional framework are performed and compared to analytical solutions. Simulations of discontinuous solutions are also proposed.

2.2 Mathematical modeling

2.2.1 Formal derivation of the congested shallow water model

A shallow water type model with an additional congestion constraint modeling a roof, i.e. an impermeable boundary above the flow, is derived

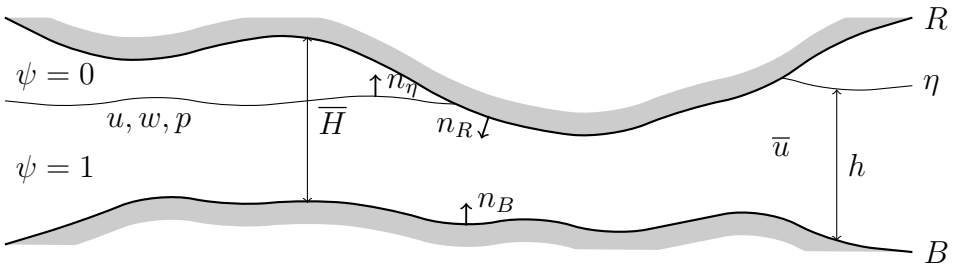

Figure 2.1 – Geometrical description of the flow

from the Navier-Stokes equations using classical thin layer arguments.
Let us consider a flow contained between two given surfaces respectively called bottom and roof. We assume that the two surfaces can be parametrized by two mono-valued smooth enough functions $B(x,t)$ (for the bottom) and $R(x,t)$ (for the roof) which satisfy $B(x,t) \leq R(x,t)$. We consider the domain $\Omega(t) = \Omega_x \times [B(x,t), R(x,t)]$ where $\Omega_x \subset \mathbb{R}^{d-1}$ with $d = 2$ or $d = 3$, see Figure 2.1. The space variable is split into its horizontal component $x \in \Omega_x$ and its vertical component $z \in [B(x,t), R(x,t)]$.

2.2.1.1 Navier-Stokes model with roof

A Navier-Stokes model describing the dynamics of the fluid is proposed. The bottom (resp. the roof) moves according to its own prescribed velocity with $U_B(x,t) \in \mathbb{R}^{d-1}$ (resp. U_R) the horizontal component and $W_B(x,t) \in \mathbb{R}$ (resp. W_R) the vertical component of the given velocity. More precisely for $\Gamma = B$ or $\Gamma = R$, it satisfies

$$\partial_t \Gamma + U_\Gamma \cdot \nabla_x \Gamma - W_\Gamma = 0. \tag{2.2.1}$$

The fluid is assumed homogeneous, with a density set to 1 for readability.
The part of the domain occupied by the fluid, denoted $\Omega_f(t)$, is marked by the color function $\psi(x,z,t) \in \{0,1\}$ such that $\psi(x,z,t) = 1$ iff $(x,z) \in \Omega_f(t)$. More precisely we assume that the fluid surface is regular enough and that there exists a mono-valued function $\eta(x,t)$ parametrizing the free surface such that ψ writes

$$\psi(x,z,t) = \begin{cases} 1, & \text{if } B(x,t) \leq z \leq \eta(x,t) \\ 0, & \text{otherwise.} \end{cases}$$

The velocity of the fluid satisfies the incompressible Navier-Stokes equations with gravity, i.e. for any $(x,z,t) \in \Omega_f(t) \times \mathbb{R}_+$

$$\begin{cases} \nabla_x \cdot u + \partial_z w = 0 \\ \partial_t u + (u \cdot \nabla_x) u + w\partial_z u + \nabla_x p - \nabla_x \cdot \sigma_{xx} - \partial_z \sigma_{xz} = 0 \\ \partial_t w + u \cdot \nabla_x w + w\partial_z w + \partial_z (p + gz) - \nabla_x \cdot \sigma_{zx} - \partial_z \sigma_{zz} = 0 \end{cases} \tag{2.2.2}$$

with $u(x,z,t) \in \mathbb{R}^{d-1}$ the horizontal component and $w(x,z,t) \in \mathbb{R}$ the vertical component of the velocity, $p(x,z,t) \in \mathbb{R}$ the pressure, g the gravity acceleration and $\sigma(u,w)$ the viscosity tensor. We denote by n_η the outward normal to the fluid surface defined by

$$n_\eta = \frac{1}{\sqrt{1 + |\nabla_x \eta|^2}} \begin{pmatrix} -\nabla_x \eta \\ 1 \end{pmatrix}.$$

The fluid is advected by the flow and the color function describing the part of the domain occupied by the fluid satisfies the following relation

$$\partial_t \psi + u \cdot \nabla_x \psi + w\partial_z \psi = 0. \tag{2.2.3}$$

From now on, a Newtonian fluid is considered, i.e. the viscosity tensor is given by

$$\sigma = \begin{pmatrix} \sigma_{xx} & \sigma_{xz} \\ \sigma_{zx} & \sigma_{zz} \end{pmatrix} \text{ with } \begin{array}{ll} \sigma_{xx} = 2\mu D_x(u), & \sigma_{xz} = \mu(\partial_z u + \nabla_x w), \\ \sigma_{zz} = 2\mu \partial_z w, & \sigma_{zx} = \mu(\partial_z u + \nabla_x w)^t, \end{array}$$

where $D_x(u) = \frac{1}{2}\left(\nabla_x u + (\nabla_x u)^t\right)$ is the symmetric gradient and $\mu > 0$ the viscosity coefficient. For each surface $\Gamma = B$ or $\Gamma = R$ the outward unit normal, see Figure 2.1, denoted by n_Γ, is defined by

$$n_B = \frac{1}{\sqrt{1 + |\nabla_x B|^2}} \begin{pmatrix} -\nabla_x B \\ 1 \end{pmatrix} \quad \text{and} \quad n_R = \frac{1}{\sqrt{1 + |\nabla_x R|^2}} \begin{pmatrix} \nabla_x R \\ -1 \end{pmatrix}.$$

At the bottom and at the roof, a no-penetration condition is considered, i.e.

$$\psi_{|z=R} \begin{pmatrix} u_{|_{z=R}} - U_R \\ w_{|_{z=R}} - W_R \end{pmatrix} \cdot n_R \geq 0 \quad \text{and} \quad \begin{pmatrix} u_{|_{z=B}} - U_B \\ w_{|_{z=B}} - W_B \end{pmatrix} \cdot n_B = 0. \tag{2.2.4}$$

The inequality at the roof is required to allow the fluid to detach itself from the surface. In addition, the friction between the fluid and the surface $\Gamma = B$ or $\Gamma = R$ is modeled by the following Navier condition

$$\psi_{|z=\Gamma} \Pi_\Gamma \left((\sigma - pI_d) n_\Gamma - \kappa_\Gamma \begin{pmatrix} u_{|_{z=\Gamma}} - U_\Gamma \\ w_{|_{z=\Gamma}} - W_\Gamma \end{pmatrix} \right) = 0 \tag{2.2.5}$$

with $\kappa_\Gamma > 0$ a friction coefficient at the surface Γ and Π_Γ the projection onto the plane tangential to the surface.
At the free surface, the continuity of the stresses reads

$$\left(1 - \psi_{|z=R}\right)\left(\sigma + (P - p)\, I_d\right) n_\eta = 0 \tag{2.2.6}$$

with $P(x, z, t)$ a given atmospheric pressure.

At this stage of modeling, when the pressure in the fluid reaches the atmospheric pressure, i.e. $p = P$, the fluid can either create vacuum, i.e. $\psi = 0$, or the pressure can decrease below the atmospheric pressure $p < P$, see [23] for more details. In [23] the authors propose a numerical strategy able to prevent the creation of vacuum but it is not clearly described at the continuous level. In the current work, only non-negative relative pressure is considered, i.e.

$$p_{|z=\eta} \geq P_{|z=\eta}. \tag{2.2.7}$$

The drawback of this assumption is that areas without water trapped under the roof can appear, which is not physically relevant. Some perspectives to overcome this drawback are discussed in the conclusion section.

The system (2.2.1)-(2.2.7) has to be completed with compatible initial data. More precisely the fluid domain at the initial time reads $\Omega_f(0) = \Omega_f^0$ with Ω_f^0 given and $\eta(x, z, 0) = \eta^0(x)$. Similarly, for any $(x, z) \in \Omega_f^0$, we assume $u(x, z, 0) = u^0(x, z)$ and $w(x, z, 0) = w^0(x, z)$ where u^0 and w^0 are given. Note that to be physically relevant, the initial fluid has to be contained in the domain, i.e. $\Omega_f^0 \subset \Omega(0)$ and the velocity should satisfy the incompressibility condition, i.e. first equation of (2.2.2).

The following domain invariance holds.

Proposition 2.2.1. *If $\Omega_f^0 \subset \Omega(0)$, then $\Omega_f(t) \subset \Omega(t)$ for any time t.*

Proof. By integration of (2.2.3) in $\mathbb{R}^d \setminus \Omega(t)$ and using a Leibniz integral rule, we get

$$\begin{aligned}\partial_t \int_{\mathbb{R}^d \setminus \Omega(t)} \psi \mathrm{d}x\mathrm{d}z = &\int_{\mathbb{R}^{d-1}} \psi_{|z=B}\left(\left(u_{|z=B} - U_B\right) \cdot \nabla_x B - \left(w_{|z=B} - W_B\right)\right) \mathrm{d}x \\ &- \int_{\mathbb{R}^{d-1}} \psi_{|z=R}\left(\left(u_{|z=R} - U_R\right) \cdot \nabla_x R - \left(w_{|z=R} - W_R\right)\right) \mathrm{d}x.\end{aligned}$$

Using the non-penetration inequality (2.2.4) and integrating in time, it yields

$$\int_{\mathbb{R}^d \setminus \Omega(t)} \psi(x, z, t)\, \mathrm{d}x\mathrm{d}z \leq \int_{\mathbb{R}^d \setminus \Omega(0)} \psi(x, z, 0)\, \mathrm{d}x\mathrm{d}z.$$

The assumption on the initial condition allows to conclude since $\psi(x, z, t) = 1$ iff $(x, z) \in \Omega_f(t)$. □

This property ensures that the fluid stays confined between the bottom and the roof.

2.2.1.2 Congested shallow water model

Let us introduce the congested shallow water model we are interested in. The unknowns of the model are the water depth h, the vertical-averaged horizontal velocity $\overline{u}$ and the surface pressure p_η which satisfy

$$\begin{cases} \partial_t h + \nabla_x \cdot (h\overline{u}) = 0 \\ \partial_t (h\overline{u}) + \nabla_x \cdot \left(h\overline{u} \otimes \overline{u} + \dfrac{g}{2} h^2 I_d \right) = -h\nabla_x (gB + p_\eta) - \kappa (\overline{u} - U) \\ \qquad\qquad +2\overline{\mu} \left(\nabla_x \cdot (h D_x (\overline{u})) + \nabla_x (h \nabla_x \cdot \overline{u}) \right) \end{cases} \tag{2.2.8}$$

with the following given parameters: κ the efficient friction parameter, U the efficient velocity of forcing and $\overline{\mu}$ the viscosity coefficient. In addition, the water depth has to satisfy the congestion constraint

$$h \leq \overline{H} \tag{2.2.9}$$

with the opening between the roof and the bottom $\overline{H}$ (see Figure 2.1) defined by

$$\overline{H}(x,t) = R(x,t) - B(x,t).$$

Eventually, the surface pressure has to satisfy

$$\left(1 - \mathbb{1}_{h \geq \overline{H}}\right)(p_\eta - P_\eta) = 0 \qquad \text{and} \qquad p_\eta \geq P_\eta, \tag{2.2.10}$$

with $P_\eta(x,t)$ the given atmospheric pressure. The shallow water model (2.2.8)-(2.2.10) is completed with the initial conditions

$$h(x,0) = h^0(x) \qquad \text{and} \qquad \overline{u}(x,0) = \overline{u}^0(x).$$

The congested shallow water model (2.2.8)-(2.2.10) can be derived from the Navier-Stokes model (2.2.1)-(2.2.7) following the strategy proposed in [51]. More precisely, considering the two characteristic space dimensions along the vertical and the horizontal dimensions, respectively H and L, and the characteristic time of observation T, the dimensionless variables read $\hat{u} = \frac{T}{L}u$, $\hat{w} = \frac{T}{H}w$, $\hat{p} = \left(\frac{T}{L}\right)^2 p$, $\hat{g} = \frac{H}{U^2}g$, $\hat{\kappa}_\Gamma = \frac{T}{L}\kappa_\Gamma$ and $\hat{\mu} = \frac{T}{L^2}\mu$. For readability, the hat $\hat{}$ is dropped even if from now on the variables are dimensionless. We claim the following proposition.

Proposition 2.2.2. *For $\varepsilon = \frac{H}{L}$ small enough, assume that the parameters satisfy the following scaling*

$$\nabla_x B = O(\varepsilon), \quad \nabla_x R = O(\varepsilon), \quad \nabla_x \eta = O(\varepsilon)$$

$$\mu = \varepsilon\mu^0, \quad \kappa_B = \varepsilon\kappa_B^0, \quad \textit{and} \quad \kappa_R = \varepsilon\kappa_R^0.$$

Then (2.2.8)-(2.2.10) *with the initial conditions*

$$h^0(x) = \eta^0(x) - B(x,0) \qquad \textit{and} \qquad \overline{u}^0(x) = \frac{1}{h^0(x)} \int_{B(x,0)}^{\eta^0(x)} u^0(x,z)\,\mathrm{d}z$$

and the parameters given by

$$\begin{gathered} \kappa = \widetilde{\kappa_B} + \mathbb{1}_{h\geq\overline{H}}\widetilde{\kappa_R}, \qquad U = \frac{1}{\kappa}\left(\widetilde{\kappa_B}U_B + \mathbb{1}_{h\geq\overline{H}}\widetilde{\kappa_R}U_R\right), \\ \overline{\mu} = \varepsilon\mu^0 \qquad \textit{and} \qquad P_\eta(x,t) = P(x,\eta(x),t) \end{gathered} \tag{2.2.11}$$

$$\textit{with} \qquad \widetilde{\kappa_R} = \begin{cases} \dfrac{\kappa_R^0}{1 + \frac{\varepsilon h}{3\mu^0}\left(\mathbb{1}_{h\geq\overline{H}}\kappa_R^0 - \frac{1}{2}\kappa_B^0\right)}, & \textit{if } \kappa_B^0 \leq 2\kappa_R^0 \\ \kappa_R^0\left(1 - \dfrac{\varepsilon h}{3\mu^0}\left(\mathbb{1}_{h\geq\overline{H}}\kappa_R^0 - \dfrac{1}{2}\kappa_B^0\right)\right), & \textit{otherwise} \end{cases}$$

$$\textit{and} \qquad \widetilde{\kappa_B} = \begin{cases} \dfrac{\kappa_B^0}{1 + \frac{\varepsilon h}{3\mu^0}\left(\kappa_B^0 - \mathbb{1}_{h\geq\overline{H}}\frac{1}{2}\kappa_R^0\right)}, & \textit{if } \kappa_R^0 \leq 2\kappa_B^0 \\ \kappa_B^0\left(1 - \dfrac{\varepsilon h}{3\mu^0}\left(\kappa_B^0 - \mathbb{1}_{h\geq\overline{H}}\dfrac{1}{2}\kappa_R^0\right)\right), & \textit{otherwise} \end{cases}$$

is formally an approximation in $O(\varepsilon^2)$ *of* (2.2.1)-(2.2.7). *More precisely*

$$h(x,t) - (\eta(x,t) - B(x,t)) = O\left(\varepsilon^2\right)$$

and

$$\overline{u}(x,t) - \frac{1}{h(x,t)} \int_{B(x,t)}^{\eta(x,t)} u(x,z,t)\,\mathrm{d}z = O\left(\varepsilon^2\right).$$

Proof. As it was done in [51], the vertical integration of (2.2.2) yields the mass conservation (first equation of (2.2.8)) and the following momentum balance

$$\begin{aligned} \partial_t\left(\int_B^\eta \overline{u}\mathrm{d}z\right) + \nabla_x \cdot \left(\int_B^\eta (u\otimes u + pI_d)\,\mathrm{d}z\right) &= p_{|_{z=\eta}}\nabla_x\eta - p_{|_{z=B}}\nabla_x B \\ -\kappa_B\left(u_{|_{z=B}} - U_B\right) - \mathbb{1}_{h\geq\overline{H}}\kappa_R\left(u_{|_{z=R}} - U_R\right) &+ \nabla_x \cdot \left(\int_B^\eta \sigma_{xx}\mathrm{d}z\right). \end{aligned} \tag{2.2.12}$$

Thanks to Proposition 2.2.1, $\psi_{|z=R}(x,t) = \mathbb{1}_{h\geq\overline{H}}(x,t)$. Let us start by formally identifying a first order approximation. As in [51], the main term of the third equation of (2.2.2) reads $p = p_{|z=\eta} + g(\eta - z) + O(\varepsilon)$. The main term of the second equation of (2.2.2) and the Navier boundary conditions (2.2.5) lead to $u = \overline{u} + O(\varepsilon)$. Injected in (2.2.12), the momentum balance of the congested shallow water model reads at first order

$$\begin{aligned}\partial_t(h\overline{u}) + \nabla_x \cdot \left(h\overline{u}\otimes\overline{u} + \frac{g}{2}h^2 I_d\right) = &-h\nabla_x\left(gB + p_{|z=\eta}\right)\\ &-\kappa_B^0(\overline{u} - U_B) - \mathbb{1}_{h\geq\overline{H}}\kappa_R^0(\overline{u} - U_R).\end{aligned}$$

In order to get a better approximation, the first perturbation terms are taken into account. The vertical momentum equation of (2.2.2) leads to

$$p = p_\eta + g(\eta - z) - 2\varepsilon\mu^0\nabla_x\cdot\overline{u} + O\left(\varepsilon^2\right)$$

where the surface pressure reads $p_\eta = p_{|z=\eta} - 2\varepsilon\mu^0\partial_z w_{|z=\eta}$. Considering the horizontal momentum equation of (2.2.2) and the Navier conditions at the bottom and the roof (2.2.5), the horizontal velocity of (2.2.2) satisfies

$$\begin{cases} \partial_{zz}^2 u &= -\dfrac{\varepsilon}{\mu^0 h}\left(\kappa_B^0(\overline{u} - U_B) + \mathbb{1}_{h\geq\overline{H}}\kappa_R^0(\overline{u} - U_R)\right) + O\left(\varepsilon^2\right)\\ \partial_z u_{|z=B} &= \dfrac{\varepsilon\kappa_B^0}{\mu^0}(\overline{u} - U_B) + O\left(\varepsilon^2\right)\\ \mathbb{1}_{h\geq\overline{H}}\partial_z u_{|z=R} &= -\mathbb{1}_{h\geq\overline{H}}\dfrac{\varepsilon\kappa_R^0}{\mu^0}(\overline{u} - U_R) + O\left(\varepsilon^2\right).\end{cases}$$

By taking into account the definition of $\overline{u}$, one can check that the horizontal velocity of (2.2.2) is under the form

$$u = \frac{\alpha_1}{2}(z - B)^2 + \alpha_2(z - B) + \alpha_3 + O\left(\varepsilon^2\right)$$

with

$$\begin{aligned}\alpha_1 &= -\frac{\varepsilon}{\mu^0 h}\left(\kappa_B^0(\overline{u} - U_B) + \mathbb{1}_{h\geq\overline{H}}\kappa_R^0(\overline{u} - U_R)\right),\\ \alpha_2 &= \frac{\varepsilon}{\mu^0}\kappa_B^0(\overline{u} - U_B),\\ \text{and}\quad \alpha_3 &= \overline{u} + \frac{\varepsilon h}{\mu^0}\left(\mathbb{1}_{h\geq\overline{H}}\frac{\kappa_R^0}{6}(\overline{u} - U_R) - \frac{\kappa_B^0}{3}(\overline{u} - U_B)\right).\end{aligned}$$

Inserted in (2.2.12), the shallow water model (2.2.8) follows, provided we define U and κ by (2.2.11).

It remains to establish (2.2.9) and (2.2.10). A direct consequence of Proposition 2.2.1 leads to $B \leq \eta \leq R$ and thus to the congestion constraint (2.2.9). Similarly, the non-negativity of the relative pressure (2.2.7) implies $p_\eta \geq P_{|_{z=\eta}}$. Introducing the first equation of (2.2.6) into the second equation of (2.2.6) gives

$$(1 - \mathbb{1}_{\eta \geq R}) \left(p_\eta - P_{|_{z=\eta}}\right) = O\left(\varepsilon^2\right).$$

We get the expected constraint (2.2.10). □

The two cases in the definition of $\widetilde{\kappa_B}$ and $\widetilde{\kappa_R}$ are chosen to get positive parameters whatever the water depth. More precisely, both correspond to the same approximation at order $O(\varepsilon^2)$. It follows that the effective friction parameter κ is always positive.

2.2.1.3 Preliminary analysis of the congested shallow water model

Let us mention some mathematical properties of the congested shallow water model. The objective is to highlight the physical relevance of the model (2.2.8)-(2.2.10). For a deeper analysis, we refer to [73]. In particular, the dissipation of mechanical energy is a crucial point for many applications such as renewable energy production using buoys. From the mathematical point of view, the energy balance, acting as a mathematical entropy, is an argument for the existence of long time solutions. In addition the conservation of the steady state, in particular the lake at rest, is relevant for many applications because the flow is close to this state. To characterize these two properties, the potential of the conservative forces defined by

$$\phi = g(h + B) + P_\eta \tag{2.2.13}$$

is a useful quantity.

Proposition 2.2.3. *Any smooth enough solution of the congested shallow water model (2.2.8)-(2.2.10) satisfies the following energy balance law*

$$\begin{aligned}\partial_t \mathcal{E} + \nabla_x \cdot \mathcal{G} = &- (p_\eta - P_\eta)\, \partial_t \overline{H} + h \partial_t (gB + P_\eta) \\ &- \frac{\kappa}{2} \left(\|\overline{u}\|^2 - \|U\|^2 + \|\overline{u} - U\|^2\right) - 2\overline{\mu} h \left(\|D_x(\overline{u})\|^2 + |\nabla_x \cdot \overline{u}|^2\right)\end{aligned}$$

with the mechanical energy $\mathcal{E} = \mathcal{K} + \mathcal{P}$, the kinetic energy and the potential energy respectively given by

$$\mathcal{K} = \frac{1}{2} h \|\overline{u}\|^2 \qquad \text{and} \qquad \mathcal{P} = gh\left(B + \frac{h}{2}\right) + hP_\eta$$

and the energy flux

$$\mathcal{G} = \left(\frac{1}{2} \|\overline{u}\|^2 + g\left(h + B\right) + p_\eta - 2\overline{\mu}\left(\nabla_x \cdot \overline{u} + D_x\left(\overline{u}\right)\right) \right) h\overline{u}.$$

Proof. The kinetic energy balance law is obtained by multiplying the momentum balance of (2.2.8) by the mean velocity $\overline{u}$ which gives

$$\begin{aligned} \partial_t \mathcal{K} + \nabla_x \cdot \left(\mathcal{K} - 2\overline{\mu} h \left(\nabla \cdot \overline{u} + D_x\left(\overline{u}\right)\right) \overline{u}\right) = -h\overline{u} \cdot \nabla_x \left(\phi + p_\eta - P_\eta\right) \\ -\frac{\kappa}{2}\left(\|\overline{u}\|^2 - \|U\|^2 + \|\overline{u} - U\|^2\right) - 2\overline{\mu} h \left(\|D_x\left(\overline{u}\right)\|^2 + |\nabla_x \cdot \overline{u}|^2\right) \end{aligned}$$

with ϕ defined by (2.2.13). Furthermore, the potential energy balance law is obtained by multiplying the mass conservation of (2.2.8) by the potential ϕ. It yields

$$\begin{aligned} \partial_t \mathcal{P} + \nabla_x \cdot \left(\left(\phi + p_\eta - P_\eta\right) h\overline{u}\right) &= h\overline{u} \cdot \nabla_x \phi + \nabla_x \cdot \left(\left(p_\eta - P_\eta\right) h\overline{u}\right) \\ &\quad + h\partial_t \left(gB + P_\eta\right). \end{aligned}$$

Summing the two energy balance laws, it remains to estimate the source term

$$\left(p_\eta - P_\eta\right) \nabla_x \cdot \left(h\overline{u}\right) = -\left(p_\eta - P_\eta\right) \partial_t \left(h - \overline{H}\right) - \left(p_\eta - P_\eta\right) \partial_t \overline{H}.$$

Eventually, considering the constraint (2.2.10), we get

$$0 = \partial_t \left(\left(p_\eta - P_\eta\right)\left(h - \overline{H}\right)\right) = \left(p_\eta - P_\eta\right) \partial_t \left(h - \overline{H}\right) + \left(h - \overline{H}\right) \partial_t \left(p_\eta - P_\eta\right)$$

which since $p_\eta - P_\eta = 0$ or $h - \overline{H} = 0$ implies that

$$\left(p_\eta - P_\eta\right) \partial_t \left(h - \overline{H}\right) = 0.$$

□

The congested shallow water model (2.2.8)-(2.2.10) admits the following lake at rest solution, i.e. a steady solution with a vanishing velocity. To provide an expression of it, we use the positive part function defined by $(\psi)_+ = \dfrac{|\psi| + \psi}{2}$ and we consider a uniform potential of conservative forces ϕ_0.

Proposition 2.2.4. *Let $\partial_t R = \partial_t B = \partial_t P_\eta = U = 0$. Then for any $\phi_0 \in \mathbb{R}$, the lake at rest defined by*

$$\overline{u} = 0 \qquad \text{and} \qquad h = \min\left(\left(\frac{\phi_0 - P_\eta}{g} - B\right)_+, \overline{H}\right) \tag{2.2.14}$$

is a steady solution of (2.2.8)-(2.2.10) and the surface pressure reads

$$p_\eta = P_\eta + \mathbb{1}_{\phi_0 \geq g\left(B + \overline{H}\right) + P_\eta} \left(\phi_0 - gR - P_\eta\right).$$

Proof. The lake at rest solution defined by (2.2.14) satisfies

$$h\left(g\left(B+h\right)+p_\eta-\phi_0\right)=0.$$

In addition, since $\overline{u}=0$, we conclude that $\partial_t\left(h\overline{u}\right)=0$ and $\partial_t h=0$. Eventually, it is clear that the lake at rest (2.2.14) ensures the congestion constraint (2.2.9) and (2.2.10). □

The lake at rest is not the only steady solution of (2.2.8)-(2.2.10). However, it is the simplest one. Some works in the literature consider more complex steady states [30; 64; 86; 88].

2.2.2 Relaxation of the congestion constraint

Due to the congestion constraint (2.2.9), the congested shallow water model is difficult to handle analytically as well as numerically. For this reason, we propose new formulations of the congestion constraint. In the context of incompressible fluid dynamics, several strategies were proposed in the literature to deal with a divergence free constraint. These strategies require that the constraint is written under the form of a divergence. Thus let us first write the unilateral constraint of the congested shallow water model under the form of a divergence. In such a context, the surface pressure p_η acts as a Lagrange multiplier in the congested areas.

Proposition 2.2.5. *Assume that h is smooth enough and $h^0\left(x\right)\leq\overline{H}\left(x,0\right)$. Then the following constraints*

i) $h\leq\overline{H}$

ii) $\mathbb{1}_{h\geq\overline{H}}\left(\partial_t\overline{H}+\nabla_x\cdot\left(h\overline{u}\right)\right)=0$

iii) $\partial_t\left(h-\overline{H}\right)_+=0$

are equivalent for any solution of (2.2.8) *and* (2.2.10).

Proof. Let $\left(h,\overline{u},p_\eta\right)$ be solution of (2.2.8) and (2.2.10).

- i)⇒ii): Assume i). Multiplying the mass conservation equation of (2.2.8) by the indicator function for $h\geq\overline{H}$, the constraint ii) is recovered since in the congested area we have $h=\overline{H}$.

- ii)⇒iii): Assume ii). Using the mass conservation, the constraint becomes $\mathbb{1}_{h\geq\overline{H}}\partial_t\left(h-\overline{H}\right)=0$.

- iii)⇒i): Assume iii). Since $h^0(x) \leq \overline{H}(x,0)$, iii) leads to i).

□

Remark 2.2.1. *Once the congestion constraint is under the divergence form ii) of Proposition 2.2.5, one can remark that in the congested area, i.e. $h = \overline{H}$, the surface pressure satisfies*

$$\begin{aligned} -\nabla_x \cdot (h \nabla_x p_\eta) = \nabla_x \cdot \left(\nabla_x \cdot \left(h\overline{u} \otimes \overline{u} + \frac{g}{2} h^2 I_d \right) + gh \nabla_x B \right) \\ + \nabla_x \cdot (\kappa (\overline{u} - U)) - \partial_{tt}^2 \overline{H} - 2\overline{\mu} \nabla_x \cdot (\nabla_x \cdot (h D_x(\overline{u})) + \nabla_x (h \nabla_x \cdot \overline{u})) . \end{aligned} \tag{2.2.15}$$

In order to recover the surface pressure from (2.2.15), boundary conditions are required. In [73], the continuity of the surface pressure is assumed. However, this strategy assumes a smooth enough flow, which is not always satisfied since hyperbolic models can lead to discontinuous solutions, see Section 2.3.2.3. In addition, this strategy requires the description of the interface position which is a challenging issue since the interface is strongly linked to the flow dynamics.

The relaxation method is a strategy frequently used to approximate the divergence free constraint, see [34; 103]. We introduce $\lambda > 0$ the relaxation parameter, characterizing the amplitude of the penetration in the roof. Let us write the approximate model

$$\begin{cases} \partial_t h_\lambda + \nabla_x \cdot (h_\lambda \overline{u}_\lambda) & = 0 \\ \partial_t (h_\lambda \overline{u}_\lambda) + \nabla_x \cdot \left(h_\lambda \overline{u}_\lambda \otimes \overline{u}_\lambda + \frac{g}{2} h_\lambda^2 I_d \right) & = -h_\lambda \nabla_x (gB + p_\lambda) - \kappa (\overline{u}_\lambda - U) \\ & \quad + 2\overline{\mu} \nabla_x \cdot (h_\lambda D_x(\overline{u}_\lambda)) \\ & \quad + 2\overline{\mu} \nabla_x (h_\lambda \nabla_x \cdot \overline{u}_\lambda) \end{cases} \tag{2.2.16}$$

completed with the initial conditions

$$h_\lambda(x,0) = h_\lambda^0(x) \qquad \text{and} \qquad \overline{u}_\lambda(x,0) = \overline{u}_\lambda^0(x) .$$

The unknowns of (2.2.16) are h_λ the approximated water depth which does not exactly satisfy (2.2.9) and $\overline{u}_\lambda$ the approximated vertical-averaged horizontal velocity. The unknown surface pressure p_η in (2.2.8) is replaced by p_λ which is taken as an implicit function of h_λ. More precisely, we assume

$$\lambda^2 \mathcal{L}(p_\lambda - P_\eta) = g \mathbb{1}_{h \geq \overline{H}} \left(\partial_t \overline{H} + \nabla_x \cdot (h\overline{u}) \right) . \tag{2.2.17}$$

We assume that the relaxation operator $\mathcal{L} : \Psi \mapsto \mathcal{L}(\Psi)$ is invertible. However since choosing, for example, $\mathcal{L} = -\Delta_x$ needs to specify a boundary value problem, we will not discuss the domain of definition and the domain of

invertibility of the operator $\mathcal{L}$ in the general case and we start by discussing the choice of $\mathcal{L}$. Classically the regularization operator $\mathcal{L}$ is chosen among I_d, $-\Delta_x$, ∂_t or $-\partial_t\Delta_x$, see [100] where these operators are presented in the context of Navier-Stokes equations. However, this list is not exhaustive. Since the congestion constraint can be written under the form of a time derivative, see iii) of Proposition 2.2.5, it seems interesting to choose $\mathcal{L}$ under the form

$$\mathcal{L}(\Psi) = \partial_t\left(\widetilde{\mathcal{L}}(\Psi)\right)$$

with $\widetilde{\mathcal{L}}$ an operator chosen among I_d or $-\Delta_x$. Then $\widetilde{\mathcal{L}}$ is invertible and $\widetilde{\mathcal{L}}^{-1}$ is a strictly positive map. We will however skip the theoretical details and do not precise the spaces on which this property holds when $\widetilde{\mathcal{L}} \neq I_d$. Note that with this choice, an additional initial condition on the surface pressure $p_\lambda(x,0) = p_\lambda^0(x)$ is required and is not provided by (2.2.8). However, the equation (2.2.17) can be integrated in time. More precisely choosing the initial condition on p_λ such that

$$\lambda^2\widetilde{\mathcal{L}}\left(p_\lambda^0(x) - P_\eta(x,0)\right) = g\left(h_\lambda^0(x) - \overline{H}(x,0)\right)_+$$

the surface pressure reads for any $(x,t) \in \mathbb{R}^{d-1}\times\mathbb{R}_+$

$$\lambda^2\widetilde{\mathcal{L}}\left(p_\lambda(x,t) - P_\eta(x,t)\right) = g\left(h_\lambda(x,t) - \overline{H}(x,t)\right)_+. \tag{2.2.18}$$

This choice corresponds to a pseudo-compressible approximation, see [100]. In the context of incompressible fluid dynamics, the convergence of the approximate model to the constrained model when λ goes to 0 using the classical regularization operators cited above, can be mathematically proven and the error introduced by the relaxation can be estimated, see for example [98].

The regularization operator $\mathcal{L}$ should be chosen in order to preserve the lake at rest solution, see Proposition 2.2.4 as well as the positivity of the relative pressure (2.2.10). In addition, the regularization operator should ensure the dissipation of the mechanical energy given in Proposition 2.2.3. In the following the latter properties are proven in the case of pseudo-compressible approximation (2.2.18). To characterize these properties, the potential of the conservative forces, which now writes (see (2.2.13))

$$\phi_\lambda = g(h_\lambda + B) + p_\lambda,$$

is again introduced. Let us start by a result on the energy balance. We skip the proof which is similar to the proof of Proposition 2.2.3.

Proposition 2.2.6. *For smooth enough solutions of* (2.2.16) *and* (2.2.18), *the following dissipation law holds*

$$\begin{aligned}\partial_t \mathcal{E}_\lambda + \nabla_x \cdot \mathcal{G}_\lambda = &- (p_\lambda - P_\eta)\, \partial_t \overline{H} + h_\lambda \partial_t (gB + P_\eta) \\ &- \frac{\kappa}{2} \left(\|\overline{u}_\lambda\|^2 - \|U\|^2 + \|\overline{u}_\lambda - U\|^2 \right) - 2\overline{\mu} h_\lambda \left(\|D_x(\overline{u}_\lambda)\|^2 + |\nabla_x \cdot \overline{u}_\lambda|^2 \right)\end{aligned}$$

with the mechanical energy $\mathcal{E}_\lambda = \mathcal{K}_\lambda + \mathcal{P}_\lambda$, *the kinetic energy and the potential energy respectively given by*

$$\mathcal{K}_\lambda = \frac{1}{2} h_\lambda \|\overline{u}_\lambda\|^2 \qquad \text{and} \qquad \mathcal{P}_\lambda = g h_\lambda \left(B + \frac{h_\lambda}{2} \right) + h_\lambda P_\eta + \mathcal{R}(h_\lambda),$$

the potential energy relative to the regularization $\mathcal{R}(\psi)$ *such that*

$$\mathrm{d}_\psi \mathcal{R} = \widetilde{\mathcal{L}}^{-1} \left(\frac{g}{\lambda^2} \left(\psi - \overline{H} \right)_+ \right)$$

and the flux of energy

$$\mathcal{G}_\lambda = \left(\frac{1}{2} \|\overline{u}_\lambda\|^2 + g(h_\lambda + B) + p_\lambda - 2\overline{\mu} \left(\nabla_x \cdot \overline{u}_\lambda + D_x(\overline{u}_\lambda) \right) \right) h_\lambda \overline{u}_\lambda.$$

Let us now prove the positivity of the relative pressure (2.2.10).

Proposition 2.2.7. *The solution of* (2.2.16) *and* (2.2.18) *satisfies*

$$\left(1 - \mathbb{1}_{h_\lambda \geq \overline{H}} \right) (p_\lambda - P_\eta) = 0 \qquad \text{and} \qquad p_\lambda \geq P_\eta.$$

Proof. The positivity of the relative pressure is easy to obtain from the expression (2.2.18) of the surface pressure. Now multiplying (2.2.18) by the indicator function of the areas where the water does not reach the roof yields

$$\left(1 - \mathbb{1}_{h_\lambda \geq \overline{H}} \right) (p_\lambda - P_\eta) = \left(1 - \mathbb{1}_{h_\lambda \geq \overline{H}} \right) \widetilde{\mathcal{L}}^{-1} \left(\frac{g}{\lambda^2} \left(h_\lambda - \overline{H} \right)_+ \right).$$

We conclude since $\widetilde{\mathcal{L}}^{-1}$ is a strictly positive map. □

Eventually, the conservation of the lake at rest is highlighted.

Proposition 2.2.8. *Assume* $\partial_t R = \partial_t B = \partial_t P = U = 0$. *Then for any* $\phi_0 \in \mathbb{R}$, *the lake at rest defined by* $\overline{u}_\lambda = 0$ *and*

$$h_\lambda = \begin{cases} \left(\dfrac{\phi_0 - P_\eta}{g} - B \right)_+, & \text{if } \phi_0 \leq g\left(\overline{H} + B \right) + P_\eta \\ \left(I_d + \lambda^2 \widetilde{\mathcal{L}} \right)^{-1} \left(\overline{H} + \lambda^2 \widetilde{\mathcal{L}} \left(\dfrac{\phi_0 - P_\eta}{g} - B \right) \right), & \text{else} \end{cases} \tag{2.2.19}$$

is a steady solution of (2.2.16) *and* (2.2.18) *and*

$$p_\lambda = \max\left(\phi_0 - g(B + h_\lambda), P_\eta \right).$$

Proof. Let us first consider the case where $\phi_0 > g\left(\overline{H} + B\right) + P_\eta$. Starting from $h_\lambda + \lambda^2 \widetilde{\mathcal{L}}(h_\lambda)$ using (2.2.19), we get

$$\lambda^2 \widetilde{\mathcal{L}}\left(\phi_0 - g\left(B + h_\lambda\right) - P_\eta\right) = g\left(h_\lambda - \overline{H}\right).$$

Using (2.2.18) it leads to

$$\lambda^2 \widetilde{\mathcal{L}}\left(\phi_0 - g\left(B + h_\lambda\right) - P_\eta\right) = \lambda^2 \widetilde{\mathcal{L}}\left(p_\lambda(x,t) - P_\eta(x,t)\right)$$

and composing by $\widetilde{\mathcal{L}}^{-1}$ we get $p_\lambda = \phi_0 - g\left(B + h_\lambda\right)$ then $\phi_\lambda = \phi_0$.
In the case where $\phi_0 \leq g\left(\overline{H} + B\right) + P_\eta$, (2.2.19) leads to $\phi_0 = g\left(h_\lambda + B\right) + P_\eta$. Moreover (2.2.18) leads to $p_\lambda = P_\eta$. Thus we finally get $\phi_\lambda = \phi_0$.
In addition, since $\overline{u}_\lambda = 0$, we conclude that $\partial_t\left(h_\lambda \overline{u}_\lambda\right) = 0$ and $\partial_t h_\lambda = 0$. □

At the limit $\lambda \to 0$, one can check that the state (2.2.19) tends to the state (2.2.14). It is a (very weak) argument to claim that (2.2.16) and (2.2.18) is a consistent approximation of (2.2.8)-(2.2.10). It is consistent (as $\lambda \to 0$) at least for some steady solutions.

To conclude, the pseudo-compressibility method seems a suitable approximation of the congested shallow water model (2.2.8)-(2.2.10). In particular, the simplest pseudo-compressibility method leading to an approximation satisfying the properties of the congested shallow water model (2.2.8)-(2.2.10) is given by $\widetilde{\mathcal{L}} = I_d$. In addition, in this case, (2.2.18) gives an explicit function for the surface pressure

$$p_\lambda(h_\lambda) = P_\eta + g\frac{\left(h_\lambda - \overline{H}\right)_+}{\lambda^2}. \tag{2.2.20}$$

Substituting it in (2.2.16) leads to

$$\begin{cases} \partial_t h_\lambda + \nabla_x \cdot \left(h_\lambda \overline{u}_\lambda\right) & = 0 \\ \partial_t\left(h_\lambda \overline{u}_\lambda\right) + \nabla_x \cdot \left(h_\lambda \overline{u}_\lambda \otimes \overline{u}_\lambda + \dfrac{g}{2} h_\lambda^2 I_d\right) & = -g h_\lambda \nabla_x \left(\dfrac{\left(h_\lambda - \overline{H}\right)_+}{\lambda^2}\right) \\ & \quad +2\overline{\mu}\nabla_x \cdot \left(h D_x\left(\overline{u}_\lambda\right)\right) \\ & \quad +2\overline{\mu}\nabla_x\left(h \nabla_x \cdot \overline{u}_\lambda\right) \\ & \quad -\kappa\left(\overline{u}_\lambda - U\right) - h_\lambda \nabla_x\left(gB + P_\eta\right). \end{cases} \tag{2.2.21}$$

One can note the similarity between (2.2.21) and the classical Euler model at the low-Froude regime [58]. The convergence to the 'incompressible' limit ($\lambda \to 0$) is studied in [67; 68] in the context of compressible fluid flow.
Besides, the approximate model (2.2.21) is close to the Partially Free Surface

model (PFS) proposed in [23]. Both models are able to switch between the congested areas and the free surface domain without following the interface and the surface pressure is an explicit function of the water depth. In [23], the authors link the parameter λ to a physical parameter such as the speed of sound in the water whereas it is a mathematical artifice here. As for the PFS model, one can show that the approximate model (2.2.21) is hyperbolic.

Proposition 2.2.9. *Assume that* $\partial_t B = \nabla_x B = \partial_t R = \nabla_x R = \kappa = \overline{\mu} = 0$, $\lambda > 0$ *and* $h_\lambda > 0$. *Then the model* (2.2.21) *is strictly hyperbolic.*
More precisely, denoting $\overline{u}_N = \overline{u}_\lambda \cdot N$ *with a unit vector* $N \in \mathbb{R}^{d-1}$, *the eigenvalues in the direction* N *are* $\overline{u}_N - c < \overline{u}_N < \overline{u}_N + c$ *with* $c = \sqrt{\left(1 + \frac{\mathbb{1}_{h_\lambda \geq \overline{H}}}{\lambda^2}\right) g h_\lambda}$.

Proof. The proof is similar to the classical shallow water case. The approximate model (2.2.21) can be written as $\partial_t W + J_x \partial_x W + J_y \partial_y W = 0$ with $W = (h_\lambda, \overline{u}_x, \overline{u}_y)^t$, the Jacobians

$$J_x = \begin{pmatrix} \overline{u}_x & h_\lambda & 0 \\ \left(1 + \frac{\mathbb{1}_{h_\lambda \geq \overline{H}}}{\lambda^2}\right) g & \overline{u}_x & 0 \\ 0 & 0 & \overline{u}_x \end{pmatrix} \quad \text{and} \quad J_y = \begin{pmatrix} \overline{u}_y & 0 & h_\lambda \\ 0 & \overline{u}_y & 0 \\ \left(1 + \frac{\mathbb{1}_{h_\lambda \geq \overline{H}}}{\lambda^2}\right) g & 0 & \overline{u}_y \end{pmatrix}.$$

The eigenvalues in the direction N being the eigenvalues of the matrix $J_x N_x + J_y N_y$, we conclude by simple computations. □

2.3 Numerical resolution

The current section is devoted to the numerical approximation of the congested shallow water model (2.2.8)-(2.2.10). Following the strategy proposed in Section 2.2.2, the numerical approach is based on a discretization of the hyperbolic model (2.2.21) at the regime $\lambda \ll 1$. We recall that the model (2.2.21) came from a particular choice of $\mathcal{L}$, which leads, in addition of the mandatory characteristics of the approximate model , i.e. an energy estimation, the positiveness of the relative pressure and the steady state preservation, to an explicit formula for the pressure (2.2.20). Another choice of $\mathcal{L}$ would be less efficient numerically since Newton's fixed point explained hereafter would become less straightforward. From now on, the dissipative terms are neglected, i.e. $\kappa = \overline{\mu} = 0$. More precisely, the numerical strategy is based on an operator splitting between the hyperbolic part of the equation and the dissipative terms. We only detail the discretization of the hyperbolic part of the model since the dissipative step might be solved using an usual implicit scheme.

The numerical strategy used to solve the approximate model (2.2.21) has to be consistent with the 'incompressible' regime $\lambda \ll 1$. More precisely, in the congested areas, this corresponds to high potential regime since the second term in (2.2.20) becomes large. By analogy with gas dynamics, this corresponds to the low-Mach regime, see [67; 68]. Classical Godunov solvers are known to be too much dissipative in this case and to require a very restrictive CFL condition, see [40; 58]. Several schemes in the literature are designed to recover the 'incompressible' regime, see [32; 62; 90].

In addition, a particular attention is given to the preservation of the lake at rest solution. Even more important than in the case of the classical shallow water model, the conservation of the lake at rest at the numerical level, using so-called well-balanced schemes [4; 11; 56], is a required property for the simulation of the model (2.2.21).

More precisely, if a scheme is not well-balanced and does not preserve the lake at rest, it will create oscillations, of order of the space step, at the free surface. However, the scheme is still consistent with the classical shallow water model. In the case of the congested shallow water model, small oscillations can artificially separate the surface from the roof and lead to strong variations of the surface pressure.

Most of the schemes designed to be consistent in the 'incompressible' regime do not care about steady states at rest. More precisely, this regime is usually analyzed for the low-Mach regime of the Euler equations without source term or with a source term constant in space such as gravity. However, the Centered-Potential Regularization (CPR) scheme introduced in [90] satisfies the two requirements: consistency with the 'incompressible' regime and the well-balanced property. The numerical strategy presented in the following is an adaptation of the CPR scheme to take into account the congestion constraint.

2.3.1 The CPR scheme adapted to the congested shallow water model

Let $\mathbb{T}$ be a mesh of Ω_x composed of star-shaped control volumes, see Figure 2.2. We denote $k \in \mathbb{T}$ a control volume, $\mathbb{F}_k$ the set of its faces, $|k|$ its volume and $|\partial k|$ its surface area. Furthermore for a face f, its area is denoted $|f|$ and k_f is the neighbor control volume of k such that $k \cap k_f = f$. The space step is defined by $l_k = \frac{|k|}{|\partial k|}$ and the normalized face size by $\nu_f^k = \frac{|f|}{|\partial k|}$. The unit normal to f outward to k is denoted as N_f^k. The set of the faces at the boundary of the mesh is designed by $\mathbb{F}_{\partial\mathbb{T}}$. In addition, the time step is denoted by δ_t^{n+1}, i.e. $t^{n+1} = t^n + \delta_t^{n+1}$.

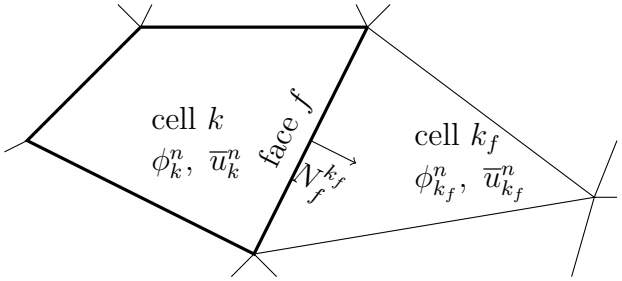

Figure 2.2 – Numerical notations for the two dimensional case, i.e. $d = 3$

2.3.1.1 Description of the CPR scheme

The CPR scheme is an IMplicit-EXplicit finite volume method. The numerical unknowns are approximations of the average in a control volume k of the variables. The mean atmospheric pressure, the mean bottom level, the mean roof level and the mean opening in the control volume k and at time t^n are respectively denoted by P_k^n, B_k^n, R_k^n and $\overline{H}_k^n = R_k^n - B_k^n$. One particularity of the CPR scheme is that the numerical unknowns are not the conserved variables, they are chosen as the potential ϕ_k^n and the horizontal velocity $\overline{u}_k^n$. This choice of variables is particularly well adapted to the congested shallow water model since the potential can be used as a parametrization of the water depth h_k^n and the surface pressure p_k^n. More precisely, we recall that the potential reads $\phi_\lambda = g\left(h_\lambda + B\right) + p_\lambda$ and we set

$$h\left(k, n; \phi\right) = \begin{cases} \dfrac{\phi - P_k^n}{g} - B_k^n, & \text{if } \phi \leq g\left(\overline{H}_k^n + B_k^n\right) + P_k^n \\ \dfrac{\overline{H}_k^n + \lambda^2\left(\frac{\phi - P_k^n}{g} - B_k^n\right)}{1 + \lambda^2}, & \text{else} \end{cases} \tag{2.3.1}$$

and

$$p\left(k, n; \phi\right) = \phi - g\left(h\left(k, n; \phi\right) + B_k^n\right). \tag{2.3.2}$$

For readability, we set $h_k^n = h\left(k, n; \phi_k^n\right)$ and $p_k^n = p\left(k, n; \phi_k^n\right)$.

Using an implicit finite volume method, the mass conservation, first equation of (2.2.21), reads

$$h_k^{n+1} = h_k^n - \frac{\delta_t^{n+1}}{l_k} \sum_{f \in \mathbb{F}_k} \mathcal{F}_f^{n+1} \cdot N_f^k \nu_f^k \tag{2.3.3}$$

with $\mathcal{F}_f^{n+1}$ an approximation of the mean mass flux $h_\lambda \overline{u}_\lambda$ at the face f between

the times t^n and t^{n+1}. More precisely if $f \notin \mathbb{F}_{\partial\mathbb{T}}$, we set

$$\mathcal{F}_f^{n+1} = \left(h^{n+1}\overline{u}^n\right)_f - \gamma\delta_t^{n+1}\left(\frac{h^{n+1}}{l}\right)_f \left[\phi^{n+1}\right]_k^{k_f} N_f^k$$

with a regularization parameter $\gamma \geq 0$ characteristic of the CPR scheme, called CPR-parameter in the sequel, see [90]. We have also introduced the following notation at the face

$$(\psi)_f = \frac{\psi_k + \psi_{k_f}}{2} \qquad \text{and} \qquad [\psi]_k^{k_f} = \frac{\psi_{k_f} - \psi_k}{2}.$$

If $f \in \mathbb{F}_{\partial\mathbb{T}}$, the numerical scheme requires boundary conditions which depend on the regime of the flow. In the current work, we do not detail the boundary conditions treatment (For a hyperbolic system it is known to be a difficult point, see [46] for more details). The scheme (2.3.3) is an implicit and non-linear scheme on the potential, thus it cannot be solved directly. An iterative Newton process is used to solve it at each time step. More precisely, writing the scheme as $S_k\left(\phi^{n+1}\right) = 0$ with

$$\begin{aligned} S_k(\phi) &= h(k, n+1; \phi) - h_k^n \\ &+ \frac{\delta_t^{n+1}}{l_k} \sum_{f \in \mathbb{F}_k} \left(\left(h(k, n+1; \phi)\,\overline{u}^n\right)_f \cdot N_f^k - \gamma\delta_t^{n+1}\left(\frac{h(k, n+1; \phi)}{l}\right)_f [\phi]_k^{k_f} \right) \nu_f^k, \end{aligned}$$

the Newton method consists in constructing a sequence $\left(\phi^{n,q}\right)_{q\geq 0}$ defined by $\phi^{n,0} = \phi^n$ and

$$\left\{ \begin{array}{lcl} \mathcal{J}\left(\phi^{n,q}\right)\delta_\phi^{n,q} & = & \mathcal{S}\left(\phi^{n,q}\right) \\ \phi^{n,q+1} & = & \phi^{n,q} - \delta_\phi^{n,q} \end{array} \right.$$

where $\mathcal{J}$ denotes the Jacobian matrix of $\mathcal{S}(\phi) = \left(S_k(\phi)\right)_{k\in\mathbb{T}}$. Furthermore ϕ^{n+1} is defined as $\lim\limits_{q\to\infty} \phi^{n,q}$. A similar Newton method is analyzed in [26]. Numerically, a quadratic convergence of the Newton method is observed.

Once the potential ϕ_k^{n+1} is recovered, the water depth h_k^{n+1} is known and the momentum balance is computed using the following explicit upwind scheme in order to get $\overline{u}_k^{n+1}$

$$\begin{aligned} h_k^{n+1}\overline{u}_k^{n+1} = h_k^n\overline{u}_k^n &- \frac{\delta_t^{n+1}}{l_k} h_k^{n+1} \sum_{f\in\mathbb{F}_k} \left[\phi^{n+1}\right]_k^{k_f} N_f^k \nu_f^k \\ &- \frac{\delta_t^{n+1}}{l_k} \sum_{f\in\mathbb{F}_k} \left(\overline{u}_k^n \left(\mathcal{F}_f^{n+1}\cdot N_f^k\right)_+ - \overline{u}_{kf}^n \left(\mathcal{F}_f^{n+1}\cdot N_f^k\right)_- \right) \nu_f^k. \end{aligned} \tag{2.3.4}$$

Eventually, the discrete surface pressure can be estimated a posteriori for output using (2.3.2).

Remark that thanks to the definition of the variables (2.3.1)-(2.3.2), in particular the choice of ϕ instead of h, the scheme (2.3.3) and (2.3.4) can be used in practice with λ set to 0. In other words, there is no more penetration in the roof and the congestion constraint (2.2.9) is exactly satisfied. In the next section, we first propose an analysis with $\lambda > 0$ then we investigate the case $\lambda = 0$ numerically in the simulations.

2.3.1.2 Numerical analysis

In the following section, the numerical counterpart of the main properties of the congested shallow water model is established. In particular, the dissipation of the mechanical energy in Proposition 2.2.6, acts as a mathematical entropy and proves the numerical stability of the scheme. Firstly, let us recall the main numerical properties inherited from the CPR scheme, before showing the properties specific to the congested shallow water model.

Let us start by a consistency result valid on a regular cartesian grid. We denote by δ_x the uniform space step, i.e. the distance between the center of two neighboring cells. In this particular case the coordinates of the center of each cell are denoted by x_k.

Proposition 2.3.1 (Consistency)**.** *Let λ and γ be fixed. Then for smooth enough solutions and a regular cartesian grid we have*

$$|h_k^n - h_\lambda(x_k, t^n)| = O(\delta_t, \delta_x)$$

and

$$\|h_k^n \overline{u}_k^n - h_\lambda(x_k, t^n)\, \overline{u}_\lambda(x_k, t^n)\| = O(\delta_t, \delta_x).$$

Proof. The proof is done in [90, Proposition 2.2]. □

Proposition 2.3.2. *The scheme (2.3.3) and (2.3.4) satisfies the following properties*

i) (Positivity of water depth) Assume $h_k^0 > 0$ for any $k \in \mathbb{T}$ and assume that the following implicit CFL condition is satisfied for any $n \in \mathbb{N}$

$$\left(\left| \overline{u}_f^n \cdot N_f^k \right| + \sqrt{\frac{\gamma}{2}} \sqrt{\left| [\phi^{n+1}]_k^{k_f} \right|} \right) \delta_t^{n+1} \leq \frac{\min\left(h_k^{n+1}, h_{k_f}^{n+1}\right)}{h_k^{n+1} + h_{k_f}^{n+1}} \min\left(l_k, l_{k_f}\right). \tag{2.3.5}$$

Then $h_k^n > 0$ for any $k \in \mathbb{T}$ and $n \in \mathbb{N}$.

ii) (Conservation of water volume) For any $n \in \mathbb{N}$,

$$\sum_{k\in\mathbb{T}} |k|\, h_k^{n+1} = \sum_{k\in\mathbb{T}} |k|\, h_k^n - \delta_t^{n+1} \sum_{f\in\mathbb{F}_{\partial\mathbb{T}}} \mathcal{F}_f^{n+1}\cdot N_f^k |f|.$$

iii) (Well-balanced scheme) For any $\phi_0 \in \mathbb{R}$, *let the initial condition be*

$$\phi_k^0 = \phi_0 \qquad \text{and} \qquad \overline{u}_k^0 = 0.$$

Then for any time, the solution of (2.3.3) *and* (2.3.4) *reads*

$$\phi_k^n = \phi_0 \qquad \text{and} \qquad \overline{u}_k^n = 0.$$

Proof. The proofs of i), ii) and iii) are done in [90, Proposition 2.1, Proposition 2.6, Proposition 2.8]. □

One can check that the discrete lake at rest iii) defined in Proposition 2.3.2 is a discrete version of the lake at rest of Proposition 2.2.8.

Note that the CFL condition (2.3.5) cannot be satisfied at a wet-dry interface. In practice the simulation of the latter can be realised by taking artificially some small time step but the scheme will not satisfy the dissipation law given below in Proposition 2.3.3.

Let us now show some properties in the case of the congested shallow water model.

Proposition 2.3.3. *For any* $\gamma \geq 1$ *and under the CFL condition* (2.3.5), *the CPR scheme* (2.3.3) *and* (2.3.4) *satisfies the following dissipation law*

$$\mathcal{E}_k^{n+1} + \frac{\delta_t^{n+1}}{l_k} \sum_{f\in\mathbb{F}_k} \left(\mathcal{G}_{\mathcal{K},f}^{n+1} + \mathcal{G}_{\mathcal{P},f}^{n+1}\right) \nu_f^k \leq \mathcal{E}_k^n + \mathcal{S}_k^{n+1}$$

with the discrete mechanical energy $\mathcal{E}_k^n = \mathcal{K}_k^n + \mathcal{P}_k^n$, *the kinetic energy and the potential energy respectively given by*

$$\mathcal{K}_k^n = \frac{1}{2} h_k^n \|\overline{u}_k^n\|^2 \qquad \text{and} \qquad \mathcal{P}_k^n = g h_k^n \left(B_k^n + \frac{h_k^n}{2}\right) + h_k^n P_k^n + \frac{g}{2\lambda^2} \left(h_k^n - \overline{H}_k^n\right)_+^2,$$

the flux of the kinetic energy

$$\begin{aligned}\mathcal{G}_{\mathcal{K},f}^{n+1} = {} & \frac{1}{2}\|\overline{u}_k^n\|^2 \left(\mathcal{F}_f^{n+1}\cdot N_f^k\right)_+ - \frac{1}{2}\|\overline{u}_{k_f}^n\|^2 \left(\mathcal{F}_f^{n+1}\cdot N_f^k\right)_- \\ & + \frac{\delta_t^{n+1}}{2} \left(\frac{h_{k_f}^{n+1}}{l_{k_f}} - \frac{h_k^{n+1}}{l_k}\right) \left|\left[\phi^{n+1}\right]_k^{k_f}\right|^2,\end{aligned}$$

the flux of the potential energy

$$\mathcal{G}_{\mathcal{P},f}^{n+1} = \phi_f^{n+1}\mathcal{F}_f^{n+1}\cdot N_f^k + \frac{h_k^{n+1}\overline{u}_k^n - h_{k_f}^{n+1}\overline{u}_{k_f}^n}{2}\cdot\left[\phi^{n+1}\right]_k^{k_f} N_f^{k_f}$$

and the source term

$$\mathcal{S}_k^{n+1} = -\left(p_k^{n+1} - P_k^{n+1}\right)\left(\overline{H}_k^{n+1} - \overline{H}_k^n\right) + h_k^n\left(gB_k^{n+1} + P_k^{n+1} - gB_k^n - P_k^n\right).$$

Proof. The following proof is an adaptation of [90, Theorem 2.3]. The estimation of the discrete kinetic energy dissipation law under the CFL condition (2.3.5) established in [90, Lemma 2.4] still holds in our case since it is obtained for any potential. However, the discrete potential energy dissipation law [90, Lemma 2.5] is obtained for a differentiable potential, which is not our case due to the positive part function of the regularization. Let us establish the discrete potential energy balance in our case. Using the two equalities $b_+(b-a) = b_+(b_+ - a_+) + b_+a_-$ where $a_- = a_+ - a$ and $2a(a-b) = a^2 - b^2 + |a-b|^2$, simple calculations lead to

$$\phi_k^{n+1}\left(h_k^{n+1} - h_k^n\right) = \mathcal{P}_k^{n+1} - \mathcal{P}_k^n + \mathcal{Q}_k^{n+1} - \mathcal{S}_k^{n+1}$$

where

$$\begin{aligned}\mathcal{Q}_k^{n+1} = \frac{g}{2}\left|h_k^{n+1} - h_k^n\right|^2 + \frac{g}{2\lambda^2}\left|\left(h_k^{n+1} - \overline{H}_k^{n+1}\right)_+ - \left(h_k^n - \overline{H}_k^n\right)_+\right|^2 \\ + \frac{g}{\lambda^2}\left(h_k^{n+1} - \overline{H}_k^{n+1}\right)_+\left(h_k^n - \overline{H}_k^n\right)_-.\end{aligned}$$

Now multiplying (2.3.3) by ϕ_k^{n+1} and taking into account that $\mathcal{Q}_k^{n+1} \geq 0$ gives the discrete potential energy dissipation law

$$\mathcal{P}_k^{n+1} \leq \mathcal{P}_k^n - \frac{\delta_t^{n+1}}{l_k}\sum_{f\in\mathbb{F}_k}\left(\mathcal{G}_{\mathcal{P},f}^{n+1} - \mathcal{R}_{\mathcal{P},f}^{n+1}\right)\nu_f^k + \delta_t^{n+1}\mathcal{W}_k^{n+1} + \mathcal{S}_k^{n+1}$$

with the rest coming from the space discretization and the work of the conservative forces respectively given by

$$\mathcal{R}_{\mathcal{P},f}^{n+1} = -\gamma\delta_t^{n+1}\left(\frac{h^{n+1}}{l}\right)_f\left|\left[\phi^{n+1}\right]_k^{k_f}\right|^2$$

and

$$\mathcal{W}_k^{n+1} = \frac{h_k^{n+1}\overline{u}_k^n}{l_k}\cdot\sum_{f\in\mathbb{F}_k}\left[\phi^{n+1}\right]_k^{k_f} N_f^k\nu_f^k.$$

Finally, the proof of [90, Theorem 2.3] allows to conclude. □

Note that $\dfrac{S_k^{n+1}}{\delta_t^{n+1}}$ is consistent with the terms depending on a time derivative in the right-hand side of the energy balance law given in Proposition 2.2.6.

Proposition 2.3.4. *The scheme (2.3.3) and (2.3.4) satisfies the following properties*

i) (Positivity of relative pressure) The relative pressure is positive, i.e. for any $k \in \mathbb{T}$ and $n \in \mathbb{N}$

$$\left(1 - \mathbb{1}_{h_k^n < \overline{H}_k^n}\right)\left(p_k^n - P_k^n\right) = 0 \qquad \text{and} \qquad p_k^n \geq P_k^n.$$

ii) (Upper bound on the surface pressure) Assume that for any $f \in \mathbb{F}_{\partial\mathbb{T}}$, we have $\mathcal{F}_f^n = 0$. Then there exists $K \in \mathbb{R}_+^*$ such that for any $\lambda > 0$, we have $p_k^n \leq K$ for any $k \in \mathbb{T}$ and $n \in \mathbb{N}$.

Proof. The proof of i) is a consequence of Proposition 2.2.7.
Let us now prove ii). The mass conservation (2.3.3) at time t^{n+1} reads

$$-\gamma\delta_t^{n+1}\sum_{f\in\mathbb{F}_k}\left(\frac{h^{n+1}}{l}\right)_f\left[\phi^{n+1}\right]_k^{k_f}\nu_f^k + \frac{l_k h_k^{n+1}}{\delta_t^{n+1}} = \frac{l_k h_k^n}{\delta_t^{n+1}} - \sum_{f\in\mathbb{F}_k}\left(h^{n+1}\overline{u}^n\right)_f \cdot N_f^k \nu_f^k.$$

Let us consider the latter equality for all $k \in \mathbb{T}$ and denote ϕ^{n+1} the vector with the components ϕ_k^{n+1} for $k \in \mathbb{T}$. We get a system of the form $M^{n+1}\phi^{n+1} = \Phi$ with M^{n+1} a non-singular M-matrix. Indeed the entries of the main diagonal of M^{n+1} are non-negative, the off-diagonal entries are non-positive and the matrix is strictly diagonally dominant. The system leads to an inequality of the form $\|M^{n+1}\phi^{n+1}\| \leq \Xi^{n+1}$ with $\Xi^{n+1} = \dfrac{l_k h_\infty}{\delta_t^{n+1}} + h_\infty\|\overline{u}_k^n\|$. In fact, thanks to the water volume conservation ii) of Proposition 2.3.2, the water depth is bounded by $0 \leq h_k^n \leq h_\infty$ with $h_\infty = \dfrac{\sum_{k\in\mathbb{T}}|k|h_k^0}{\min_{k\in\mathbb{T}}|k|}$ and the bound on the right hand side follows.
As a consequence, we get a bound on ϕ_k^n and the bound on the surface pressure follows. More precisely, $\forall n \geq 0$, $\max\limits_{k\in\mathbb{T}} p_k^n \leq \max\limits_{k\in\mathbb{T}}\phi_k^n + g\left(h_\infty + \max\limits_{k\in\mathbb{T}} B_k^n\right)$. □

Thanks to ii) from Proposition 2.3.4, we are able to characterize the penetration with respect to λ. More precisely considering (2.2.20), we have

$$\left(h_k^n - \overline{H}_k^n\right)_+ = O\left(\lambda^2\right).$$

It shows that (2.2.9) is verified as λ goes to zero. Furthermore, it shows that the mechanical energy in Proposition 2.3.3 remains bounded when λ tends to 0.

2.3.2 Simulation and numerical validation

The numerical solution of the congested shallow water model is illustrated in a one dimensional framework, i.e. $x \in \mathbb{R}$. Sections 2.3.2.1, 2.3.2.2 and 2.3.2.3 are devoted to stationary solutions. More precisely, simulations of the lake at rest are commented in Section 2.3.2.1. In Section 2.3.2.2, simulations of transcritical steady flow with a free hydraulic jump are compared to an analytical solution. A simulation of a transcritical steady flow with an hydraulic jump constrained by the roof is illustrated in Section 2.3.2.3. Then Sections 2.3.2.4 and 2.3.2.5 are devoted to time-dependent solutions. In Section 2.3.2.4, a time-dependent analytical solution of (2.2.8)-(2.2.10) is given and compared to the numerical solution obtained with (2.3.3)-(2.3.4). Eventually, a simulation in the case of discontinuous velocity is realized in Section 2.3.2.5.

Unless indicated otherwise, for all the test cases $g = 9.81$, $P_\eta = 0$, $\gamma = 1$ and a channel of length $l = 1$ is considered, i.e. $x \in [0, 1]$ where the entry is located at $x = 0$ and the exit at $x = 1$.

2.3.2.1 The lake at rest

The discrete lake at rest iii) of Proposition 2.3.2 is tested and validated in various configurations with bottom and roof which may be continuous or not. Note that in such configurations, the CFL condition (2.3.5) is satisfied for any positive time step. Setting λ to zero, the discrete lake at rest iii) of Proposition 2.3.2 satisfies the constraint (2.2.9) and thus is a discrete version of Proposition (2.2.14). This setting is tested and validated as well.

2.3.2.2 Transcritical steady flow with free hydraulic jump

For any smooth enough bottom and roof, an analytical solution for transcritical steady flow can be obtained as long as the top of the hydraulic jump does not reach the roof. The description of the analytical solution and the algorithm used to compute the solution are described in Appendix A.

Let us consider a roof and a bottom defined by $R(x) = 100(x - 0.5)^2 + 5.8$ and

$$B(x) = \begin{cases} 1, & \text{if } x \leq 0.65 \\ \exp\left(-100(x - 0.65)^2\right), & \text{if } x > 0.65. \end{cases}$$

The water depth at the exit is fixed to $h(l, t) = 8$ and the discharge at the entry is set to $h\overline{u}(0, t) = 40$. The physical parameters are chosen such that the flow is subcritical (fluvial) at the boundaries, but becomes supercritical (torrential) because of the roof.

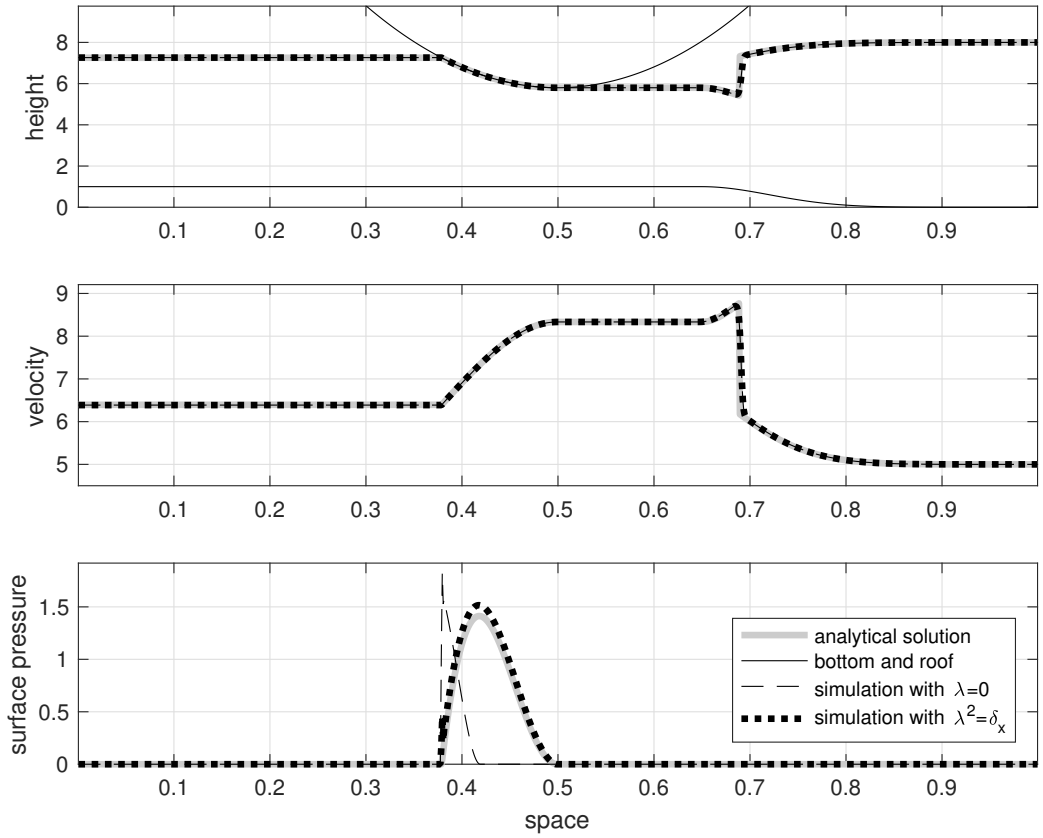

Figure 2.3 – Transcritical steady flow with free hydraulic jump.

The numerical solutions with the parameter $\lambda = 0$ and $\lambda^2 = \delta_x$ together with the analytical solution with regular space step $\delta_x = 10^{-3}$ are plotted in Figure 2.3.

First of all, let us discuss the results with respect to the value of λ. The simulation was performed with several parameters λ from 1 to 0 and for $\delta_x \in \left\{\frac{1}{300}, \frac{1}{1000}, \frac{1}{3000}, \frac{1}{10000}\right\}$. In Figure 2.4 the L^2-errors of the water height, the velocity and the surface pressure are plotted versus λ^2 for the different space steps. We notice that for $\lambda < 1$, the water depth and the velocity are well approximated. The surface pressure is more difficult to obtain. The best agreement with the analytical solution is obtained for $\delta_x \leq \lambda^2 \leq (\delta_x)^{\frac{1}{2}}$. For $\lambda^2 < \delta_x$, the surface pressure is not in good agreement with the analytical solution. Indeed the numerical error of the scheme on the congestion constraint is fully reflected to the surface pressure when λ tends to 0 whereas it is split between the water level and the surface pressure in the case $\lambda > 0$.

Figure 2.5 shows the convergence rates in L^2-norm to the analytical

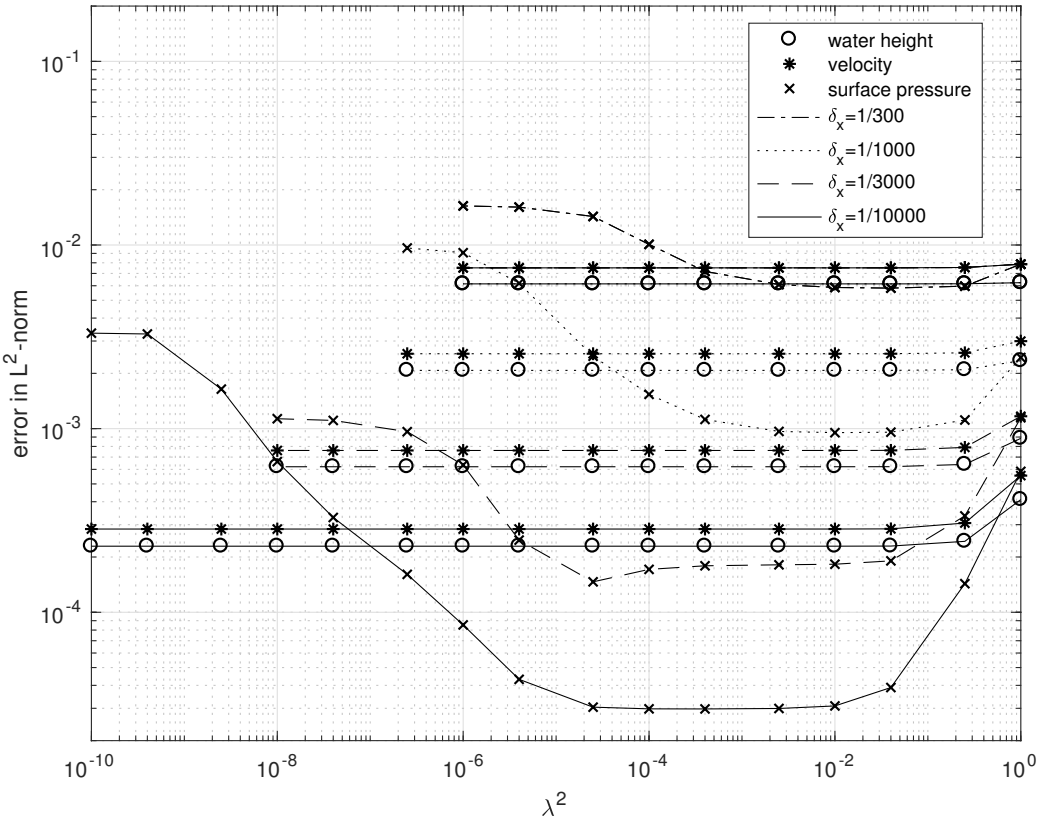

Figure 2.4 – Transcritical steady flow with free hydraulic jump: L^2-errors for the water height, the velocity and the surface pressure versus the parameter λ for different values of the space step δ_x

solution for the water depth, the velocity as well as the surface pressure for $\lambda = 0$ and $\lambda^2 = \delta_x$. In both cases, $\lambda = 0$ and $\lambda^2 = \delta_x$, the water depth and the velocity converge at first order. In the case $\lambda^2 = \delta_x$, the surface pressure converges at approximatively order 1.5, which is faster than expected. Indeed, as the water height converges at first order, the surface pressure is expected to converge at first order as well. In the case $\lambda = 0$, the surface pressure seems to converge but chaotically.

2.3.2.3 Transcritical steady flow with constrained hydraulic jump

The solution presented in Appendix A is not valid when the top of the hydraulic jump reaches the roof. In this case, the non-conservative product $h\nabla_x p_\eta$ is not clearly defined. The following simulation illustrates the solution of the numerical scheme in such a configuration.

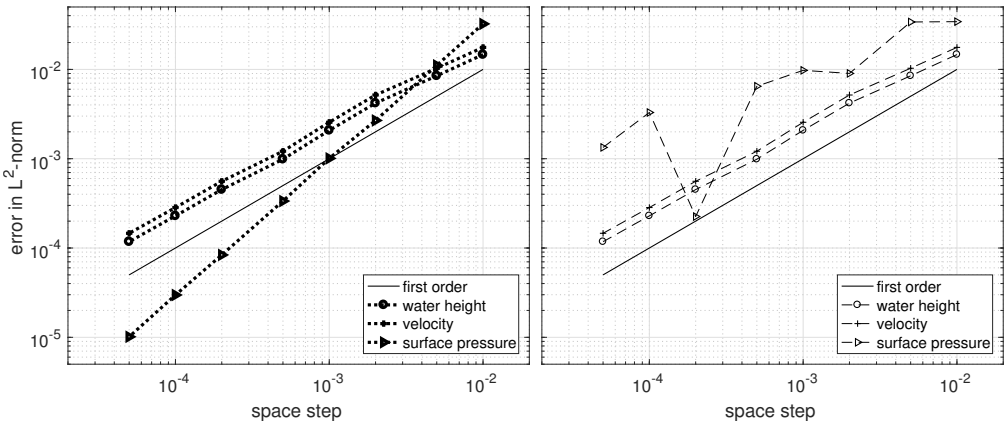

a) L^2-errors with $\lambda^2 = \delta_x$ b) L^2-errors with $\lambda = 0$

Figure 2.5 – Transcritical steady flow with free hydraulic jump: L^2-convergence rate for the water height, the velocity and the surface pressure compared to first order.

Let us consider a bottom and a roof respectively defined by

$$B(x) = 3.5 \exp\left(-100\,(x-0.35)^2\right) \qquad \text{and} \qquad R(x) = 100\,(x-0.5)^2 + 5.8.$$

The water depth at the exit is fixed to $h(l,t) = 8$ and the discharge at the entry is set to $h\overline{u}(0,t) = 25$. The physical parameters are chosen such that the flow is subcritical (fluvial) at the boundaries but becomes supercritical (torrential) because of the nonflat bottom and the hydraulic jump reaches the roof.

The simulated solution with $\delta_x = 10^{-3}$ and $\lambda^2 = \delta_x$ as well as $\lambda = 0$ is plotted in Figure 2.6. Furthermore a reference solution is plotted for comparison. More precisely the analytical solution of the water height without considering the roof and the corresponding velocity are plotted, see (A.0.2) as well as the analytical value of the surface pressure considering the roof, see (A.0.3). As expected, the water depth and the velocity are similar in the areas where the flow does not reach the roof and only the localization of the hydraulic jump is not recovered. At the hydraulic jump, the water depth as well as the surface pressure are discontinuous which makes the product $h\nabla_x p_\eta$ really non-conservative and the position of the shock not easy to compute. The peak of the pressure at the top of the hydraulic jump is due to oscillation effects of the CPR scheme at discontinuities, see [90]. By increasing the CPR-parameter γ in order to regularize the solution and decrease the oscillation effects, the approximation of the water height gets worse. However, the hydraulic jump is clearly not located at the same position

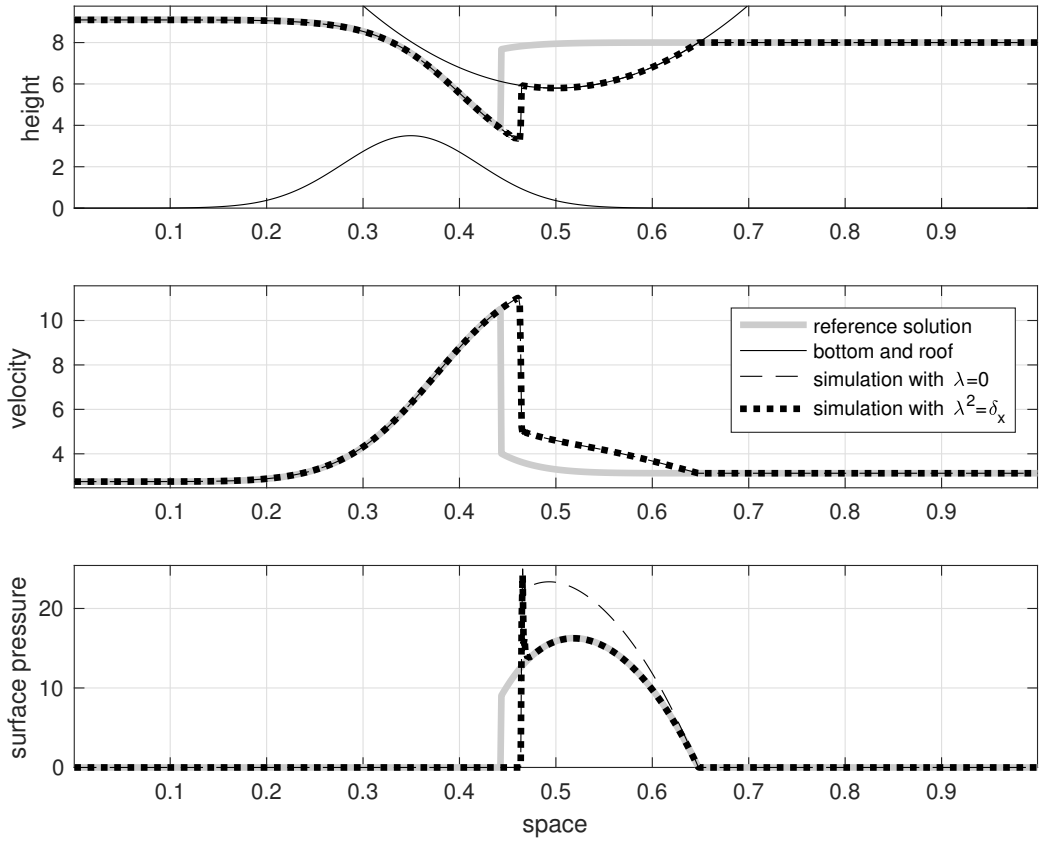

Figure 2.6 – Transcritical steady flow with constrained hydraulic jump.

with and without the roof. We conclude that the surface pressure has an impact on the jump condition, at least at the discrete level.

2.3.2.4 Time-dependent emptying tank

Assuming a fixed and flat bottom, an analytical solution of the congested shallow water model can be obtained for any fixed bottom as long as the interface between the congested and the free surface flow is fixed. More precisely, we claim the following statement.

Proposition 2.3.5. *Let us consider a fixed flat bottom and an uniform atmospheric pressure, i.e.* $B = \partial_x P = 0$. *Furthermore, let us consider a fixed constant roof in a part of the domain delimited by two fixed points* $x_l \leq 0 \leq x_r$, *i.e.*

$$R(x) = \begin{cases} \overline{H}_0, & \text{if } x_l \leq x \leq x_r \\ \infty, & elsewhere \end{cases}$$

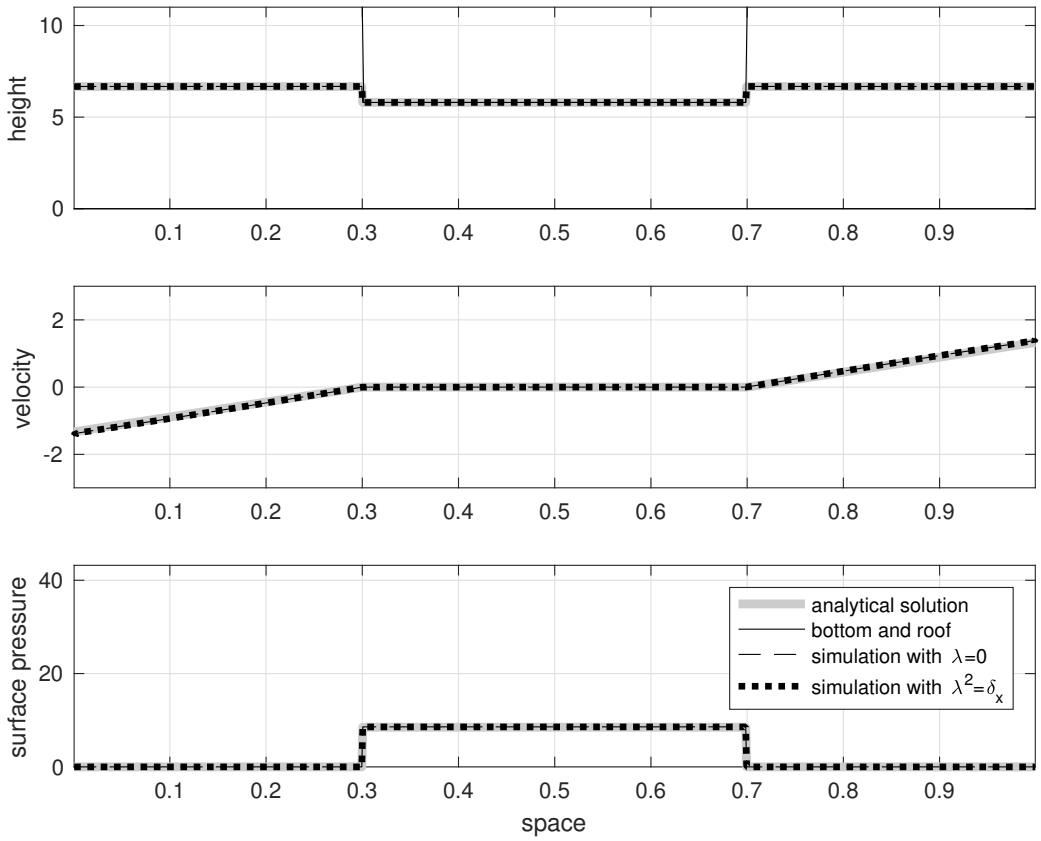

Figure 2.7 – Emptying tank at time t=0.5

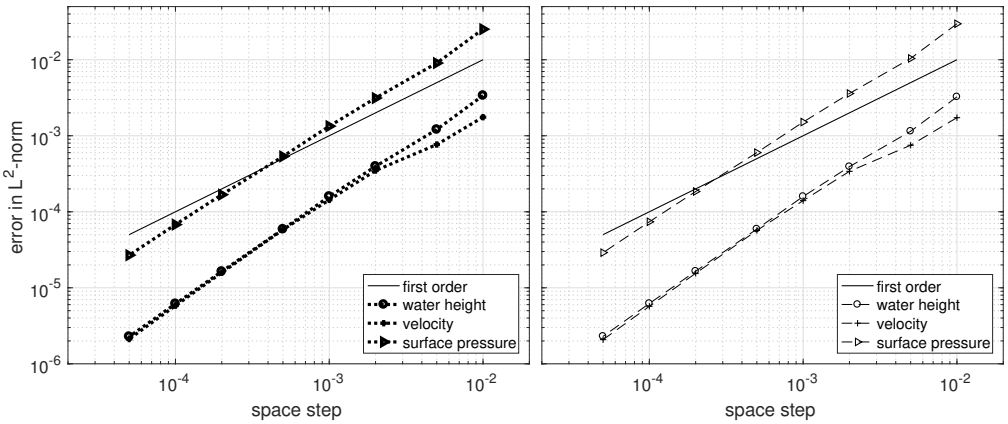

a) L^2-errors with $\lambda^2 = \delta_x$ b) L^2-errors with $\lambda = 0$

Figure 2.8 – Emptying tank: L^2-convergence rate for the water height, the velocity and the surface pressure compared to first order.

with an arbitrary opening $\overline{H}_0 > 0$.
Then for any $\alpha \geq 0$, $h^0 > \overline{H}_0$ *and any time* $t \leq \frac{h^0 - \overline{H}_0}{\alpha \overline{H}_0}$, *the following functions*

$$h(x,t) = \begin{cases} \overline{H}_0, & \text{if } x_l \leq x \leq x_r \\ \dfrac{h^0}{1+\alpha t}, & \text{elsewhere} \end{cases}$$

$$\overline{u}(x,t) = \begin{cases} \dfrac{\alpha (x - x_l)}{1+\alpha t}, & \text{if } x < x_l \\ 0, & \text{if } x_l \leq x \leq x_r \\ \dfrac{\alpha (x - x_r)}{1+\alpha t}, & \text{if } x_r < x \end{cases}$$

$$p_\eta(x,t) = P_\eta(t) + g\left(\frac{h^0}{1+\alpha t} - \overline{H}_0\right)$$

are solution of the congested shallow water model (2.2.8)-(2.2.10) *without friction, i.e.* $\overline{\mu} = 0$.

Proof. The proof relies on simple computations after injecting the functions in the congested shallow water equations (2.2.8)-(2.2.10). The non-conservative product is well-defined since the pressure at the bottom $gh + p_\eta$ is continuous. □

Figure 2.7 shows the analytical solution of the Proposition 2.3.5 at time $t = 0.5$ with the parameters $h^0 = 10$, $\alpha = 1$, $\overline{H}_0 = 5.8$, $x_l = 0.3$ and $x_r = 0.7$, together with the numerical solution with $\delta_x = 10^{-3}$ and $\lambda^2 = \delta_x$ as well as $\lambda = 0$. The numerical solution is in very good agreement with the analytical solution. Figure 2.8 shows the convergence rates in L^2-norm to the analytical solution for the water depth, the velocity and the surface pressure for $\lambda = 0$ and $\lambda^2 = \delta_x$. The three unknowns converge approximately at order 1.36 for any λ, which is better than the expected first order. In this case the pressure depends linearly on the water depth, which explains the same order of convergence for the pressure for both values of λ compared to the stationary case.

2.3.2.5 Time-dependent filling tank

The current simulation is a numerical investigation of the jump condition when the top of the hydraulic jump reaches the roof. More precisely, a fixed flat bottom and roof and a symmetrical initial condition given by

$$h^0(x) = \frac{1}{2}\overline{H}(x,0) \qquad \text{and} \qquad \overline{u}^0(x) = \begin{cases} C, & \text{if } x < \frac{1}{2} \\ -C, & \text{if } x > \frac{1}{2} \end{cases}$$

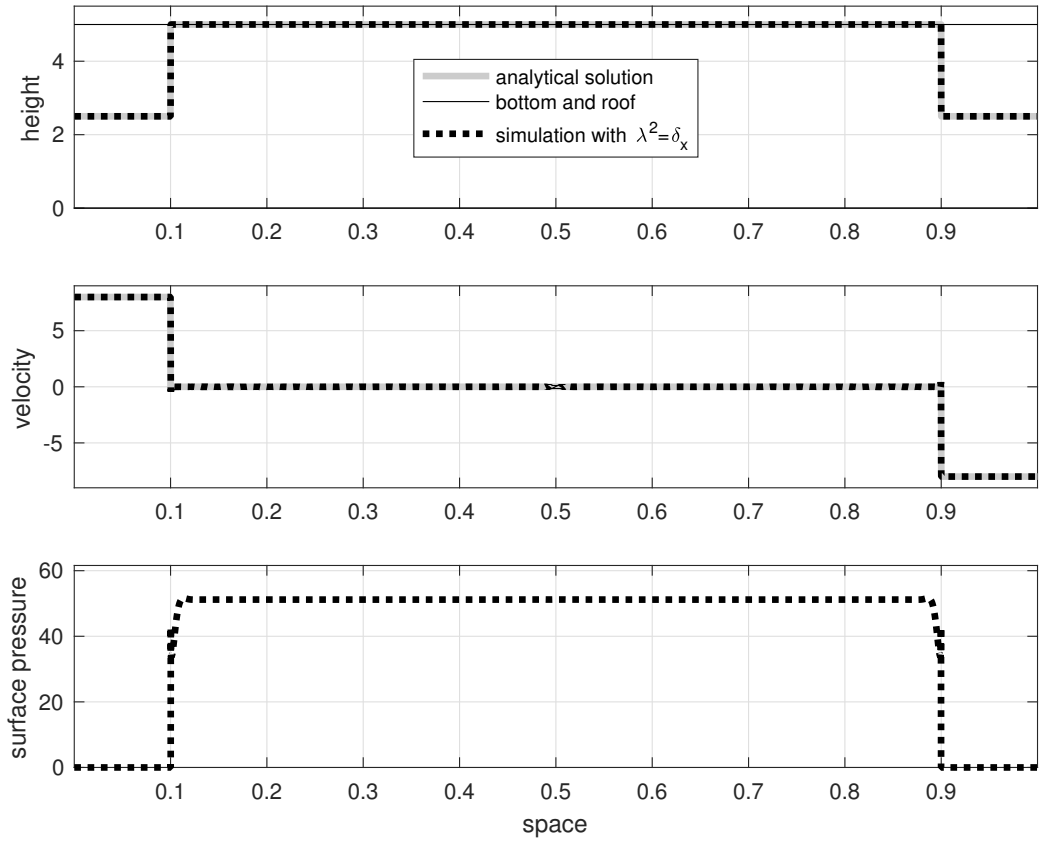

Figure 2.9 – Filling tank at time t=0.05.

with $\overline{H}(x,0) = 5$ for all $x \in [0,l]$ and $C = 8$ are considered. The initial condition is chosen such that the flow is supercritical (torrential).

Figure 2.9 shows the numerical result at time $t = 0.05$ with $\delta_x = 10^{-4}$, $\lambda^2 = \delta_x$ and $\gamma = 10$. Due to the shock waves, the CPR-parameter γ is increased to get slightly more regularisation, see [90]. Otherwise oscillations of the pressure in the vicinity of the shock due to oscillation effects of the CPR scheme are observed. However, the oscillations increase when λ becomes smaller and more regularization is needed. As a consequence, we cannot pass $\lambda = 0$ in the simulation, as either the oscillations become too large or the regularization effect is too high. As expected, the solution is composed by tree constant states separated by two shock waves. By symmetry, it is clear that the velocity in the middle state should vanish. In addition, the conservation of the mass imposes the velocity of the shock wave. More precisely, it leads to $X' = 2U$ with $X(t)$ the position of the shock. However, the computation of the pressure of the middle state is inaccessible since the water depth and the surface pressure are discontinuous at the shock.

2.4 Conclusion

A shallow water type model with a constraint of congestion is derived from the Navier-Stokes equations for the modeling of a roof in geophysical applications. The simulation of the congested shallow water model is challenging due to the unknown localization of the interface between the congested areas and the free surface domain. To overcome this difficulty, an approximate model which is hyperbolic in the free surface domain as well as in the congested areas is proposed based on a pseudo-compressible approximation. We show that two properties, mainly well-balanced and low-Froude stability, are needed at the discrete level for the simulation of the approximate model. Eventually, a numerical scheme adapted from the Centered-Potential Regularization scheme is proposed and confronted with analytical solutions to illustrate the efficiency of the scheme.

Concerning the theoretical analysis, several issues have not yet been addressed. Firstly, to confirm the relevance of the pseudo-compressible approximation, the convergence of the approximate model (2.2.16) and (2.2.18) as λ goes to zero to the initial congested shallow water model (2.2.8)-(2.2.10) seems a natural question but not at hand for the moment. The second open problem in the analysis of the congested shallow water model (2.2.8)-(2.2.10) is the definition of the non-conservative product $h\nabla_x p_\eta$. More precisely the water height, as well as the surface pressure can be discontinuous in the same point as shown in Figure 2.6. Since the surface pressure plays the role of a Lagrange multiplier, the model (2.2.8)-(2.2.10) is not a hyperbolic conservation law. As a consequence a classical analysis of non-conservative products in hyperbolic theory, for example [37], cannot be directly applied here.

To improve the modeling, several ways can be investigated. First of all, the modeling of areas with negative relative pressure, i.e. $p_\eta < P_\eta$ is quite challenging. This issue seems more generally linked to the modeling of trapped air pockets under the roof. Secondly, the congestion constraint can be applied to more complex models of free surface flow such as the layerwise discretized models [3; 5], the non-hydrostatic models [27; 74] or the combination of the two [48]. Moreover, the bilateral interaction between the roof and the fluid seems interesting for applications, in particular for object buoyancy such as boats or buoys. Last but not least, the modeling of an immersed object, using layerwise discretized models, is still quite far but can be a challenging objective.

The appendix A about the transcritical analytical solution was attached to the published article.

Chapter 3

Congested shallow water model: floating buoy

This chapter has been done in collaboration with Edwige Godlewski, Martin Parisot and Jacques Sainte-Marie.

It will be submitted (a preprint version already exists [54]).

3.1 Introduction

We are interested in the modeling of a floating body. In a previous work [55] we considered a congested shallow water model. A roof denoting an impermeable surface above the water flow which constrains the water surface was introduced. In [55], the motion of the roof was prescribed, whereas in the present work, it is no longer the case, leading to the coupling of the equations modeling the fluid and the structure motion. Applications are floating icebergs, floating fragments during inondations or the production of sustainable energy using buoys.

Two main approaches are proposed in the literature to treat fluid-solid interaction.

The first dates back to Fritz John who proposed a mathematical formulation of the problem [65]. The fluid is described by a velocity potential with a linear model for the free surface evolution. The motion of the solid is supposed to be of small amplitude so that the interface between the water and the solid is constant in time. Finally the surface pressure is obtained using the linearized Bernoulli equation. Although the model is quite simplified, linear potential flow theory is still used in industrial context since it is not costly

in CPU time, see [82]. However nonlinear terms play an important part for wave interaction. For instance the nonlinearity should be taken into account in simulations of wave energy converter farms. Improvements have been made to include nonlinear effects based on the boundary element methods [60] and an interface depending on time [66]. This progress needs higher CPU times and does not yet allow wave breaking.

The second are Navier-Stokes CFD computations. This approach is considerably used in blood flow, for instance in aortic flow [31; 97].

Some other works also use Navier-Stokes CFD computations for the simulation of the flow around a yacht [91] or wave energy converters [1; 89; 107]. This approach couples the fluid usually expressed in a Eulerian frame and the solid usually expressed in a Lagrangian frame. The difficulty comes from the mesh. A moving grid with front tracking methods or a fixed mesh with fictitious fluid domain can be considered. The first one perfectly catches the interface but needs a moving mesh while the second is less accurate on the position of the interface but the mesh is fixed. However this strategy implies high CPU times and does not make these methods suitable for engineering optimization.

To take advantage of the benefits from each approach, a coupling has been proposed [105]. Since the viscosity is not considered in potential flow theory, it can hardly been included in the coupling.

Recently the nonlinear floating body problem was reformulated in the framework of vertical-integrated models [73]. A vertical movement of the body is considered so that the interface between the congested and the free surface domain is fixed in time and continuity of the unknowns is assumed at the interface. The surface pressure is then obtained by an elliptic equation.
An analysis of this shallow water type model in the two dimensional case with radial symmetry is done in [17]. In a more general framework the well-posedness of the model in the one dimensional case has been proven in [63], relaxing the assumption of vertical lateral walls. The description of the interface position is dealt with.
A numerical resolution in one dimension of the model proposed in [73] is done in [18]. Each domain can be solved by the most appropriate numerical strategy but transmission conditions have to be written at the interface. Since discontinuous solutions can appear in hyperbolic models, the latter conditions can be tricky to handle.

In [55] we have proposed a uniform numerical resolution which eliminates the description of the interface and the transition conditions between the congested and the free surface domain. The surface pressure is seen as a Lagrange multiplier associated to a constraint.

These models [55; 73] are based on depth-averaging and thus they cannot

modelize wave breaking but nonlinear terms are accounted for. Simpler than the Navier-Stokes equations but still physically relevant, their resolution is less CPU consuming since the computational domain does not depend on time. For optimization processes this seems interesting, especially when large domains are considered.

In the present work, we give a formulation of the floating body problem taking into account a freely floating object, i.e. translating and rotating. A choice of discretization for the different operators is proposed in order to assure a strong coupling between the two systems. We use a Newmark scheme for the solid and adapt the numerical strategy given in [55] for a 'fixed roof' to the coupling. Furthermore our method allows to write the energy of the coupled fluid-solid system. The energy transfer between the fluid and the solid is indeed a challenging problem and of major interest in energy production using buoys. From a mathematical point of view, the energy balance, acting as an entropy, is an argument for the existence of long time solutions.

In Section 3.2 the formulation at the continuous level is given. In Section 3.3 we explain the numerical strategy. A first naive non-entropy satisfying approach is considered followed by an entropy correction. Finally in Section 3.4 we show simulations in a one dimensional framework to validate our approach.

3.2 Mathematical modeling

Let us start by recalling the shallow water model for constrained flow.

3.2.1 Fluid dynamics

In [55] a shallow water type model with an additional congestion constraint modeling a 'roof' is proposed. Let us briefly introduce this model which is derived from the Navier-Stokes equations.
A flow contained between two surfaces respectively called roof and bottom is considered. The two surfaces can be parametrized by two given mono-valued smooth enough functions $R(x,t)$ and $B(x,t)$ (see Figure 3.1) which satisfy $B(x,t) \leq R(x,t)$. The opening $\overline{H}$ between the roof and the bottom is defined by

$$\overline{H}(x,t) = R(x,t) - B(x,t).$$

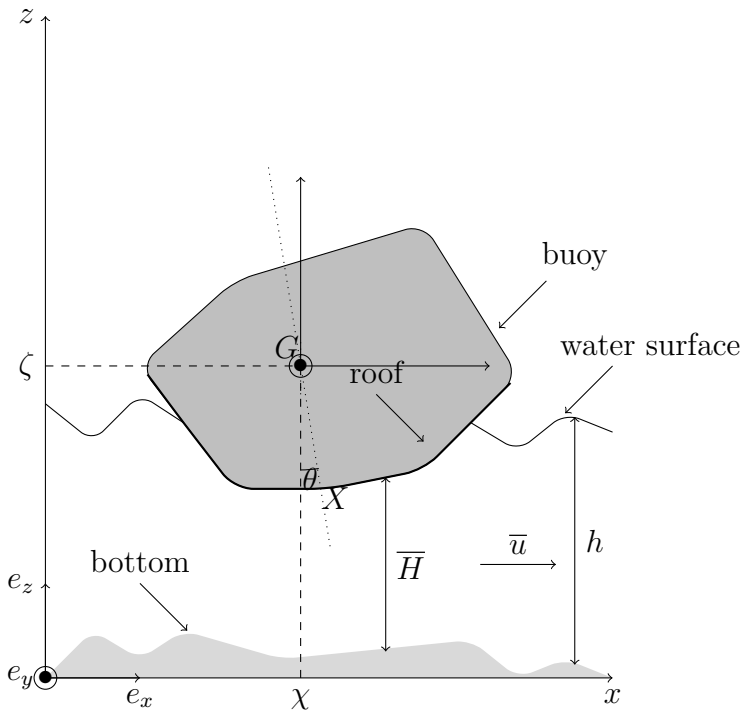

Figure 3.1 – Buoy configuration

We consider a one dimensional given domain $\Omega_x \subset \mathbb{R}$. In practice the domain Ω_x will be bounded but for simplicity the boundary conditions will not be detailled. The unknowns of the model are the water depth h, the vertical-averaged horizontal velocity $\overline{u}$ and the surface pressure p_η which satisfy

$$\begin{cases} \partial_t h & + \partial_x \left(h\overline{u}\right) & = 0 \\ \partial_t \left(h\overline{u}\right) & + \partial_x \left(h\overline{u}^2 + \dfrac{g}{2}h^2\right) & = -h\partial_x \left(gB + p_\eta\right) \end{cases} \tag{3.2.1}$$

with g the gravitational constant.
In addition, the constraint

$$\min\left(\overline{H} - h, p_\eta - P\right) = 0 \tag{3.2.2}$$

has to be satisfied where $P\left(x,t\right)$ denotes the given atmospheric pressure.
In the following, the atmospheric pressure is taken constant in time and space and for simplicity equal to zero, i.e. $P = 0$.
Finally the system (3.2.1)-(3.2.2) is completed with the initial conditions $h\left(x,0\right) = h^0(x)$ and $\overline{u}\left(x,0\right) = \overline{u}^0\left(x\right)$.
An energy balance law can be written.

Lemma 3.2.1. *Any smooth enough solution of the congested shallow water model (3.2.1)-(3.2.2) satisfies the following energy balance law*

$$\partial_t \mathcal{E} + \partial_x \mathcal{G} = -p_\eta \partial_t R + (gh + p_\eta)\, \partial_t B$$

with the mechanical energy

$$\mathcal{E} = \frac{1}{2} h \overline{u}^2 + gh \left(B + \frac{h}{2} \right)$$

and the energy flux

$$\mathcal{G} = \left(\frac{1}{2} \overline{u}^2 + g\,(h + B) + p_\eta \right) h \overline{u}.$$

Proof. The proof is done in [55, Proposition 1.3]. □

In the present work, if $B\,(x,t)$ is still a given function, this is no longer the case for $R\,(x,t)$. The interaction between the fluid and the roof is considered, i.e. $R\,(x,t)$ is now an unknown of the problem and its evolution has to be determined.

Note that the modeling of submerged objects is not allowed by the choice of modeling for the fluid since the vertical averaged model considers only one water height. Thus in the following, we will restrict ourselves to a certain type of configuration for the floating objects. For more mathematical details see Hypothesis 3.2.2.

3.2.2 Solid dynamics

Let us describe the planar motion of a floating object. The reader can refer to [69] for more details about solid dynamics. The scalar product between two vectors v_1 and v_2 is denoted $v_1 \cdot v_2$ and the cross product $v_1 \times v_2$.
We consider a homogeneous solid body $\mathcal{B}$ of mass M floating on top of the water surface, called buoy in the following. A general planar movement supposes three degrees of freedom, denoted χ, ζ and θ, see Figure 3.1. The buoy is supposed not to touch the bottom. The interior unit normal to the buoy surface is denoted by n and its center of mass $G = (\chi, \zeta)$, where $\chi \in \Omega_x$ denotes the horizontal and $\zeta \in \mathbb{R}$ the vertical component. The variable θ stands for the angle between the unit vector in the vertical direction e_z and the vector GX where X is a point in the solid different from the center of mass. The moment of inertia of the solid around an axis passing through the center of mass is denoted $\mathcal{J}_G$.

A general planar motion of a rigid body can be separated into a translational motion of a point in the body and a rotational motion around an axis through that point. In most cases it is convenient to choose this point as the center of mass G. In the part of the domain where there is no buoy, the roof is defined high enough not to touch the fluid surface and otherwise the roof is given by

$$R(x,t) = \mathcal{R}(x, \chi(t), \zeta(t), \theta(t)) \tag{3.2.3}$$

where

$$\mathcal{R}(x,\chi,\zeta,\theta) = R_0(x-\chi,\theta) + \zeta \tag{3.2.4}$$

with $R_0(x,\theta)$ a given function characterizing the geometry of the inferior surface of the floating object at position $x \in \Omega_x$ and for any angle $\theta \in [-\pi,\pi]$. For example in the case of a discal buoy with radius r, an expression can be given for R_0. Since the geometry is independent of the rotation, it writes

$$R_0^{disc}(x,\theta) = \begin{cases} -\sqrt{r^2-x^2}, & \text{if } -r \le x \le r \\ +\infty, & \text{elsewhere.} \end{cases}$$

For an elliptical buoy with semi-minor and semi-major axis respectively equal to a and b,

$$R_0^{ell}(x,\theta) = \begin{cases} \min\{z \mid \mathcal{P}_{x,\theta}(z) = 0\}, & \text{if } \min\limits_{t\in[0,2\pi[} f_\theta(t) \le x \le \max\limits_{t\in[0,2\pi[} f_\theta(t) \\ +\infty, & \text{elsewhere} \end{cases}$$

with the second order polynomial

$$\mathcal{P}_{x,\theta}(z) = \frac{(x\cos\theta + z\sin\theta)^2}{a^2} + \frac{(x\sin\theta - z\cos\theta)^2}{b^2} - 1$$

and $f_\theta(t) = a\cos(\theta)\cos(t) + b\sin(\theta)\sin(t)$. Since the function R_0 is not always explicit, we will explain in Section 3.3.4 the numerical handling.

The horizontal (resp. vertical) forces other than the weight and the pressure from the fluid will be denoted by F_χ (resp. F_ζ). Their torque around the center of mass is denoted by T_θ. These forces could for example represent a mooring line and do not play a direct role in the interaction between the fluid and the solid.

Proposition 3.2.1. *A general planar movement of the solid body $\mathcal{B}$ is described by the system*

$$\begin{cases} M\ddot{\chi} = -\displaystyle\int_{\Omega_x} p_\eta \partial_x \mathcal{R} \mathrm{d}x + F_\chi \\ M\ddot{\zeta} = -Mg + \displaystyle\int_{\Omega_x} p_\eta \mathrm{d}x + F_\zeta \\ \mathcal{J}_G\ddot{\theta} = \displaystyle\int_{\Omega_x} p_\eta \partial_\theta \mathcal{R} \mathrm{d}x + T_\theta \end{cases} \tag{3.2.5}$$

completed with the initial conditions $\chi(0) = \chi^0$, $\dot{\chi}(0) = \dot{\chi}^0$, $\zeta(0) = \zeta^0$, $\dot{\zeta}(0) = \dot{\zeta}^0$, $\theta(0) = \theta^0$ *and* $\dot{\theta}(0) = \dot{\theta}^0$.

Proof. The translational motion can be described by Newton's second law of motion. Taking into account the forces F_χ, F_ζ, the weight together with the pressure applied on the buoy from the water gives the following equations

$$\begin{cases} M\ddot{\chi} = \displaystyle\int_{\Omega_x} p_\eta n \cdot e_x \sqrt{1 + (\partial_x \mathcal{R})^2}\mathrm{d}x + F_\chi \\ M\ddot{\zeta} = -Mg + \displaystyle\int_{\Omega_x} p_\eta n \cdot e_z \sqrt{1 + (\partial_x \mathcal{R})^2}\mathrm{d}x + F_\zeta. \end{cases} \tag{3.2.6}$$

The rotational movement is described by the angular momentum theorem, i.e.

$$\partial_t \mathcal{L}_G = \int_{\Omega_x} p_\eta \left(GX \times n\right) \cdot e_y \sqrt{1 + (\partial_x \mathcal{R})^2}\mathrm{d}x + T_\theta \tag{3.2.7}$$

where $\mathcal{L}_G$ denotes the angular momentum around G, X a point at the surface with coordinates $(X_x, \mathcal{R}(X_x, \chi, \zeta, \theta))$ and $e_y = e_x \times e_z$ the unit vector in the direction perpendicular to the plane.

By definition, in a planar framework $\partial_t \mathcal{L}_G = \mathcal{J}_G \ddot{\theta}$.

Replacing the interior normal $n = \dfrac{1}{\sqrt{1 + (\partial_x \mathcal{R})^2}} \begin{pmatrix} -\partial_x \mathcal{R} \\ 1 \end{pmatrix}$ in (3.2.6) leads to the first two equations of (3.2.5) and for (3.2.7) it yields

$$\mathcal{J}_G \ddot{\theta} = -\int_{\Omega_x} p_\eta \left(GX \cdot e_z \partial_x \mathcal{R} + GX \cdot e_x\right) \mathrm{d}x + T_\theta. \tag{3.2.8}$$

Let us denote by $\widetilde{\ }$ the coordinates in the reference frame of the center of mass. In this frame, the movement is a simple rotation of angle θ and as a consequence the coordinates $\left(\widetilde{X}_x, \widetilde{\mathcal{R}}\left(\widetilde{X}_x, \theta\right)\right)$ of the point X verify

$$\begin{pmatrix} \widetilde{X}_x \\ \widetilde{\mathcal{R}} \end{pmatrix} = M_{\theta - \theta^0} \begin{pmatrix} \widetilde{X}_x^0 \\ \widetilde{\mathcal{R}}\left(\widetilde{X}_x^0, \theta^0\right) \end{pmatrix}$$

with $\left(\widetilde{X}_x^0, \widetilde{\mathcal{R}}\left(\widetilde{X}_x^0, \theta^0\right)\right)$ the coordinates of the point X with an angle θ^0 and

$$M_{\theta - \theta^0} = \begin{pmatrix} \cos(\theta - \theta^0) & \sin(\theta - \theta^0) \\ -\sin(\theta - \theta^0) & \cos(\theta - \theta^0) \end{pmatrix}. \tag{3.2.9}$$

The previous relation implies

$$\widetilde{\mathcal{R}} = \partial_\theta \widetilde{X}_x. \tag{3.2.10}$$

Moreover the trajectory of the points of the buoy are concentric circles, i.e. $\partial_\theta \|GX\| = 0$. Thus

$$\partial_\theta \left(\left(\widetilde{X}_x \right)^2 + \left(\widetilde{\mathcal{R}} \left(\widetilde{X}_x, \theta \right) \right)^2 \right) = 0$$

and it follows

$$\widetilde{X}_x \partial_\theta \widetilde{X}_x + \widetilde{\mathcal{R}} \partial_\theta \widetilde{X}_x \partial_x \widetilde{\mathcal{R}} + \widetilde{\mathcal{R}} \partial_\theta \widetilde{\mathcal{R}} = 0.$$

Using now the relation (3.2.10), we get

$$\widetilde{X}_x + \widetilde{\mathcal{R}} \partial_x \widetilde{\mathcal{R}} + \partial_\theta \widetilde{\mathcal{R}} = 0. \tag{3.2.11}$$

Finally introducing this relation in (3.2.8) and noticing that $GX \cdot e_z = \widetilde{\mathcal{R}}$ and $GX \cdot e_x = \widetilde{X}_x$ gives the last equation in (3.2.5). □

The solid system admits the following energy balance law.

Lemma 3.2.2. *Any smooth solution of (3.2.5) satisfies the following energy law*

$$\partial_t E = \left(\int_{\Omega_x} p_\eta \mathrm{d}x + F_\zeta \right) \dot{\zeta} - \left(\int_{\Omega_x} p_\eta \partial_x \mathcal{R} \, \mathrm{d}x - F_\chi \right) \dot{\chi} + \left(\int_{\Omega_x} p_\eta \partial_\theta \mathcal{R} \mathrm{d}x + T_\theta \right) \dot{\theta}$$

with $E(\chi, \zeta, \theta) = \dfrac{M}{2} \left(\dot{\zeta}^2 + \dot{\chi}^2 \right) + \dfrac{\mathcal{J}_G}{2} \dot{\theta}^2 + Mg\zeta.$

Proof. Multiplying the first equation of (3.2.5) by $\dot{\chi}$, the second equation by $\dot{\zeta}$, the third equation by $\dot{\theta}$ and summing gives the result. □

An energy law for the coupled fluid-solid system (3.2.5) and (3.2.1)-(3.2.2) is obtained.

Proposition 3.2.2. *Considering a no-flux boundary on Ω_x, any smooth solution of (3.2.5) and (3.2.1)-(3.2.2) satisfies the following energy balance law*

$$\partial_t \left(\int_{\Omega_x} \mathcal{E} \, \mathrm{d}x + E \right) = \int_{\Omega_x} (gh + p_\eta) \, \partial_t B \mathrm{d}x + F_\zeta \dot{\zeta} + F_\chi \dot{\chi} + T_\theta \dot{\theta}.$$

Proof. It follows from (3.2.3)-(3.2.4) that

$$\begin{aligned} \partial_t R(x,t) &= \dot{\chi} \partial_\chi \mathcal{R}(x, \chi, \zeta, \theta) + \dot{\zeta} \partial_\zeta \mathcal{R}(x, \chi, \zeta, \theta) + \dot{\theta} \partial_\theta \mathcal{R}(x, \chi, \zeta, \theta) \\ &= -\dot{\chi} \partial_x \mathcal{R}(x, \chi, \zeta, \theta) + \dot{\zeta} + \dot{\theta} \partial_\theta \mathcal{R}(x, \chi, \zeta, \theta). \end{aligned} \tag{3.2.12}$$

Now integrating the energy balance law from Lemma 3.2.1 over Ω_x and summing with the result from Lemma 3.2.2 concludes the proof. □

Since R_0 goes to infinity in the part of the domain where there is no buoy, the derivatives $\partial_x \mathcal{R}$ and $\partial_\theta \mathcal{R}$ are singular. However, the derivatives are multiplied by the surface pressure p_η, see (3.2.5) and the surface pressure p_η vanishes in the points where the buoy is not in contact with the water. Thus these singularities do not impact the model assuming the following hypothesis.

Hypothesis 3.2.1. *The water does not reach the buoy at the singular points, in particular at the extremities.*

3.3 Numerical resolution

This section is devoted to the numerical resolution of (3.2.1)-(3.2.2) and (3.2.5). We first describe separately the numerical methods chosen for each model before considering their coupling.

3.3.1 Discretization for the fluid dynamics

Let us firstly remind some properties of the numerical strategy proposed in [55] for the congested shallow water model (3.2.1)-(3.2.2).
Let $\mathbb{T}$ be a mesh of Ω_x composed of control volumes. We denote $k \in \mathbb{T}$ a control volume, x_k the coordinate of its center and by the subscript $k-\frac{1}{2}$ (resp. $k+\frac{1}{2}$) its left (resp. right) face. The space step is defined by $|k|$. In addition the time step is denoted by δ_t^{n+1}, i.e. $t^{n+1} = t^n + \delta_t^{n+1}$.
The mean bottom level in the control volume k, at time t^n, is denoted by B_k^n.

A pseudo-compressibility method is used to take into account the congestion constraint. Let us denote by λ the relaxation parameter.
Following [55], one particularity of the proposed scheme is that the numerical unknowns are ϕ_k^n and $\overline{u}_k^n$ which are the average of the potential defined by $\phi = g\,(h+B) + p_\eta$ and the velocity $\overline{u}$ in the volume k at time t^n. The potential can be used as a parametrization of the water depth and the surface pressure, thus we set

$$h\,(k,n;\phi) = \begin{cases} \dfrac{\phi}{g} - B_k^n, & \text{if } \phi \leq g R_k^n \\ \dfrac{R_k^n - B_k^n + \lambda^2 \left(\frac{\phi}{g} - B_k^n\right)}{1+\lambda^2}, & \text{else} \end{cases}$$

and

$$p\,(k,n;\phi) = \phi - g\,(h\,(k,n;\phi) + B_k^n)$$

where R_k^n is an approximation of the mean value of the roof level in the control volume k at time t^n. For readability, we set $h_k^n = h\left(k, n; \phi_k^n\right)$ and $p_k^n = p\left(k, n; \phi_k^n\right)$.
We also introduce the following notation

$$\partial_t^{n+1}\psi = \frac{\psi^{n+1} - \psi^n}{\delta_t^{n+1}}.$$

The scheme finally reads

$$h_k^{n+1} = h_k^n - \frac{\delta_t^{n+1}}{|k|}\left(\mathcal{F}_{k+\frac{1}{2}}^{n+1} - \mathcal{F}_{k-\frac{1}{2}}^{n+1}\right) \tag{3.3.1}$$

and

$$\begin{aligned} h_k^{n+1}\overline{u}_k^{n+1} &= h_k^n\overline{u}_k^n - \delta_t^{n+1}h_k^{n+1}\frac{\phi_{k+1}^{n+1} - \phi_{k-1}^{n+1}}{2|k|} \\ &- \frac{\delta_t^{n+1}}{|k|}\left(\overline{u}_k^n\left(\mathcal{F}_{k+\frac{1}{2}}^{n+1}\right)_+ - \overline{u}_{k+1}^n\left(\mathcal{F}_{k+\frac{1}{2}}^{n+1}\right)_- + \overline{u}_k^n\left(\mathcal{F}_{k-\frac{1}{2}}^{n+1}\right)_- - \overline{u}_{k-1}^n\left(\mathcal{F}_{k-\frac{1}{2}}^{n+1}\right)_+\right) \end{aligned} \tag{3.3.2}$$

with $\mathcal{F}_{k+\frac{1}{2}}^{n+1}$ an approximation of the mean mass flux $h\overline{u}$ at the face $k+\frac{1}{2}$ between the times t^n and t^{n+1}. More precisely

$$\mathcal{F}_{k+\frac{1}{2}}^{n+1} = \frac{h_k^{n+1}\overline{u}_k^n + h_{k+1}^{n+1}\overline{u}_{k+1}^n}{2} - \frac{\gamma\delta_t^{n+1}}{2}\left(\frac{h_k^{n+1}}{|k|} + \frac{h_{k+1}^{n+1}}{|k+1|}\right)\frac{\left(\phi_{k+1}^{n+1} - \phi_k^{n+1}\right)}{2} \tag{3.3.3}$$

with a regularization parameter $\gamma \geq 0$ characteristic of the scheme, see [90].
The numerical scheme requires boundary conditions which depend on the regime of the flow. In the current work, we do not detail the boundary conditions treatment, see [76, section 21.8] for more details.
The following energy dissipation law has been proven in [55, Proposition 2.3].

Lemma 3.3.1. *For any $\gamma \geq 1$ and under the CFL condition*

$$\begin{aligned} &\left(\left|\frac{\overline{u}_k^n + \overline{u}_{k+1}^n}{2}\right| + \sqrt{\frac{\gamma}{2}}\sqrt{\left|\frac{\phi_{k+1}^{n+1} - \phi_k^{n+1}}{2}\right|}\right)\delta_t^{n+1} \\ &\qquad \leq \frac{\min\left(h_k^{n+1}, h_{k+1}^{n+1}\right)}{2\left(h_k^{n+1} + h_{k+1}^{n+1}\right)}\min\left(|k|, |k+1|\right) \end{aligned} \tag{3.3.4}$$

there exists a discrete flux $\mathcal{G}_{k+\frac{1}{2}}^{n+1}$ such that the scheme (3.3.1)-(3.3.3) admits the following energy dissipation law

$$\partial_t^{n+1}\mathcal{E}_k + \frac{1}{|k|}\left(\mathcal{G}_{k+\frac{1}{2}}^{n+1} - \mathcal{G}_{k-\frac{1}{2}}^{n+1}\right) \leq -p_k^{n+1}\partial_t^{n+1}R_k + \left(gh_k^n + p_k^{n+1}\right)\partial_t^{n+1}B_k \tag{3.3.5}$$

with the discrete mechanical energy

$$\mathcal{E}_k^n = \frac{1}{2} h_k^n \left(\overline{u}_k^n\right)^2 + g h_k^n \left(B_k^n + \frac{h_k^n}{2}\right) + \frac{g}{2\lambda^2} \left(h_k^n - R_k^n + B_k^n\right)_+^2$$

and $\mathcal{G}_{k+\frac{1}{2}}^{n+1}$ *defined in [55].*

Note that in the present work, R_k^n depends on the values χ^n, ζ^n and θ^n via (3.2.4). In the next section, the numerical resolution for the latter and its coupling with the fluid scheme will be detailed.

3.3.2 Discretization for the solid dynamics

The three degrees of freedom of the solid at time t^n are respectively denoted by θ^n, χ^n and ζ^n.

Due to its simple implementation, a Newmark scheme is chosen to solve the buoy dynamics (3.2.5). In fact each time step only requires the resolution of one set of equations. For $(\alpha, \beta) \in [0,1]^2$, the Newmark scheme for an ODE of the form $\ddot{\Lambda} = \mathcal{H}\left(\Lambda, \dot{\Lambda}, t\right)$ writes

$$\begin{cases} \Lambda^{n+1} = \Lambda^n + \delta_t^{n+1} \dot{\Lambda}^n + \dfrac{\left(\delta_t^{n+1}\right)^2}{2} \left(\beta \ddot{\Lambda}^{n+1} + (1-\beta)\, \ddot{\Lambda}^n\right) \\ \dot{\Lambda}^{n+1} = \dot{\Lambda}^n + \delta_t^{n+1} \left(\alpha \ddot{\Lambda}^{n+1} + (1-\alpha)\, \ddot{\Lambda}^n\right) \end{cases} \tag{3.3.6}$$

where in our case $\Lambda = \begin{pmatrix} \chi \\ \zeta \\ \theta \end{pmatrix}$ and $\mathcal{H}$ is given in (3.2.5).

In the following, we take $\alpha = \beta = 1$ since the source term $p_k^{n+1} \partial_t^{n+1} R_k$ in (3.3.5) corresponding to the movement of the structure is implicit. This is required to get the discrete energy stability, see Proposition 3.3.1. Note that with this choice, the Newmark scheme is completely implicit and of first order. For the approximation of the integrals in (3.2.5) we take

$$\begin{cases} M \ddot{\chi}^n = -\displaystyle\sum_{k \in \mathbb{T}} |k| p_k^n \partial_k^\delta R^n + F_\chi^n & (3.3.7) \\ M \ddot{\zeta}^n = -Mg + \displaystyle\sum_{k \in \mathbb{T}} |k| p_k^n + F_\zeta^n & (3.3.8) \\ \mathcal{J}_G \ddot{\theta}^n = \displaystyle\sum_{k \in \mathbb{T}} |k| p_k^n \partial_\theta^\delta R_k^n + T_\theta^n & (3.3.9) \end{cases}$$

where $\partial_k^\delta R^n$ (resp. $\partial_\theta^\delta R_k^n$) are discretizations of the derivative of the roof with respect to x (resp. θ) at time t^n. These terms will be discussed below in order to obtain the energy stability for the coupled fluid-solid model. Let us first state the energy stability for the Newmark scheme.

Lemma 3.3.2. *The scheme (3.3.6)-(3.3.9) satisfies the following energy law*

$$\begin{aligned}\partial_t^{n+1}E &= -\left(\sum_{k\in\mathbb{T}}\left(|k|\partial_k^\delta R^{n+1}p_k^{n+1}\right) - F_\chi^{n+1}\right)\partial_t^{n+1}\chi \\ &\quad + \left(\sum_{k\in\mathbb{T}}\left(|k|p_k^{n+1}\right) + F_\zeta^{n+1}\right)\partial_t^{n+1}\zeta \\ &\quad + \left(\sum_{k\in\mathbb{T}}\left(|k|\partial_\theta^\delta R_k^{n+1}p_k^{n+1}\right) + T_\theta^{n+1}\right)\partial_t^{n+1}\theta\end{aligned} \tag{3.3.10}$$

with $E^n = E\left(\chi^n, \zeta^n, \theta^n\right)$ defined in Lemma 3.2.2.

Proof. The proof for the general ODE case is detailed in [70, section 3]. Using a Newmark scheme for the linear equation of motion on a vector of unknowns Λ

$$C_1\ddot{\Lambda}^n + C_2\dot{\Lambda}^n + C_3\Lambda^n = f^n \tag{3.3.11}$$

where C_1, C_2 and C_3 are matrices and f a vector representing the external forces, the author proves the following energy equation

$$\begin{aligned}\partial_t^{n+1}\left(\frac{1}{2}\dot{\Lambda}\cdot\left(C_1 + \frac{\delta_t^{n+1}}{2}C_2\right)\dot{\Lambda} + \frac{1}{2}\Lambda\cdot C_3\Lambda\right) &= -\frac{\delta_t^{n+1}}{2}\partial_t^{n+1}\Lambda\cdot C_3\partial_t^{n+1}\Lambda \\ &\quad + \partial_t^{n+1}\Lambda\cdot f^{n+1} \\ &\quad - \frac{1}{2}\left(\partial_t^{n+1}\Lambda\cdot C_2\partial_t^{n+1}\Lambda\right) - \frac{1}{2}\left(\frac{\dot{\Lambda}^{n+1}+\dot{\Lambda}^n}{2}\cdot C_2\frac{\dot{\Lambda}^{n+1}+\dot{\Lambda}^n}{2}\right).\end{aligned}$$

Applied in our case by setting $C_1 = \begin{pmatrix} M & 0 & 0 \\ 0 & M & 0 \\ 0 & 0 & \mathcal{J}_G \end{pmatrix}$, $C_2 = 0$, $C_3 = 0$ and $f^n = \begin{pmatrix} -\sum_{k\in\mathbb{T}}|k|p_k^n\partial_k^\delta R^n + F_\chi^n \\ -Mg + \sum_{k\in\mathbb{T}}|k|p_k^n + F_\zeta^n \\ \sum_{k\in\mathbb{T}}|k|p_k^n\partial_\theta^\delta R_k^n + T_\theta^n \end{pmatrix}$, we conclude since we have $\partial_t^{n+1}E =$

$$\partial_t^{n+1}\left(\frac{1}{2}\dot{\Lambda}\cdot C_1\dot{\Lambda}\right) + Mg\partial_t^{n+1}\zeta. \qquad \square$$

3.3.3 Coupling strategy between the fluid and the solid

Let us now concentrate on the discrete coupling. We will discuss the form of $\partial_k^\delta R^n$ and $\partial_\theta^\delta R_k^n$ in (3.3.7)-(3.3.9) and analyze the energy of the coupled system. A first naive approach that is not entropy satisfying will be given. In a second paragraph an adapted choice for $\partial_k^\delta R^n$ and $\partial_\theta^\delta R_k^n$ will be explained. It is introduced in order to obtain an energy dissipation law.

3.3.3.1 A first approach

In this section a straightforward discretization for $\partial_k^\delta R^n$ and $\partial_\theta^\delta R_k^n$ is analyzed. We take $\partial_k^\delta R^n = \partial_k^C R^n$ and $\partial_\theta^\delta R_k^n = \partial_\theta^C R_k^n$ in (3.3.7)-(3.3.9), where

$$\partial_k^C R^n = \frac{R_{k+1}^{n-1} - R_{k-1}^{n-1}}{2|k|} \quad \text{and} \quad \partial_\theta^C R_k^n = -\left(R_k^{n-1} - \zeta^{n-1}\right)\partial_k^C R^n - \left(x_k - \chi^{n-1}\right). \tag{3.3.12}$$

The choice for $\partial_k^C R^n$ is a centered discretization of $\partial_x \mathcal{R}$ and the discretization of $\partial_\theta^C R_k^n$ comes from (3.2.11). More precisely $\partial_\theta^C R_k^n$ is a discretization of $-GX\cdot e_z \partial_x\mathcal{R} - GX\cdot e_x$.
A discrete energy inequality for the coupled fluid-solid system can be written.

Lemma 3.3.3. *Consider a no-flux boundary on Ω_x. Then the scheme (3.3.1)-(3.3.3) and (3.3.6)-(3.3.9) with (3.3.12) admits the following energy inequality*

$$\begin{aligned}\partial_t^{n+1}\left(\sum_{k\in\mathbb{T}}|k|\mathcal{E}_k + E\right) \le \sum_{k\in\mathbb{T}}\left(|k|\left(gh_k^n + p_k^{n+1}\right)\partial_t^{n+1}B_k\right)\\ + F_\zeta^{n+1}\partial_t^{n+1}\zeta - F_\chi^{n+1}\partial_t^{n+1}\chi + T_\theta^{n+1}\partial_t^{n+1}\theta\\ + \sum_{k\in\mathbb{T}}|k|p_k^{n+1}\left(-\partial_t^{n+1}R_k - \partial_t^{n+1}\chi\partial_k^\delta R^{n+1} + \partial_t^{n+1}\zeta + \partial_t^{n+1}\theta\partial_\theta^\delta R_k^{n+1}\right).\end{aligned} \tag{3.3.13}$$

Proof. Summing (3.3.5) over the computational domain and adding (3.3.10) gives the result. $\square$

Except for the last sum, the energy inequality (3.3.13) is consistent with the energy given in Proposition 3.2.2. Since we do not have an equivalent condition to (3.2.12) at the discrete level, the last sum in (3.3.13) does not

vanish and its sign cannot be determined. As a consequence no energy stability is obtained. However a simple choice of discretization for $\partial_k^\delta R^n$ and $\partial_\theta^\delta R_k^n$ can be made to get an energy balance law for the system at the discrete level. This will be explained in the next section.

3.3.3.2 Entropy correction

Let us now discuss a choice for $\partial_k^\delta R^n$ and $\partial_\theta^\delta R_k^n$ such that the energy stability is ensured. Let

$$\partial_k^\delta R^n = \begin{cases} \dfrac{\partial_t^n \zeta - \partial_t^n R_k}{\partial_t^n \chi}, & \text{if } \partial_t^n \chi \neq 0 \text{ and } \partial_t^n \theta = 0 \\ \partial_k^C R^n, & \text{else} \end{cases} \tag{3.3.14}$$

and

$$\partial_\theta^\delta R_k^n = \begin{cases} \dfrac{\partial_t^n R_k + \partial_t^n \chi \partial_k^C R^n - \partial_t^n \zeta}{\partial_t^n \theta}, & \text{if } \partial_t^n \theta \neq 0 \\ \partial_\theta^C R_k^n, & \text{else.} \end{cases} \tag{3.3.15}$$

For (3.3.14)-(3.3.15) to be numerically well defined when $\partial_t^n \chi \to 0$ (resp. $\partial_t^n \theta \to 0$) a tolerance is introduced in practice, see Section 3.3.4. With (3.3.14)-(3.3.15), an energy dissipation law can be proven.

Proposition 3.3.1. *Consider a no-flux boundary on Ω_x. Then the scheme (3.3.1)-(3.3.3) and (3.3.6)-(3.3.9) with (3.3.14)-(3.3.15) admits the following dissipation law*

$$\partial_t^{n+1}\left(\sum_{k\in\mathbb{T}} |k|\mathcal{E}_k + E\right) \leq \sum_{k\in\mathbb{T}} \left(|k|\left(gh_k^n + p_k^{n+1}\right)\partial_t^{n+1} B_k\right) + F_\zeta^{n+1}\partial_t^{n+1}\zeta - F_\chi^{n+1}\partial_t^{n+1}\chi + T_\theta^{n+1}\partial_t^{n+1}\theta.$$

Proof. Following the inequality of Lemma 3.3.3, it is sufficient to prove that

$$-\partial_t^{n+1} R_k - \partial_t^{n+1}\chi \partial_k^\delta R^{n+1} + \partial_t^{n+1}\zeta + \partial_t^{n+1}\theta \partial_\theta^\delta R_k^{n+1} = 0. \tag{3.3.16}$$

Replacing the expressions of $\partial_k^\delta R^n$ and $\partial_\theta^\delta R_k^n$ from (3.3.14)-(3.3.15) in (3.3.16) concludes the proof. □

The choice (3.3.14)-(3.3.15) is made to impose (3.2.12) at the discrete level. The consistency of (3.3.14)-(3.3.15) with the respective derivative is therefore straightforward. If $\partial_t^n \chi = 0$ and $\partial_t^n \theta = 0$ there is no condition to verify and any choice can be made for $\partial_k^\delta R^n$ and $\partial_\theta^\delta R_k^n$. In the case where $\partial_t^n \theta = 0$ or $\partial_t^n \chi = 0$, a condition on $\partial_\theta^\delta R_k^n$ (resp. $\partial_k^\delta R^n$) is obtained to verify (3.2.12) at the discrete level. In the last case, i.e. $\partial_t^n \chi \neq 0$ and $\partial_t^n \theta \neq 0$, a condition is imposed on $\partial_\theta^\delta R_k^n$, i.e. $\partial_\theta^\delta R_k^n = \dfrac{\partial_t^n R_k + \partial_t^n \chi \partial_k^\delta R^n - \partial_t^n \zeta}{\partial_t^n \theta}$ and any discretization for $\partial_k^\delta R^n$ can be chosen.

3.3.4 Practical details

Some details about the practical implementation are given below.

Correction near equilibrium

For (3.3.14)-(3.3.15) to be numerically well defined when $\partial_t^n \chi \to 0$ (resp. $\partial_t^n \theta \to 0$), a tolerance $\varepsilon_t > 0$ is introduced in practice, i.e.

$$\partial_k^\delta R^n = \begin{cases} \dfrac{\partial_t^n \zeta + \partial_t^n \theta \partial_\theta^C R_k^n - \partial_t^n R_k}{\partial_t^n \chi}, & \text{if } |\chi^{n+1} - \chi^n| > \varepsilon_t \text{ and } |\theta^{n+1} - \theta^n| < \varepsilon_t \\ \partial_k^C R^n, & \text{else} \end{cases} \tag{3.3.17}$$

and

$$\partial_\theta^\delta R_k^n = \begin{cases} \dfrac{\partial_t^n R_k + \partial_t^n \chi \partial_k^C R^n - \partial_t^n \zeta}{\partial_t^n \theta}, & \text{if } |\theta^{n+1} - \theta^n| > \varepsilon_t \\ \partial_\theta^C R_k^n, & \text{else.} \end{cases} \tag{3.3.18}$$

Considering a no-flux boundary on Ω_x as well as a smooth enough roof, there exists $\Xi \in \mathbb{R}$ such that the scheme (3.3.1)-(3.3.3) and (3.3.6)-(3.3.9) with (3.3.17)-(3.3.18) admits the following energy inequality

$$\begin{aligned} \partial_t^{n+1} \left(\sum_{k \in \mathbb{T}} |k| \mathcal{E}_k + E \right) \leq & \sum_{k \in \mathbb{T}} \left(|k| \left(p_k^{n+1} + g h_k^n \right) \partial_t^{n+1} B_k \right) \\ & + F_\zeta^{n+1} \partial_t^{n+1} \zeta - F_\chi^{n+1} \partial_t^{n+1} \chi + T_\theta^{n+1} \partial_t^{n+1} \theta \\ & + \Xi \, \varepsilon_t. \end{aligned}$$

In the considered applications, the buoy is supposed smooth enough and is moving, i.e. $|\theta^{n+1} - \theta^n| > \varepsilon_t$ or $|\chi^{n+1} - \chi^n| > \varepsilon_t$. Thus the energy between the solid and the fluid is perfectly controlled. Close to the equilibrium, i.e. $|\theta^{n+1} - \theta^n| < \varepsilon_t$ and $|\chi^{n+1} - \chi^n| < \varepsilon_t$, the energy is not perfectly preserved, but is bounded by an arbitrary small parameter.

Fixed point approach

The scheme (3.3.1)-(3.3.3) is implicit and non-linear on the potential. An iterative Newton process on the potential is explained in [55] to solve it at each time step. The fixed point resolution has to be adapted to take into account the dynamics of the buoy. More precisely the iterations will be done on the variable $W^n = (\phi^n, \Lambda^n)$.
The derivatives of the water height with respect to χ, ζ and θ depend on the shape of the buoy which makes the Jacobian difficult to be computed. Therefore a semi-Newton fixed point is implemented, for which the latter derivatives are not taken into account. As a consequence no quadratic convergence is recovered.
Two stopping criteria are used to increase the reliability of the result. If the L^∞-norm of the residual and $\|W^{n,q+1} - W^{n,q}\|_\infty$ are inferior to a tolerance ε_{Newton}, we set $W^{n+1} = W^{n,q+1}$.
A large time step given by (3.3.4) which takes into account only the fluid is not necessarily adapted to the induced large buoy movement and can result in a large number of fixed point iterations. To avoid two-way wiring in the fixed point, the time step is limited if necessary, see for example [28] for time step adaptation in a fixed point method. We set a maximum acceptable number of iterations i_{max} in the fixed point. If the Newton fixed point takes too many iterations to converge, the time step is reduced, i.e. $\delta_t^{n,q+1} = \omega \delta_t^{n,q}$ with a reduction factor $\omega < 1$ and the time iteration is recomputed, i.e. $W^{n,q+1} = W^n$.
The implicit CFL condition (3.3.4) is verified for every time iteration at convergence to ensure the scheme to be entropy satisfying, see Lemma 3.3.1. If the CFL condition is not verified, the time iteration is recomputed using the time step given by (3.3.4).
In practice the fixed point algorithm converges in a few iterations with reasonable time steps. The performance of the fixed point will be given for each test case done below. A rigourous proof of convergence for the fixed point has not been done in this work.

Buoy implementation

The roof R_k^n is an approximation of $R_0(x-\chi^n,\theta^n)+\zeta^n$ at the point x_k, see (3.2.4). However since an explicit expression of R_0 is not easy to have, even for a simple geometry, let us explain in the following the numerical implementation of the geometry of the buoy.
In practice the buoy is represented by a finite sequence of points

$$\mathcal{S}_0 = ((X_i, Z_i))_{i\in[\![1,N_P]\!]}$$

with N_P the number of points. The points describe in the reference frame of the center of mass with $\theta = 0$ and in anti-clockwise order the vertices of a polygon approaching the geometry of the buoy. Thus at time t^n and in the observational frame of reference, the buoy with a rotation of angle θ^n is described by the sequence of points

$$\mathcal{S} = \left\{ M_{\theta^n}\begin{pmatrix} X \\ Z \end{pmatrix} + \begin{pmatrix} \chi^n \\ \zeta^n \end{pmatrix} \mid \begin{pmatrix} X \\ Z \end{pmatrix} \in \mathcal{S}_0 \right\}$$

where M_{θ^n} is defined in (3.2.9).
Let $i_-^n = \{i \in [\![1,N_P]\!] \mid (X_i,Z_i) \in \mathcal{S} \text{ and } \forall j \in [\![1,N_P]\!]\ X_i \le X_j\}$ and $i_+^n = \{i \in [\![1,N_P]\!] \mid (X_i,Z_i) \in \mathcal{S} \text{ and } \forall j \in [\![1,N_P]\!]\ X_i \ge X_j\}$. The lower part of the buoy is defined by the subsequence

$$S^- = \left(\left(X_{\psi(i)}, Z_{\psi(i)}\right)\right)_{i\in I}$$

with

$$\psi : i \mapsto \left(i + i_-^n - 2\right) \mod N_p + 1$$

and

$$I = \left\{1, 2, ..., (i_+^n - i_-^n + 1) \mod N_p\right\}.$$

For any point x_k not under the buoy, i.e. $x_k < X_{i_-^n}$ or $x_k > X_{i_+^n}$, the roof is defined high enough not to touch the fluid surface. In the part of the domain where the buoy is, i.e. $X_{i_-^n} \le x_k \le X_{i_+^n}$, the roof is deduced from $\mathcal{S}^-$. For $k \in \mathbb{T}$, let $\left(X_k^-, Z_k^-\right) = \{(X_i,Z_i) \in \mathcal{S}^- \mid X_i = \max_{X_j \le x_k} X_j\}$ and $\left(X_k^+, Z_k^+\right) = \{(X_i,Z_i) \in \mathcal{S}^- \mid X_i = \min_{X_j \ge x_k} X_j\}$. In other words, $\left(X_k^-, Z_k^-\right)$ (resp. $\left(X_k^+, Z_k^+\right)$) is the nearest vertice from the left (respectively from the right) to x_k among the sequence of points $\mathcal{S}^-$. To get an approximation of the roof in x_k a linear interpolation between Z_k^- and Z_k^+ is done, i.e. $R_k^n = \dfrac{\left(x_k - X_k^-\right) Z_k^+ + \left(X_k^+ - x_k\right) Z_k^-}{X_k^+ - X_k^-}$.

3.4 Simulations

We illustrate the validity of our coupled numerical model by some one dimensional computations.
A first test case is the return to equilibrium problem. A reference solution is given in [73] through the resolution of a nonlinear ODE. The simulation is compared to this reference solution and the order of convergence is computed. In order to show the robustness of the code, a second test case where a structure with initial velocity is falling into water at rest is proposed.
The last test case shows the ability to simulate wave energy converters.

In the following we take $g = 9.81$. The length of the domain Ω_x and the final time of simulation are respectively denoted by l and $\mathcal{T}$. The space step using a regular grid is denoted by δ_x. The relaxation parameter is chosen as $\lambda = \sqrt{\delta_x}$, see [55] for more details about this choice. The CPR-parameter γ is set to 2. It is slightly increased compared to the optimal value necessary to get the entropy in Lemma 3.3.1. This has a regularizing effect (see [90]) and prevents oscillations which can be observed with the CPR scheme in the vicinity of a shock. For all the test cases $\varepsilon_{Newton} = 1 \times 10^{-8}$, $i_{max} = 15$, $\varepsilon_t = \varepsilon_{Newton}$ and $\omega = \frac{1}{4}$.

3.4.1 Return to equilibrium

We consider a test case modeling a return to equilibrium for which an analytical solution is proposed in [73, Corollary 1]. It corresponds to the vertical movement of an object initially at rest and with the water at rest, starting from a configuration where it is not at its equilibrium position denoted by ζ_{eq} and evolving towards it. The equilibrium of the buoy is defined by $u = 0$, $\phi = \phi_0 \in \mathbb{R}$, $\dot{\zeta} = 0$ and $\zeta = \zeta_{eq}$ such that

$$Mg = \int_{\Omega_x} p_\eta \mathrm{d}x. \tag{3.4.1}$$

In other words the equilibrium is the situation where the surface pressure balances out the weight of the buoy. Only a vertical movement is considered for this test case. More precisely we suppose that

$$F_\chi = \int_{\Omega_x} p_\eta \partial_x \mathcal{R} \mathrm{d}x, \qquad T_\theta = -\int_{\Omega_x} p_\eta \partial_\theta \mathcal{R} \mathrm{d}x \qquad \text{and} \qquad F_\zeta = 0 \tag{3.4.2}$$

which expresses the fact that the horizontal and angular degrees of freedom are fixed.

We define $\delta_G = \zeta - \zeta_{eq}$ the distance of the center of mass to the equilibrium position with the initial conditions $\delta_G^0 = \zeta^0 - \zeta_{eq}$ and $\dot{\delta_G^0} = \dot{\zeta}^0$. The water height corresponding to the equilibrium position is denoted h_{eq}. A rectangular buoy is considered which corresponds to a flat roof. The length of the roof is equal to $l_R = 0.8$ and the roof is defined so that it is symmetric with respect to its center of mass. A flat bottom is considered for simplicity. For the above defined configuration, the position of the center of mass is determined by

$$\left(M + \frac{2}{3\zeta}\left(\frac{l_R}{2}\right)^3\right)\ddot{\delta_G} = -gl_R\delta_G - \nu\left(\dot{\delta_G}\right) + \mu\left(\delta_G\right)\dot{\delta_G}^2 \tag{3.4.3}$$

with the coefficients

$$\nu\left(\dot{\delta_G}\right) = gl_R\left(h_{eq} - \tau\left(\frac{l_R}{4\sqrt{g}}\dot{\delta_G}\right)^2\right)$$

and

$$\mu\left(\delta_G\right) = \frac{4}{3\zeta^2}\left(\left(\frac{l_R}{2} - \chi^0\right)^3 + \left(\chi^0\right)^3\right).$$

The coefficient τ is given by

$$\tau\left(r\right) = \frac{1}{3}\left(\sqrt{h_{eq}} + C\left(r\right) + \frac{h_{eq}}{C\left(r\right)}\right)$$

with

$$C\left(r\right) = \frac{3}{2}\left(-4r + \frac{8}{27}h_{eq}^{\frac{3}{2}} + 4\sqrt{r\left(r - \frac{4}{27}h_{eq}^{\frac{3}{2}}\right)}\right)^{\frac{1}{3}}.$$

The simulation is done in a domain of length $l = 40$. The final time $\mathcal{T}$ is equal to 4 and the mass $M = 0.5$. We consider an equilibrium with $\zeta_{eq} = 1$ and the water depth h_{eq} satisfying (3.4.1). The initial conditions read $\phi^0 = gh_{eq}$ and $\overline{u}^0 = 0$. Initially the position of the center of mass is $\chi^0 = 20$, $\zeta^0 = 1.2$ and $\theta^0 = 0$ and it has a null velocity. The initial position is above the equilibrium position.

The simulation is compared to the reference solution in Figure 3.2. More precisely the evolution in time of the distance to the equilibrium position δ_G is shown. The agreement between the two solutions is good and the solution tends to the equilibrium position as expected. The convergence rate in L^2-norm for δ_G is shown in Figure 3.3. The error computed corresponds to the L^2-norm of the difference between the 'exact' (obtained by solving the ODE (3.4.3)) and the computed position of the center of mass over the time interval

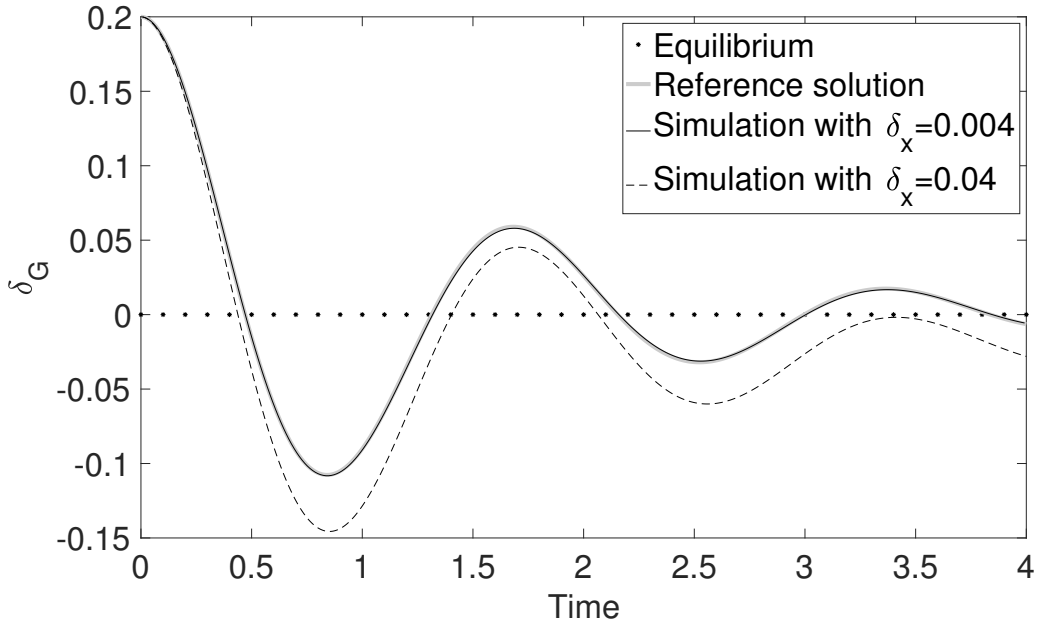

Figure 3.2 – Return to equilibrium: evolution of the distance to the equilibrium position in time

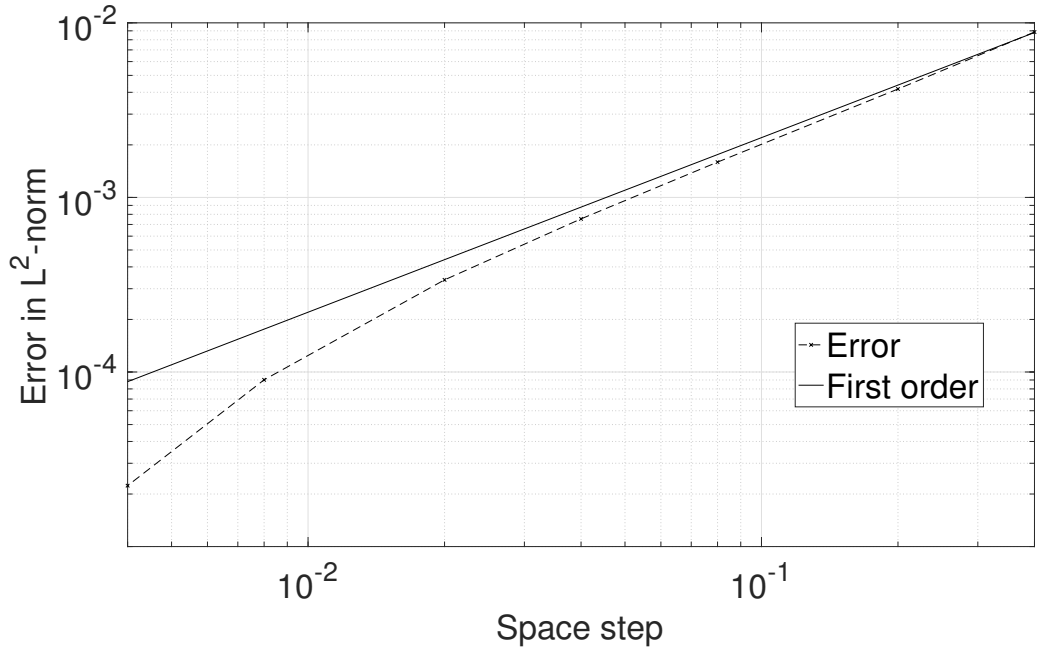

Figure 3.3 – Return to equilibrium: Convergence rate in L^2-norm for δ_G compared to first order

$[0, 4]$. A slightly better than first order convergence is obtained. By taking $\alpha = \beta = 1$, the Newmark scheme is completely implicit and therefore of first order as already noted.

Remark 3.4.1. *Note that in a symmetric case, the two first equalities in* (3.4.2) *become* $F_\chi = T_\theta = 0$. *In fact, in this particular case,* $\int_{\Omega_x} p_\eta \partial_x \mathcal{R} \mathrm{d}x = 0$ *and* $\int_{\Omega_x} p_\eta \partial_\theta \mathcal{R} \mathrm{d}x = 0$. *Although neither horizontal nor angular acceleration should be noticed in such a configuration, see* (3.2.5), *in practice, due to the fixed point error, small oscillations can appear in long time. For this reason, even with an axisymmetric buoy* (3.4.2) *is imposed.*

3.4.2 Throwing

We now consider a test case modeling the movement of a buoy thrown into the water and then allowed to float freely.

We consider a closed domain with flat bottom and length $l = 4$. The water is initially at rest, i.e. $\phi^0 = g$ and $u^0 = 0$, with $F_\chi = 0$, $F_\zeta = 0$ and $T_\theta = 0$. The buoy is an ovoid parametrized by $(0.3\cos(s) + 0.025\cos(2s), 0.2\sin(s))$ for $s \in [0, 2\pi]$. The initial value of the buoy velocity is $\dot{\chi}^0 = 1.0$, $\dot{\zeta}^0 = 1.0$ and $\dot{\theta}^0 = 1.0$. The initial position of the ovoid is defined by $\chi^0 = 0.4$, $\zeta^0 = 1.5$ and $\theta^0 = \dfrac{\pi}{2}$. The mass M and the angular moment $\mathcal{J}_G$ of the buoy are taken equal to 5×10^{-3} and 1×10^{-3}.

Taking 1000 grid points, the space step is $\delta_x = 4.0 \times 10^{-3}$ and the final time $\mathcal{T}$ is equal to 1.5.

The buoy position, the water height and the surface pressure at different times are shown in Figure 3.4. At the beginning the fluid is at rest and the buoy is not in contact with the fluid. At the impact an energy transfer from the buoy to the water is observed and small waves are created. The buoy continues moving to the right and moreover angular and vertical oscillations are observed. The evolution of the mechanical energy in time is shown in Figure 3.5. More precisely the energy ratio $\dfrac{\sum_{k\in\mathbb{T}} \delta_x \mathcal{E}_k(t) + E(t)}{\sum_{k\in\mathbb{T}} \delta_x \mathcal{E}_k(0) + E(0)}$ is shown. The result is in accordance with Proposition 3.3.1. More precisely a dissipation of the mechanical energy is observed. The fixed point converges with a mean time step of 7.69×10^{-4} and the mean number of calls of the linear system resolution per time step is equal to 35. This seems satisfactory in terms of numerical costs. The mean time step $\overline{\delta_t}$ (second row), the mean number of calls $\overline{\#_{resol}}$ of the linear system resolution per time step (third row) and the total number of calls $\#_{resol}$ of the linear system resolution (fourth row) for different values of the time step reduction factor ω (first row) are shown in Table 3.a.

ω	0.1	0.25	0.5	0.75	0.9
$\overline{\delta_t}$	6.21×10^{-4}	7.69×10^{-4}	1.25×10^{-3}	1.47×10^{-3}	1.61×10^{-3}
$\overline{\#_{resol}}$	26	35	46	82	192
$\#_{resol}$	63634	68493	54611	84074	117403

Table 3.a – Throwing: the mean time step, the mean number of calls of the linear system resolution per time step and the total number of calls of the linear system resolution for different values of ω.

By increasing the parameter ω, the mean time step as well as the mean number of calls of the linear system resolution per time step increase. This seems natural but makes the choice for an optimal value quite difficult. More precisely the CPU time decreases with a bigger time step but increases with the number of calls of the linear system resolution. As a consequence the choice for ω highly depends on the test case. In this particular case the best value seems to be obtained around $\omega = 0.5$.

3.4.3 Wave energy converter

To simulate an energy converter, a spring is added to the modelization from section 3.2.2, see Figure 3.6. A restoring as well as damping force will be taken into account to modelize the energy extraction. The structure is allowed to move vertically and to rotate around its center of mass and it is fixed in the horizontal direction, i.e. $F_\zeta = -c\dot{\zeta} - K\left(\zeta - \overline{\zeta}\right)$, $T_\theta = 0$ and $F_\chi = \int_{\Omega_x} p_\eta \partial_x \mathcal{R} \mathrm{d}x$. The damping (resp. stiffness) coefficients are denoted $c \in \mathbb{R}_+$ (resp. $K \in \mathbb{R}_+$). The characteristic length of the spring is denoted $\overline{\zeta}$. Let us rewrite the equations from section 3.2.2 in the case where we add a spring. The proofs will not be detailed since they are an adaptation of those done for the corresponding results cited previously.

The planar movement of the energy wave converter is described by the system

$$\begin{cases} M\ddot{\zeta} = -Mg + \displaystyle\int_{\Omega_x} p_\eta \mathrm{d}x - c\dot{\zeta} - K\left(\zeta - \overline{\zeta}\right) \\ \mathcal{J}_G \ddot{\theta} = \displaystyle\int_{\Omega_x} p_\eta \partial_\theta \mathcal{R} \mathrm{d}x. \end{cases} \tag{3.4.4}$$

The energy for the solid can be written.

Lemma 3.4.1. *Any smooth solution of* (3.4.4) *satisfies the following energy*

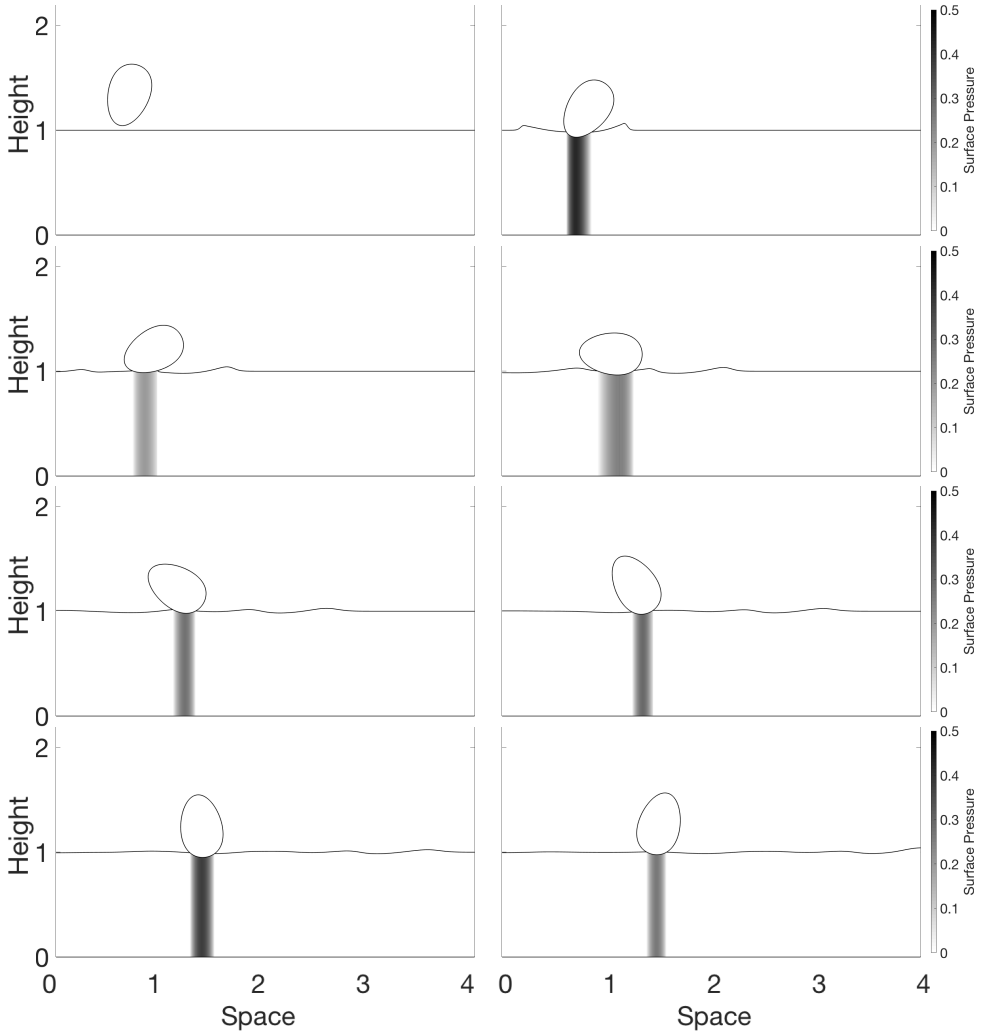

Figure 3.4 – Throwing: buoy, water height and surface pressure from $t = 0.3$ to $t = 1.35$ at regular intervals

law

$$\partial_t \widetilde{E} = \int_{\Omega_x} p_\eta \partial_\theta \mathcal{R} \mathrm{d}x \dot{\theta} + \int_{\Omega_x} p_\eta \mathrm{d}x \dot{\zeta} - c\dot{\zeta}^2$$

with $\widetilde{E}(\zeta, \theta) = \dfrac{\mathcal{J}_G}{2}\dot{\theta}^2 + \dfrac{M}{2}\dot{\zeta}^2 + Mg\zeta + \dfrac{K}{2}\left(\zeta - \overline{\zeta}\right)^2$.

The energy for the coupled fluid-solid system is obtained.

Proposition 3.4.1. *Considering a no-flux boundary on* Ω_x*, any smooth solution of* (3.4.4) *and* (3.2.1)-(3.2.2) *satisfies the following energy balance*

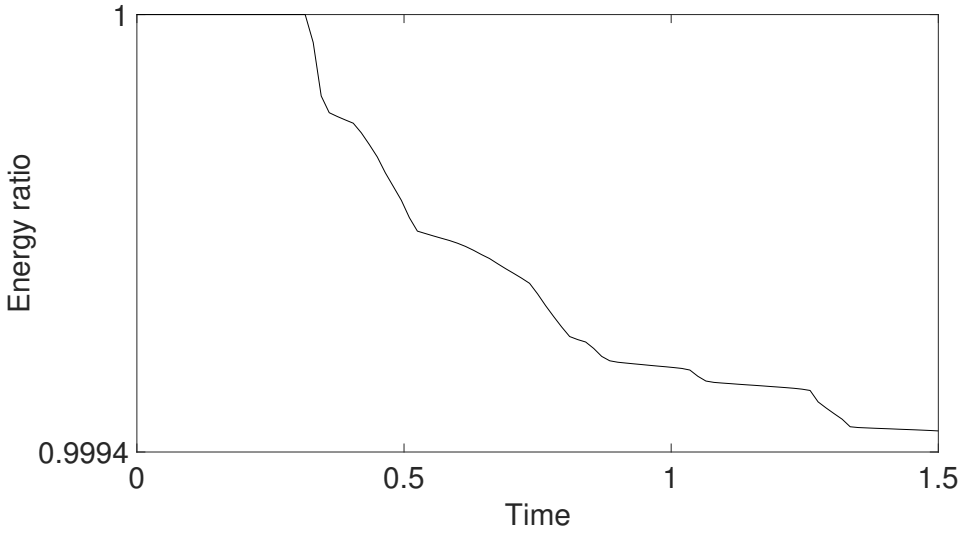

Figure 3.5 – Throwing: mechanical energy ratio evolution in time

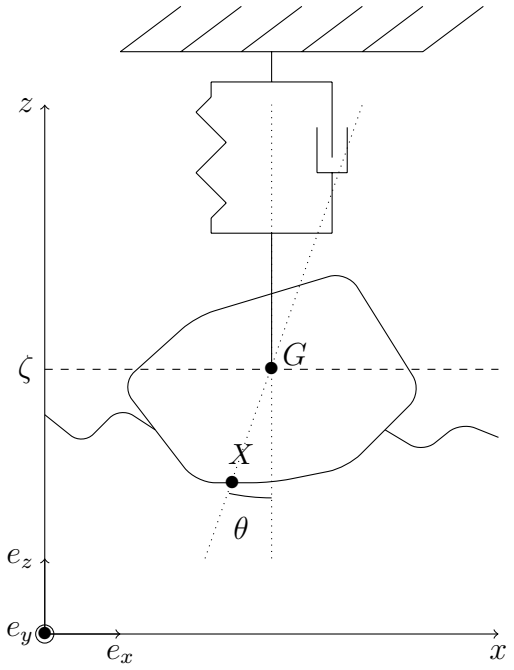

Figure 3.6 – Wave energy converter with a spring

law

$$\partial_t \left(\int_{\Omega_x} \mathcal{E} \, \mathrm{d}x + \widetilde{E} \right) = \int_{\Omega_x} (p_\eta + gh) \, \partial_t B \mathrm{d}x - c\dot{\zeta}^2.$$

The term $c\dot{\zeta}^2$ is a dissipation term due to the damping of the spring. A part of this energy could be recovered for energy production.

Using again the Newmark scheme (3.3.6) with $\widetilde{\Lambda} = \begin{pmatrix} \zeta \\ \theta \end{pmatrix}$, (3.4.4) is discretized in the following way

$$\begin{cases} M\ddot{\zeta}^n = -Mg + \displaystyle\sum_{k\in\mathbb{T}} |k| p_k^n - c\dot{\zeta}^n - K\left(\zeta^n - \overline{\zeta}\right) \\ \mathcal{J}_G \ddot{\theta}^n = \displaystyle\sum_{k\in\mathbb{T}} |k| p_k^n \partial_\theta^\delta R_k^n. \end{cases} \tag{3.4.5}$$

As before the discrete energy stability is proven for the adapted discretization of $\partial_\theta^\delta R_k^n$. Let us first recall the energy for the Newmark scheme.

Lemma 3.4.2. *The scheme* (3.3.6) *and* (3.4.5) *satisfies the following energy law*

$$\begin{aligned} \partial_t^{n+1} \left(\widetilde{E} + \frac{\delta_t^{n+1}}{4} \left(\dot{\zeta}\right)^2 \right) &= \sum_{k\in\mathbb{T}} \left(|k| p_k^{n+1} \partial_\theta^\delta R_k^{n+1} \right) \partial_t^{n+1} \theta + \sum_{k\in\mathbb{T}} |k| p_k^n \partial_t^{n+1} \zeta \\ &\quad - P_c^{n+1} - K \frac{\delta_t^{n+1}}{2} \left(\partial_t^{n+1}\zeta\right)^2 \end{aligned}$$

with $\widetilde{E}^n = \widetilde{E}\left(\zeta^n, \theta^n\right)$ *and* $P_c^{n+1} = \dfrac{c}{2} \left(\left(\partial_t^{n+1}\zeta\right)^2 + \left(\dfrac{\dot{\zeta}^{n+1} + \dot{\zeta}^n}{2} \right)^2 \right)$.

Proof. The proof is similar to the proof of Lemma 3.3.2. The coefficients are (with obvious notations) $\widetilde{f}^n = \begin{pmatrix} -Mg + K\overline{\zeta} + \displaystyle\sum_{k\in\mathbb{T}} |k| p_k^n \\ \displaystyle\sum_{k\in\mathbb{T}} |k| p_k^n \partial_\theta^\delta R_k^n \end{pmatrix}$, $\widetilde{C}_1 = \begin{pmatrix} M & 0 \\ 0 & \mathcal{J}_G \end{pmatrix}$, $\widetilde{C}_2 = \begin{pmatrix} c & 0 \\ 0 & 0 \end{pmatrix}$ and $\widetilde{C}_3 = \begin{pmatrix} K & 0 \\ 0 & 0 \end{pmatrix}$. □

For the adapted choice of discretization for $\partial_\theta^\delta R_k^n$, see (3.3.15), the energy stability is achieved for the coupled fluid-solid system. Note that $\partial_t^n \chi = 0$ in (3.3.15) since the structure is fixed in the horizontal direction.

Proposition 3.4.2. *Consider a no-flux boundary on Ω_x. Then the scheme (3.3.1)-(3.3.3), (3.3.6) and (3.4.5) with (3.3.15) admits the following dissipation law*

$$\partial_t^{n+1}\left(\sum_{k\in\mathbb{T}}|k|\mathcal{E}_k+\widetilde{E}+\frac{\delta_t^{n+1}}{4}\left(\dot{\zeta}\right)^2\right)\leq\sum_{k\in\mathbb{T}}\left(|k|\left(gh_k^n+p_k^{n+1}\right)\partial_t^{n+1}B_k\right)-P_c^{n+1}-K\frac{\delta_t^{n+1}}{2}\left(\partial_t^{n+1}\zeta\right)^2.$$

In the following a simple case of a wave energy converter attached to a spring is simulated.
The buoy is an ellipse with semi-minor and semi-major axis respectively equal to 0.2 and 0.4. Its mass M is equal to 1.0×10^{-2} and the moment of inertia $\mathcal{J}_G$ equals 5.0×10^{-3}. The stiffness coefficients K and the characteristic length $\overline{\zeta}$ are $K=1.0\times10^{-2}$ respectively $\overline{\zeta}=1.4$. At the left boundary waves of the form $h(t)=h^0+0.05\sin(4\pi t)$ enter the domain. At the right boundary we impose a non-flux boundary condition. Furthermore the initial horizontal coordinate χ and vertical coordinate ζ of the center of mass are $\chi=1.5$ respectively $\zeta=1.4$. Initially $\dot{\zeta}=0$, $\theta^0=\frac{\pi}{2}$, $\dot{\theta}^0=0$, $\overline{u}^0=0$ and $\phi^0=\phi_0$ so that the buoy is at equilibrium, see Section 3.4.1

Taking 1000 grid points and a domain with flat bottom of length $l=3$, the space step $\delta_x=3.0\times10^{-3}$. The final time $\mathcal{T}$ is equal to 1.

The optimisation of wave energy converters is a key point in the development of such devices. To show the feasibility of an optimisation procedure, a naive estimation of the recoverable energy is done. The recovered energy, depending on the technology used to convert wave energy, is a part of the recoverable energy defined by

$$E_c=\sum_{n\in\{1,\dots,N\}}\delta_t^nP_c^n$$

where N is the number of time iterations and P_c^n defined in Lemma 3.4.2. In Figure 3.7 the ratio between the recoverable energy E_c and the total introduced energy $\mathcal{E}_{tot}$ is shown for different values of c. The total introduced energy is computed by considering the previous simulation without the buoy. More precisely it is defined by

$$\mathcal{E}_{tot}=\sum_{n\in\{1,\dots,N\}}\delta_t^n\partial_t^n\left(\sum_{k\in\mathbb{T}}|k|\mathcal{E}_k\right).$$

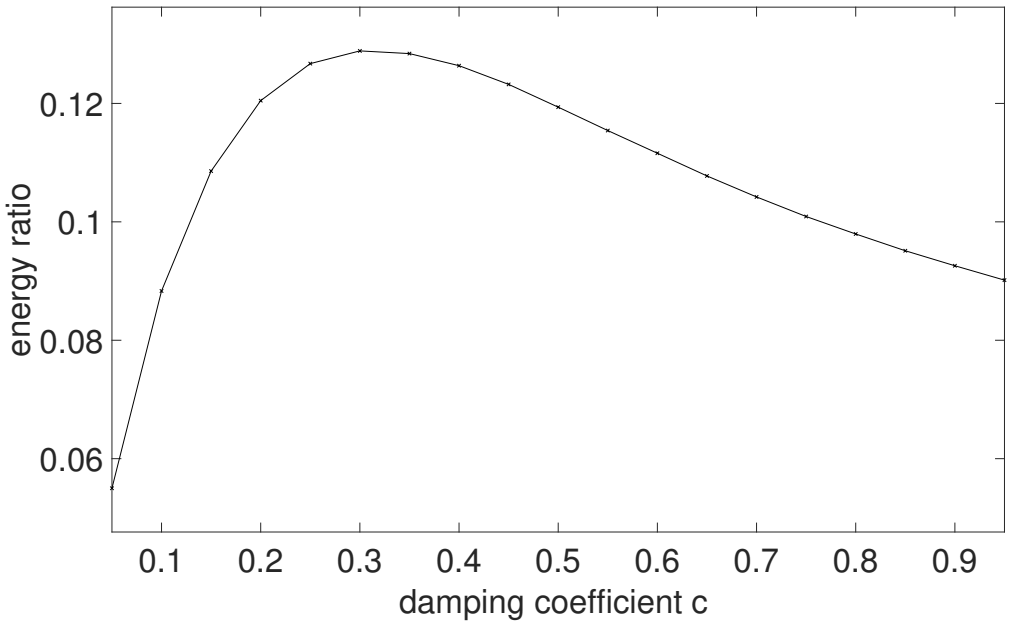

Figure 3.7 – Spring: recoverable energy for different values of the damping coefficient

The best choice seems to be obtained around $c = 0.3$. Physically a small stiffness allows the spring to move as much as possible. Furthermore a small damping coefficient would not be able to absorb any energy. In contrary if the damping coefficient is too high, the buoy will be slowed down due to the damping and the recoverable energy would not be optimal.

3.5 Conclusion

A strong coupling between a congested shallow water type model and Newton's second law of motion is presented for the modeling of floating structures. We have taken a particular care to the energy transfer between the solid and the water. An entropy correction is made at the discrete level in order to ensure an entropy dissipation law and the numerical scheme proposed in [55] is adapted to take into account a freely floating object. Finally numerical simulations are proposed to validate the approach and to show the feasibility of physically relevant cases.

However real life applications need an extension to the two dimensional case. Since the computations become CPU costly in higher dimensions, some scientific computing issues should be resolved beforehand. One can think of linking our method with a less CPU consuming scheme for free surface flow

far from the congested area.

The physical description of water waves is important when considering wave energy converters. More complex models such as dispersive models [27; 74] or layerwise models [5] or the combination of both [48] could be used to represent the flow. Dispersive models do not neglect the vertical acceleration and are therefore more adapted to characterize heave effets. Layerwise models can better modelize wind effects by considering a vertical profile of the velocity. Since our approach only concerns the water height and not the velocity, the numerical resolution of the cited models should not raise particular difficulties.

A logical follow-up is the interaction of several objects for the simulation of wave energy converter farms [92] or floating fragments during inondations. Since these phenomena take place on a large space scale, the proposed model seems well adapted. Our method is directly adaptable to take into account several objets. Nevertheless for the latter, interactions between the objets should be accounted for.

A challenging objective is the handling of submerged objets [47; 57]. This issue seems related to layerwise models since at least two water heights are necessary. However the transition between a totally submerged and a floating objet is still open at the moment. Eventually we might also consider the interaction of energy converters with the bottom as in [9; 10].

In appendix B the case of a rotation about a point $O \neq G$ is shown.

Appendix A

The transcritical analytical solution

The classical test case of transcritical steady flow is largely used to measure the convergence of a numerical scheme confronted to a hydraulic jump. Even if an explicit formula is not obtained, the exact solution can be computed on a grid. The analytical solution for free surface flow is described in [33]. This section is devoted to the analytical solution of the congested shallow water model. However, since the non-conservative product is not clearly defined, the strategy is only valid assuming the solution is continuous when the roof is reached. In other words, the top of the hydraulic jump is supposed not to reach the roof. In addition, the boundary conditions are given for the classical shallow water model in the subcritical regime. It follows that the flow does not reach the roof at the boundary.

The solution is given by intervals with constant hydraulic heads separated by discontinuities satisfying the classical Rankine-Hugoniot relation since the hydraulic jump is supposed not to reach the roof.
More precisely, for steady flow, the mass conservation equation of (2.2.8) leads to a constant mass flux $h\overline{u} = Q$. Moreover, when the water depth is continuous, the energy conservation Proposition 2.2.3 holds and yields a constant energy flux $\left(\frac{1}{2}\overline{u}^2 + g\left(h + B\right) + p_\eta\right) h\overline{u} = \mathcal{G}$. Assuming that the surface pressure and the water depth are known in a point, denoted from now on characteristic point X, the hydraulic head $K = \frac{\mathcal{G}}{Q}$ can be computed. More precisely, the hydraulic head reads

$$K = h\left(X\right) + B\left(X\right) + \frac{p\left(X\right)}{g} + \frac{H_c^3}{2h^2\left(X\right)} \tag{A.0.1}$$

with $H_c = \left(\frac{Q}{\sqrt{g}}\right)^{\frac{2}{3}}$ the critical water depth.

At the free surface, the surface pressure corresponds to the atmospheric pressure and the water depth is solution of the following third order polynomial

$$p_\eta = P_\eta \qquad \text{and} \qquad h^3 + \left(B + \frac{P_\eta}{g} - K\right) h^2 + \frac{H_c^3}{2} = 0. \tag{A.0.2}$$

More precisely, one can show that the water depth is the larger root of the polynomial in the area where the flow is subcritical and the smaller of the positive roots when the flow is supercritical. In the same interval, if the roof is reached, the water depth corresponds to the opening and the surface pressure is defined by the following expression

$$p_\eta = g\left(K - \overline{H} - B - \frac{H_c^3}{2\overline{H}^2}\right) \qquad \text{and} \qquad h = \overline{H}. \tag{A.0.3}$$

The surface pressure in (A.0.3) is a generalization of the Archimedes' principle since when the mass flux vanishes, i.e. $Q = 0$, thus $H_c = 0$, the surface pressure corresponds to the weight of a fictitious water volume above the roof.

Now let us explain the strategy followed to compute the analytical solution on a grid. In the following, we only detail how to determine the characteristic node j, discrete counterpart of the characteristic point X.

In the free surface area, the characteristic node j is determined by the point where the water depth corresponds to the critical water depth. Indeed, in this point the water depth is known (the pressure is determined by the atmospheric pressure) and the hydraulic head K can be computed using (A.0.1). More precisely, as it is explained in [33], this point corresponds to the point where $B + \frac{P_\eta}{g}$ is locally decreasing.

In the congested area, the characteristic node j is determined by the right point where the flow reaches the roof. Indeed since this point reaches the roof, we have $h_j = \overline{H}_j$ and since at its right the flow has a free surface and the surface pressure is assumed continuous we have $p_j = P_j$. To determine this point, we start from the right point where the opening intersects the critical water depth. At the left of this point, the flow is clearly supercritical. Then, we proceed successively node by node going to the left as follows. Assuming the current node is the characteristic node, the hydraulic head is computed using (A.0.1). Then, the pressure at the left neighbor node is computed using (A.0.3). If the relative pressure at the left is negative, we conclude that the current node is not the characteristic node and we pass to the next one. Once the characteristic node is determined, the water depth

at the right is computed using (A.0.2) until the hydraulic jump. At the left of the characteristic node, the surface pressure is computed using (A.0.3) until the pressure becomes negative, which corresponds to the entrance of the water under the roof. Eventually, the velocity can be deduced dividing in each point the mass flux by the water depth. The numerical implementation of the analytical solution is given in Algorithm 1.

Algorithm 1: Transcritical analytical solution

Input:

N	–	integer scalar	: Number of control volumes
H_c, g	–	real scalar	: Critical water depth, Gravity acceleration
H_r	–	real scalar	: Right water depth (boundary condition)
$B, \overline{H}, P$	–	real array(1:N)	: Bottom, Opening, Atmospheric pressure

for *i=1* **to** N **do** $(h_i, p_i) \leftarrow (H_c, P_i)$; *# Initialization*

*#*_____*Starting from the right border*_____

$(h_N, p_N) \leftarrow (H_r, P_N)$; $K \leftarrow$ (A.0.1) ; $subcritical \leftarrow (h_N > H_c)$;
$i \leftarrow N - 1$;
while $(i > 0)$ **do**
  if *subcritical* **then**
    $(h_i, p_i) \leftarrow$ (A.0.2) ; *# Assuming free surface*
    if $\left(h_i > \overline{H}_i\right)$ **then** $(h_i, p_i) \leftarrow$ (A.0.3) ; *# If congested*
  else
    *#*_____*Find the characteristic point*_____
    $j \leftarrow i + 1$; $found \leftarrow false$;
    while not $found$ **do**
      $j \leftarrow j - 1$;
      if $(j = 0)$ **then STOP** 42 *# Left boundary supercritical*
      if $\left(\overline{H}_j \geq H_c\right)$ **then**
        if $(gB_{j-1} + P_{j-1} \leq gB_j + P_j)$ **then**
          $(h_j, p_j) \leftarrow (H_c, P_j)$; $K \leftarrow$ (A.0.1) ;
          $found \leftarrow true$; *# Free surface area*
      else
        $(h_j, p_j) \leftarrow \left(\overline{H}_j, P_j\right)$; $K \leftarrow$ (A.0.1) ;
        $(h_{j-1}, p_{j-1}) \leftarrow$ (A.0.3) ;
        if $(p_{j-1} > P_{j-1})$ **then** $found \leftarrow true$; *# Congested area*
    *#*_____*Right side until free hydraulic jump*_____
    $i \leftarrow j - 1$; $RH \leftarrow false$;
    while not RH **do**
      $i \leftarrow i + 1$; $(h_i, p_i) \leftarrow$ (A.0.2) ; *# Assuming free surface*
      if $\left(h_i > \overline{H}_i\right)$ **then** $(h_i, p_i) \leftarrow$ (A.0.3) ; *# If congested*
      if $(i = N)$ **then** $RH \leftarrow true$; *# Right boundary supercritical*
      else $RH \leftarrow \left(\frac{H_c^3}{h_i} + \frac{h_i^2}{2} < \frac{H_c^3}{h_{i+1}} + \frac{h_{i+1}^2}{2}\right)$; *# Rankine-Hugoniot*
    *#*_____*Left congested side until free surface*_____
    $i \leftarrow j - 1$; $(h_i, p_i) \leftarrow$ (A.0.3);
    while $(p_i > 0)$ **do** $i \leftarrow i - 1$; $(h_i, p_i) \leftarrow$ (A.0.3) ;
    $subcritical \leftarrow (h_i > H_c)$; $(h_i, p_i) \leftarrow$ (A.0.2) ;
  if $h_i < H_c$ **then** $(h_i, P_i) \leftarrow (H_c, P_i)$;
  $subcritical \leftarrow (h_i > H_c)$; $i \leftarrow i - 1$; *# Test the regime*

for *i=1* **to** N **do** $\overline{u}_i \leftarrow \frac{\sqrt{gH_c^3}}{h_i}$; *# Computation of the velocity*

Appendix B

Rotation about a fixed point $O \neq G$

Some wave energy converters consist in a buoy fixed at a point $O \neq G$ and rotating around this point, see Figure B.1.

Let us give in the following the equations from Chapter 3 adapted to the case of a rotation about a fixed point $O \neq G$. The proofs will not be detailed since they are close to the equivalent results cited previously.

The only degree of freedom considered is an angular movement, i.e. $F_\zeta = Mg - \int_{\Omega_x} p_\eta \mathrm{d}x$ and $F_\chi = \int_{\Omega_x} p_\eta \partial_x \mathcal{R} \mathrm{d}x$ and the moment of inertia of the solid around an axis perpendicular to the plane and passing through O is denoted $\mathcal{J}_O$. Here the angle θ represents the angle between the vectors e_z and OG.

Since the object is rotating around $O \neq G$, it is more convenient to write the angular momentum theorem in O which slightly modifies the equation on θ compared to Chapter 3. The angular movement is defined by

$$\mathcal{J}_O \ddot{\theta} = -Mg\|OG\| \sin(\theta) + \int_{\Omega_x} p_\eta \partial_\theta R_0 \mathrm{d}x + T_\theta \tag{B.0.1}$$

with the initial conditions $\theta(0) = \theta^0$ and $\dot{\theta}(0) = \dot{\theta}^0$.

The weight has a torque about a point different from the center of mass which explains the supplementary term in the angular momentum theorem compared to Chapter 3.

The energy for the solid can be written.

Lemma B.0.1. *Any smooth solution of* (B.0.1) *satisfies the following energy law*

$$\partial_t \left(\frac{\mathcal{J}_O}{2} \dot{\theta}^2 - Mg\|OG\| \cos(\theta) \right) = \int_{\Omega_x} p_\eta \partial_\theta R_0 \mathrm{d}x \dot{\theta} + T_\theta \dot{\theta}.$$

The energy for the coupled fluid-solid system is obtained.

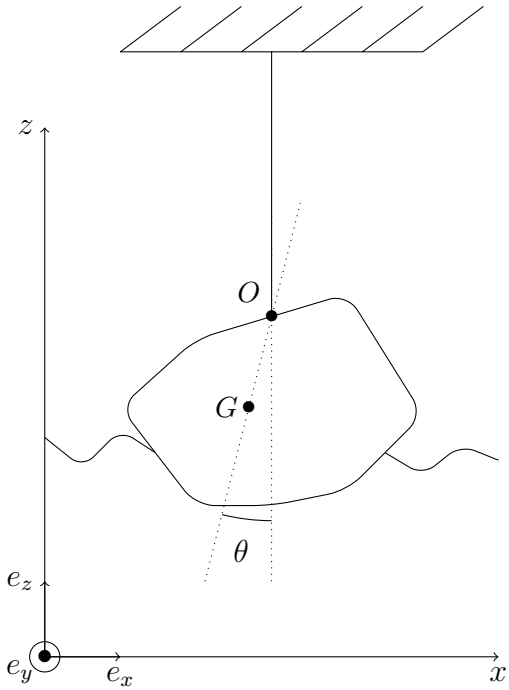

Figure B.1 – Buoy rotating around a fixed point $O \neq G$.

Proposition B.0.1. *Considering a no-flux boundary on Ω_x, any smooth solution of (B.0.1) and (3.2.1)-(3.2.2) satisfies the following energy balance law*

$$\partial_t \left(\int_{\Omega_x} \mathcal{E} \, \mathrm{d}x + \frac{\mathcal{J}_O}{2}\dot{\theta}^2 - Mg\|OG\| \cos(\theta) \right) = \int_{\Omega_x} (p_\eta + gh)\, \partial_t B \mathrm{d}x + T_\theta \dot{\theta}.$$

Using again the Newmark scheme (3.3.6) with $\Lambda = \theta$ and linearizing the equation, i.e. taking $\sin(\theta) = \theta$, (B.0.1) is discretized in the following way

$$\mathcal{J}_O \ddot{\theta}^n = -Mg\|OG\|\theta^n + \sum_{k\in\mathbb{T}} |k| p_k^n \partial_\theta^\delta R_k^n + T_\theta^n. \tag{B.0.2}$$

As before the discrete energy stability is proven for the adapted discretization of $\partial_\theta^\delta R_k^n$, see (3.3.15). Note that $\partial_t^n \chi = 0$ and $\partial_t^n \zeta = 0$ in (3.3.15) since the structure is fixed in the horizontal direction.

Let us first recall the energy for the Newmark scheme.

Lemma B.0.2. *Let $\alpha = \beta = 1$. Then the scheme (3.3.6) and (B.0.2) satisfies the following energy law*

$$\partial_t^{n+1} \left(\frac{\mathcal{J}_O}{2}\dot{\theta}^2 + \frac{Mg\|OG\|}{2}\theta^2 \right) \leq \left(\sum_{k\in\mathbb{T}} \left(|k| p_k^{n+1} \partial_\theta^\delta R_k^{n+1} \right) + T_\theta^{n+1} \right) \partial_t^{n+1}\theta.$$

The energy stability is achieved for the coupled fluid-solid system.

Proposition B.0.2. *Consider a no-flux boundary on Ω_x and let $\alpha = \beta = 1$, then the scheme (3.3.1)-(3.3.2), (3.3.6) and (B.0.2) with (3.3.15) admits the following dissipation law*

$$\partial_t^{n+1}\left(\sum_{k\in\mathbb{T}}|k|\mathcal{E}_k + \frac{\mathcal{J}_O}{2}\dot{\theta}^2 + \frac{Mg\|OG\|}{2}\theta^2\right) \leq \sum_{k\in\mathbb{T}}\left(|k|\left(p_k^{n+1} + gh_k^n\right)\partial_t^{n+1}B_k\right) + T_\theta^{n+1}\partial_t^{n+1}\theta.$$

A simulation of a buoy swinging around a fixed point $O \neq G$ due to incoming waves is proposed.

The buoy is an ellipse with semi-minor and semi-major axis equal to 0.2 respectively 0.4. Its mass is equal to 1.0×10^{-2} and the moment of inertia around O equals 1.0×10^{-3}. The horizontal and vertical coordinates of the fixed point O are 1 and 1.4. Furthermore the initial angle θ^0 is equal to 0 and $OG = 0.2$. No supplementary forces are considered, i.e. $T_\theta = 0$. Finally $\dot{\theta}^0 = 0$, $\phi^0 = 0.9g$ and $\overline{u}^0 = 0$.

At the left boundary waves of the form $h(t) = 0.9 + 0.025\sin(4\pi t)$ enter the domain. At the right boundary reflexion of the waves is eliminated using zero-order extrapolation, see [76, section 7.3.1].

We take $T = 2.5$, a domain with flat bottom of length 2 and the space step $\delta_x = 2.0 \times 10^{-3}$.

The buoy position, the water height as well as the surface pressure at different times are shown in Figure B.2. As expected the buoy starts moving due to the incoming waves and oscillates. As explained before, the CPR-parameter γ is taken equal to 2 in order to get more regularization. By comparing the buoy position for different values of the CPR-parameter, no significant difference is observed. However a regularization is observed on the surface pressure. The fixed point converges with a mean time step equal to 5.24×10^{-4} and the mean number of the linear system resolution per time step is equal to 44 which seems acceptable in terms of numerical costs.

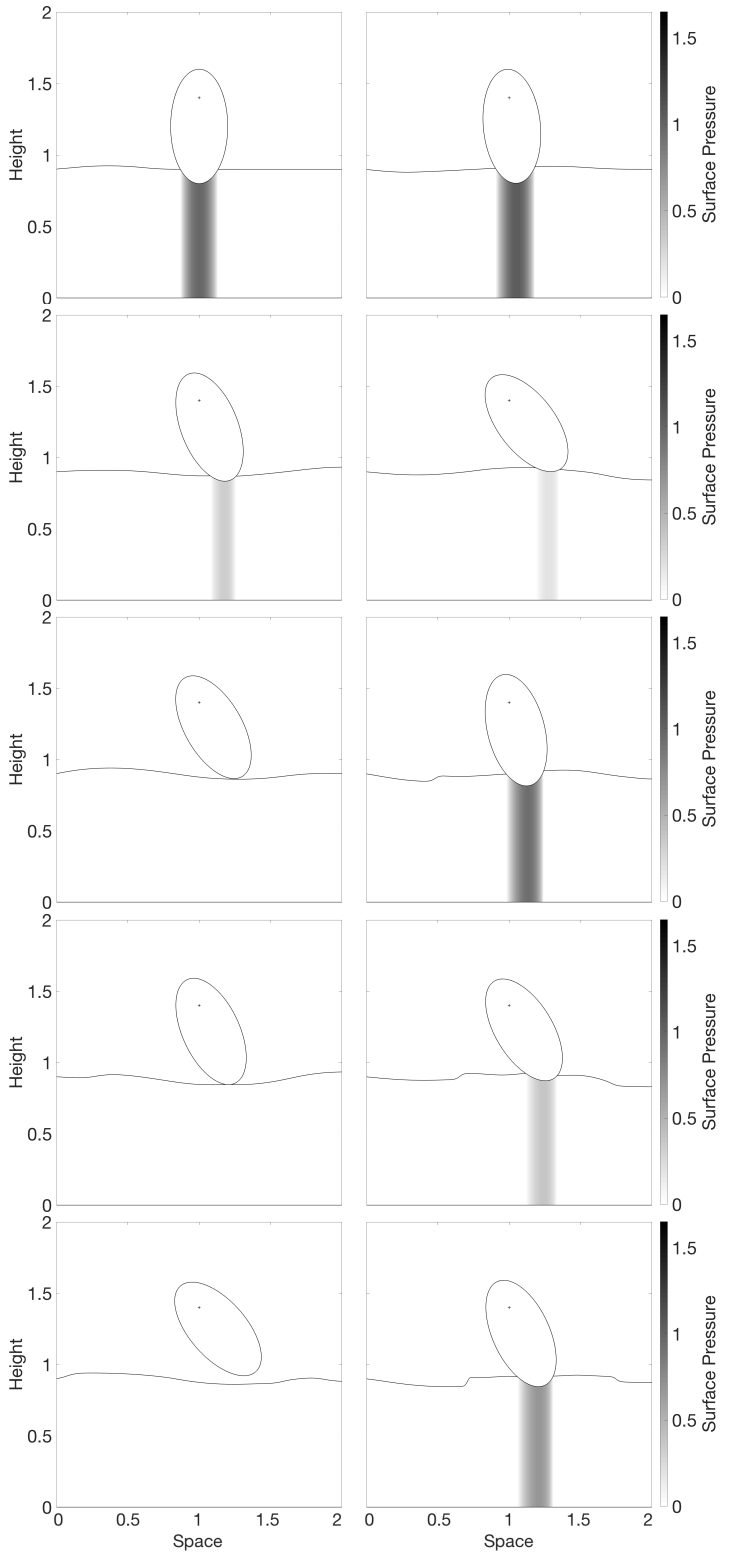

Figure B.2 – Swinging: buoy, water height and surface pressure from $t = 0.275$ to $t = 2.5$ at regular intervals

Bibliographie

[1] Agamloh, E., Wallace, A., and von Jouanne, A. (2008). Application of fluid-structure interaction simulation of an ocean wave energy extraction device. *Renewable Energy*, 33(4) :748–757.

[2] Aletti, M., Gerbeau, J.-F., and Lombardi, D. (2016). A simplified fluid-structure model for arterial flow. Application to retinal hemodynamics. *Computational Methods in Applied Mechanics and Engineering*, 306 :77–94.

[3] Audusse, E. (2005). A multilayer Saint-Venant model : derivation and numerical validation. *Discrete and Continuous Dynamical Systems - Series B*, 5 :189–214.

[4] Audusse, E., Bouchut, F., Bristeau, M.-O., Klein, R., and Perthame, B. (2004). A fast and stable well-balanced scheme with hydrostatic reconstruction for shallow water flows. *SIAM Journal on Scientific Computing*, 25(6) :2050–2065.

[5] Audusse, E., Bristeau, M.-O., Perthame, B., and Sainte-Marie, J. (2011). A multilayer Saint-Venant system with mass exchanges for shallow water flows. Derivation and numerical validation. *ESAIM : Mathematical Modelling and Numerical Analysis*, 45(1) :169–200.

[6] Aureli, F., Dazzi, S., Maranzoni, A., and Mignosa, P. (2015). Validation of single- and two-equation models for transient mixed flows : a laboratory test case. *Journal of Hydraulic Research*, 53(4) :440–451.

[7] Aw, A. and Rascle, M. (2000). Resurrection of 'second order' models of traffic flow. *SIAM Journal on Applied Mathematics*, 60(3) :916–938.

[8] Babarit, A. and Delhommeau, G. (2015). Theoretical and numerical aspects of the open source BEM solver NEMOH. In *11th European Wave and Tidal Energy Conference*, Nantes, France.

[9] Benyo, K. (2017). Wave-structure interaction for long wave models with a freely moving bottom. working paper or preprint <hal-01665775>.

[10] Benyo, K. (2018). Numerical analysis of the weakly nonlinear Boussinesq system with a freely moving body on the bottom. working paper or preprint <arXiv-1805.07216 >.

[11] Bermudez, A. and Vazquez, E. (1994). Upwind methods for hyperbolic conservation laws with source terms. *Computers & Fluids*, 23(8) :1049–1071.

[12] Berthelin, F. (2002). Existence and weak stability for a pressureless model with unilateral constraint. *Mathematical Models and Methods in Applied Sciences*, 12(02) :249–272.

[13] Berthelin, F. and Bouchut, F. (2003). Weak solutions for a hyperbolic system with unilateral constraint and mass loss. *Annales de l'Institut Henri Poincare (C) Non Linear Analysis*, 20(6) :975–997.

[14] Berthelin, F. and Broizat, D. (2012). A model for the evolution of traffic jams in multi-lane. *Kinetic and Related Models*, 5(4) :697–728.

[15] Berthelin, F., Degond, P., Delitala, M., and Rascle, M. (2008a). A model for the formation and evolution of traffic jams. *Archive for Rational Mechanics and Analysis*, 187(2) :185–220.

[16] Berthelin, F., Degond, P., Le Blanc, V., Moutari, S., Rascle, M., and Royer, J. (2008b). A traffic-flow model with constraints for the modeling of traffic jams. *Mathematical Models and Methods in Applied Sciences*, 18(supp01) :1269–1298.

[17] Bocchi, E. (2018). Floating structures in shallow water : local well-posedness in the axisymmetric case. working paper or preprint <arXiv-1802.07643>.

[18] Bosi, U., Engsig-Karup, A. P., Eskilsson, C., and Ricchiuto, M. (2018). A spectral/hp element depth-integrated model for nonlinear wave-body interaction. Research Report RR-9166, Inria Bordeaux Sud-Ouest ; Technical University of Denmark ; University of Aalborg ; RISE.

[19] Bouchut, F. (1994). *On zero pressure gas dynamics*, pages 171–190. World Scientific.

[20] Bouchut, F. (2004). *Nonlinear stability of finite volume methods for hyperbolic conservation laws and well-balanced schemes for sources*. Birkhäuser.

[21] Bouchut, F., Brenier, Y., Cortes, J., and Ripoll, J.-F. (2000). A hierarchy of models for two-phase flows. *Journal of Nonlinear Science*, 10(6) :639–660.

[22] Bourdarias, C., Ersoy, M., and Gerbi, S. (2012). A mathematical model for unsteady mixed flows in closed water pipes. *Science China Mathematics*, 55(2) :221–244.

[23] Bourdarias, C. and Gerbi, S. (2007). A finite volume scheme for a model coupling free surface and pressurised flows in pipes. *Journal of Computational and Applied Mathematics*, 209(1) :109–131.

[24] Bousso, S., Daynou, M., and Fuamba, M. (2013). Numerical modeling of mixed flows in storm water systems : critical review of literature. *Journal of Hydraulic Engineering*, 139(4) :385–396.

[25] Brebbia, C. A., Telles, J. C. F., and Wrobel, L. C. (1984). *Boundary Element Techniques - theory and applications in engineering*. Springer-Verlag, Berlin.

[26] Brenner, K. and Cancès, C. (2017). Improving Newton's method performance by parametrization : the case of Richards equation. *SIAM Journal on Numerical Analysis*, 55(4) :1760–1785.

[27] Bristeau, M.-O., Mangeney, A., Sainte-Marie, J., and Seguin, N. (2015). An energy-consistent depth-averaged Euler system : derivation and properties. *Discrete and Continuous Dynamical Systems - Series B*, 20(4) :961–988.

[28] Cancès, C. and Guichard, C. (2017). Numerical analysis of a robust free energy diminishing finite volume scheme for parabolic equations with gradient structure. *Foundations of Computational Mathematics*, 17(6) :1525–1584.

[29] Capart, H., Sillen, X., and Zech, Y. (1997). Numerical and experimental water transients in sewer pipes. *Journal of Hydraulic Research*, 35(5) :659–672.

[30] Castro, M., Gallardo, J. M., López-García, J. A., and Parés, C. (2008). Well-balanced high order extensions of Godunov's method for semilinear balance laws. *SIAM Journal on Numerical Analysis*, 46(2) :1012–1039.

[31] Chabannes, V. (2013). *Vers la simulation numérique des écoulements sanguins*. Thèse, Université de Grenoble.

[32] Chalons, C., Girardin, M., and Kokh, S. (2013). Large time step and asymptotic preserving numerical schemes for the gas dynamics equations with source terms. *SIAM Journal on Scientific Computing*, 35(6) :A2874–A2902.

[33] Chanson, H. (2004). *Hydraulics of open channel flow*. Elsevier Science.

[34] Chorin, A. J. (1968). Numerical solution of the Navier-Stokes equations. *Mathematics of Computation*, 22(104) :745–762.

[35] Clément, A., McCullen, P., Falcão, A., Fiorentino, A., Gardner, F., Hammarlund, K., Lemonis, G., Lewis, T., Nielsen, K., Petroncini, S., Pontes, M.-T., Schild, P., Sjöström, B.-O., Sørensen, H. C., and Thorpe, T. (2002). Wave energy in Europe : current status and perspectives. *Renewable and Sustainable Energy Reviews*, 6(5) :405–431.

[36] Cunge, J. A. and Wegner, M. (1964). Intégration numérique des équations d'écoulement de Barré de Saint-Venant par un schéma implicite de différences finies. *La Houille Blanche*, (1) :33–39.

[37] Dal Maso, G., LeFloch, P. G., and Murat, F. (1995). Definition and weak stability of nonconservative products. *Journal de mathématiques pures et appliquées*, 74(6) :483–548.

[38] de Saint-Venant, B. (1871). Théorie du movement non-permanent des eaux crues des rivières et à l'introduction des marées dans leur lit. *Comptes rendus de l'Académie des sciences*, 73 :147–154.

[39] Degond, P., Hua, J., and Navoret, L. (2011). Numerical simulations of the Euler system with congestion constraint. *Journal of Computational Physics*, 230(22) :8057–8088.

[40] Dellacherie, S. (2010). Analysis of Godunov type schemes applied to the compressible Euler system at low Mach number. *Journal of Computational Physics*, 229(4) :978–1016.

[41] Delle Monache, M. L. (2014). *Traffic flow modeling by conservation laws*. Thèse, Université Nice Sophia Antipolis.

[42] Demay, C. (2017). *Modelling and simulation of transient air-water two-phase flows in hydraulic pipes*. Thèse, Université Grenoble Alpes.

[43] Després, B. (2007). A geometrical approach to nonconservative shocks and elastoplastic shocks. *Archive for Rational Mechanics and Analysis*, 186(2) :275–308.

[44] Després, B., Lagoutière, F., and Seguin, N. (2011). Weak solutions to Friedrichs systems with convex constraints. *Nonlinearity*, 24(11) :3055–3081.

[45] Donea, J., Giuliani, S., and Halleux, J. (1982). An Arbitrary Lagrangian-Eulerian finite element method for transient dynamic fluid-structure interactions. *Computer Methods in Applied Mechanics and Engineering*, 33(1) :689–723.

[46] Dubois, F. and LeFloch, P. G. (1988). Boundary conditions for nonlinear hyperbolic systems of conservation laws. *Journal of Differential Equations*, 71(1) :93–122.

[47] Ducassou, B., Nuñez, J., Cruchaga, M., and Abadie, S. (2017). A fictitious domain approach based on a viscosity penalty method to simulate wave/structure interaction. *Journal of Hydraulic Research*, 55(6) :847–862.

[48] Fernandez-Nieto, E. D., Parisot, M., Penel, Y., and Sainte-Marie, J. (2017). A hierarchy of non-hydrostatic layer-averaged approximation of Euler equations for free surface flows. working paper or preprint <hal-01324012>.

[49] Fuamba, M. (2002). Contribution on transient flow modelling in storm sewers. *Journal of Hydraulic Research*, 40(6) :685–693.

[50] Gashaw, S., Goatin, P., and Härri, J. (2018). Modeling and analysis of mixed flow of cars and powered two wheelers. *Transportation Research Part C : Emerging Technologies*, 89 :148 – 167.

[51] Gerbeau, J.-F. and Perthame, B. (2001). Derivation of viscous Saint-Venant system for laminar shallow water ; numerical validation. *Discrete and Continuous Dynamical Systems - Series B*, 1(1) :89–102.

[52] Girard (1799). Brevets d'intervention. tome 2 numéro 150 page 265.

[53] Glowinski, R., Pan, T.-W., and Periaux, J. (1994). A fictitious domain method for Dirichlet problem and applications. *Computer Methods in Applied Mechanics and Engineering*, 111(3) :283–303.

[54] Godlewski, E., Parisot, M., Sainte-Marie, J., and Wahl, F. (2018a). Congested shallow water model : floating object. working paper or preprint <hal-01871708>.

[55] Godlewski, E., Parisot, M., Sainte-Marie, J., and Wahl, F. (2018b). Congested shallow water model : roof modelling in free surface flow. *ESAIM : Mathematical Modelling and Numerical Analysis*, 52(5) :1679 – 1707.

[56] Greenberg, J. M. and Leroux, A.-Y. (1996). A well-balanced scheme for the numerical processing of source terms in hyperbolic equations. *SIAM Journal on Numerical Analysis*, 33(1) :1–16.

[57] Guerber, E. (2011). *Numerical modelling of nonlinear interactions of waves with submerged structures : applied to the simulation of wave energy converters*. Thèse, Université Paris-Est.

[58] Guillard, H. and Murrone, A. (2004). On the behavior of upwind schemes in the low Mach number limit : II. Godunov type schemes. *Computers & Fluids*, 33(4) :655–675.

[59] Hamam, A. M. and McCorquodale, J. (1982). Transient conditions in the transition from gravity to surcharged sewer flow. *Canadian Journal of Civil Engineering*, 9(2) :189–196.

[60] Harris, J., Kuznetsov, K., Peyrard, C., Saviot, S., Mivehchi, A., T. Grilli, S., and Benoit, M. (2017). Simulation of wave forces on a gravity based foundation by a BEM based on fully nonlinear potential flow. In *27th Offshore and Polar Engineering Conference*, San Francsico, USA.

[61] He, H., Qu, Q., and Li, J. (2013). Numerical simulation of section systems in the pelamis wave energy converter. *Advances in Mechanical Engineering*, 5 :186056.

[62] Herbin, R., Kheriji, W., and Latché, J.-C. (2014). On some implicit and semi-implicit staggered schemes for the shallow water and Euler equations. *ESAIM : Mathematical Modelling and Numerical Analysis*, 48(6) :1807–1857.

[63] Iguchi, T. and Lannes, D. (2018). Hyperbolic free boundary problems and applications to wave-structure interactions. working paper or preprint <arXiv-1806.07704>.

[64] Jin, S. and Wen, X. (2005). Two interface-type numerical methods for computing hyperbolic systems with geometrical source terms having concentrations. *SIAM Journal on Scientific Computing*, 26(6) :2079–2101 (electronic).

[65] John, F. (1949). On the motion of floating bodies. I. *Communications on Pure and Applied Mathematics*, 2(1) :13–57.

[66] Kashiwagi, M. (2000). Non-linear simulations of wave-induced motions of a floating body by means of the mixed Eulerian-Lagrangian method.

Proceedings of the Institution of Mechanical Engineers, Part C : Journal of Mechanical Engineering Science, 214(6) :841–855.

[67] Klainerman, S. and Majda, A. (1981). Singular limits of quasilinear hyperbolic systems with large parameters and the incompressible limit of compressible fluids. *Communications on Pure and Applied Mathematics*, 34(4) :481–524.

[68] Klainerman, S. and Majda, A. (1982). Compressible and incompressible fluids. *Communications on Pure and Applied Mathematics*, 35(5) :629–651.

[69] Knudsen, J. and Hjorth, P. (2012). *Elements of Newtonian Mechanics*. Springer Berlin Heidelberg.

[70] Krenk, S. (2006). Energy conservation in Newmark based time integration algorithms. *Computer methods in applied mechanics and engineering*, 195(44) :6110–6124.

[71] Labbé, S. and Maitre, E. (2013). A free boundary model for Korteweg fluids as a limit of barotropic compressible Navier-Stokes equations. *Methods and Applications of Analysis*, 20(2) :165–178.

[72] Landajuela, M., Vidrascu, M., Chapelle, D., and Fernández, M. A. (2017). Coupling schemes for the FSI forward prediction challenge : comparative study and validation. *International Journal for Numerical Methods in Biomedical Engineering*, 33(4) :e2813.

[73] Lannes, D. (2017). On the dynamics of floating structures. *Annals of PDE*, 3(1) :11.

[74] Lannes, D. and Bonneton, P. (2009). Derivation of asymptotic two-dimensional time-dependent equations for surface water wave propagation. *Physics of Fluids*, 21(1) :016601.

[75] Lefebvre-Lepot, A. and Maury, B. (2011). Micro-macro modelling of an array of spheres interacting through lubrication forces. *Advances in Mathematical Sciences Advances in Mathematical Sciences and Applications*, 21(2) :535–557.

[76] LeVeque, R. J. (2002). *Finite volume methods for hyperbolic problems*. Cambridge University Press.

[77] Levi, L. (2001). Obstacle problems for scalar conservation laws. *ESAIM : Mathematical Modelling and Numerical Analysis*, 35(3) :575–593.

[78] Li, J. and McCorquodale, A. (1999). Modeling mixed flow in storm sewers. *Journal of Hydraulic Engineering*, 125(11) :1170–1180.

[79] Lions, P.-L. and Masmoudi, N. (1999). On a free boundary barotropic model. *Annales de l'Institut Henri Poincare (C) Non Linear Analysis*, 16(3) :373–410.

[80] Marche, F. (2007). Derivation of a new two-dimensional viscous shallow water model with varying topography, bottom friction and capillary effects. *European Journal of Mechanics - B/Fluids*, 26(1) :49–63.

[81] Masuda, Y. (1986). An experience of wave power generator through tests and improvement. In *Hydrodynamics of Ocean Wave-Energy Utilization*, Berlin Heidelberg, Germany.

[82] Matt, F., Babarit, A., Ben, C., David, F., Louise, O., Katie, S., Johannes, S., and Troch, P. (2012). A review of numerical modelling of wave energy converter arrays. In *ASME 2012 International Conference on Ocean, Offshore and Artic Engineering*, Rio de Janeiro, Brazil.

[83] Maury, B. and Preux, A. (2015). Pressureless Euler equations with maximal density constraint : a time-splitting scheme. working paper or preprint <hal-01224008>.

[84] Maury, B., Roudneff-Chupin, A., Santambrogio, F., and Venel, J. (2011). Handling congestion in crowd motion modeling. *Networks and Heterogeneous Media*, 6(3) :485–519.

[85] Meyer-Peter, E. and Favre, H. (1932). Über die Eigenschaften von Schwällen und die Berechnung von Unterwasserstollen. *Schweizerische Bauzeitung*, 100(4/5) :43–50.

[86] Michel-Dansac, V., Berthon, C., Clain, S., and Foucher, F. (2017). A well-balanced scheme for the shallow-water equations with topography or Manning friction. *Journal of Computational Physics*, 335 :115–154.

[87] Navier, H. (1827). Mémoire sur les lois du mouvement des fluides. *Mémoires de l'Académie des sciences*, 6 :389–41.

[88] Noelle, S., Xing, Y., and Shu, C.-W. (2007). High-order well-balanced finite volume WENO schemes for shallow water equation with moving water. *Journal of Computational Physics*, 226(1) :29–58.

[89] Palm, J., Eskilsson, C., Moura Paredes, G., and Bergdahl, L. (2013). CFD simulation of a moored floating wave energy converter. In *Proceedings of the 10th European Wave and Tidal Energy Conference*, Aalborg, Denmark.

[90] Parisot, M. and Vila, J.-P. (2016). Centered-Potential Regularization for the advection upstream splitting method. *SIAM Journal on Numerical Analysis*, 54(5) :3083–3104.

[91] Parolini, N. and Quarteroni, A. (2005). Mathematical models and numerical simulations for the America's cup. *Computer Methods in Applied Mechanics and Engineering*, 194(9) :1001–1026.

[92] Penalba, M., Touzón, I., Lopez-Mendia, J., and Nava, V. (2017). A numerical study on the hydrodynamic impact of device slenderness and array size in wave energy farms in realistic wave climates. *Ocean Engineering*, 142 :224–232.

[93] Perrin, C. and Zatorska, E. (2015). Free/congested two-phase model from weak solutions to multi-dimensional compressible Navier-Stokes equations. *Communications in Partial Differential Equations*, 40(8) :1558–1589.

[94] Perthame, B. (2004). PDE models for chemotactic movements : parabolic, hyperbolic and kinetic. *Applications of Mathematics*, 49(6) :539–564.

[95] Perthame, B., Quirós, F., and Vázquez, J. L. (2014). The Hele–Shaw asymptotics for mechanical models of tumor growth. *Archive for Rational Mechanics and Analysis*, 212(1) :93–127.

[96] Prosperetti, A. (2002). Navier-Stokes numerical algorithms for free-surface flow computations : an overview. In *Drop-Surface Interactions*, Vienna, Austria.

[97] Quarteroni, A., Tuveri, M., and Veneziani, A. (2000). Computational vascular fluid dynamics : problems, models and methods. *Computing and Visualization in Science*, 2(4) :163–197.

[98] Rannacher, R. (1992). *On Chorin's projection method for the incompressible Navier-Stokes equations*, pages 167–183. Springer Berlin Heidelberg.

[99] Roudneff, A. (2011). *Macroscopic modelling of crowd motion.* Thèse, Université Paris Sud - Paris XI.

[100] Shen, J. (1997). Pseudo-compressibility methods for the unsteady incompressible Navier-Stokes equations. *Proceedings of the 1994 Beijing*

symposium on nonlinear evolution equations and infinite dynamical systems, pages 68–78.

[101] Song, C., A. Cardie, J., and Sau Leung, K. (1983). Transient mixed-flow models for storm sewers. *Journal of Hydraulic Engineering*, 109(11) :1487–1504.

[102] Stokes, G. G. (1845). On some cases of fluid motion. *Transactions of Cambridge Philosophical Society*, 8 :287–305.

[103] Témam, R. (1969). Sur l'approximation de la solution des équations de Navier-Stokes par la méthode des pas fractionnaires (I). *Archive for Rational Mechanics and Analysis*, 32(2) :135–153.

[104] Wiggert, D. C. (1972). Transient flow in free surface, pressurized systems. *Journal of the Hydraulics Division*, 98(1) :11–27.

[105] Wu, G. and Taylor, R. (2003). The coupled finite element and boundary element analysis of nonlinear interactions between waves and bodies. *Ocean Engineering*, 30(3) :387–400.

[106] Wylie, E., Streeter, V., and Suo, L. (1993). *Fluid transients in systems*. Prentice Hall.

[107] Yu, Y.-H. and Li, Y. (2013). Reynolds-averaged Navier–Stokes simulation of the heave performance of a two-body floating-point absorber wave energy system. *Computers & Fluids*, 73 :104–114.

Modélisation et analyse des interactions entre écoulements à surface libre et objets flottants

Cette thèse traite de la modélisation et de la résolution numérique d'écoulements sur un grand domaine en présence d'un objet flottant. Les applications de ce travail sont les écoulements sous la banquise ou dans les conduites, la dérive d'icebergs ou la production d'énergie renouvelable. Nous dérivons un modèle de type Saint-Venant avec une contrainte de congestion supplémentaire depuis les équations de Navier-Stokes. La contrainte de congestion est un défi pour la résolution numérique d'équations hyperboliques. Nous proposons alors un modèle unifié basé sur une relaxation pseudo-compressible pour la résolution. Cette approche ne nécessite pas de décrire la dynamique de l'interface entre la partie en charge et la partie à surface libre de l'écoulement. Nous identifions les propriétés nécessaires à la résolution numérique (schéma bas-Froude, préservation des équilibres, couplage satisfaisant l'entropie) et décrivons l'adaptation d'un schéma volumes finis. Une attention particulière est portée sur la dissipation de l'énergie mécanique au niveau continu comme au niveau discret. La méthode est validée en dimension un sur des solutions analytiques stationnaires et non-stationnaires ainsi que sur des cas plus concrets pouvant modéliser de façon simplifiée des récupérateurs d'énergie.

équations de Saint-Venant, modèle hyperbolique congestionné, schéma well-balanced, schéma satisfaisant l'entropie, schéma bas-Froude

Modeling and analysis of interactions between free surface flows and floating structures

This thesis is about the modeling and the numerical approximation on a large space scale of flows in the presence of a floating body. It is motivated by applications for geophysical phenomena such as flows under the ice floe or in sewers, floating icebergs and renewable energy production using wave energy converters. We derive a shallow water model with a supplementary congestion constraint from the Navier-Stokes equations. The congestion constraint is a challenging problem for the numerical approximation of hyperbolic equations. Thus we propose a unified model based on a pseudo-compressible relaxation for the resolution. This approach does not need to describe the dynamics of the interface between the free surface and the congested domain. We identify the mandatory properties for the numerical scheme (low-Froude stability, well-balanced character, entropy-satisfying coupling) and describe the adaptation of a numerical scheme based on a finite volume method. We focus on an energy dissipation law at the continuous as well as discrete level. In the one dimensional case, a validation using stationary and non-stationary analytical solutions is established and the feasibility to simulate a simple energy converter is shown.

shallow water equations, congested hyperbolic model, entropy-satisfying scheme, well-balanced scheme, low-Froude stability